学位論文

Experimental search for hidden photon CDM in the eV mass range with a concave mirror

(凹面鏡を用いた質量 eV 領域における

hidden photon ダークマター探索)

平成 27 年 12 月博士（理学）申請

東京大学大学院理学系研究科

物理学専攻

鈴木　惇也

Experimetal search for hidden photon CDM in the eV mass range with a concave mirror

Jun'ya Suzuki

February 5, 2016

Abstract

A lot of evidence from observations of astronomical objects indicates the existence of invisible non-baryonic matter (dark matter, DM) in the universe. Direct detection of dark matter is one of the most urgent tasks in experimental physics today.

The most prominent and paradigmatic candidate for dark matter is weakly interacting massive particles (WIMPs) such as neutralinos predicted in supersymmetric theories, and most of the current experiments aim to detect WIMPs via their elastic scattering off atomic nuclei. However, there are alternative candidates which can explain the density of dark matter today, and hidden photon (or hidden-sector photon, dark photon) is one of those candidates.

We report an experimental search for hidden photon cold dark matter (HP CDM) with a novel method using a concave mirror for the first time. From the result of the measurement, we found no evidence for the existence of HP CDM and set an upper limit on the photon-HP mixing parameter of $\chi \sim 7 \times 10^{-12}$ for the hidden photon mass $m_{\gamma'}$ between 1.9 eV and 4.3 eV.

Contents

List of Figures

List of Tables

Chapter 1

Introduction

The existence of invisible matter (dark matter, DM) is supported by a lot of astronomical observations. The standard model of cosmology (Λ-CDM), which supposes the existence of a cosmological constant Λ and cold dark matter in the universe, has successfully explained lots of observational facts including astonishing accordance with CMB observations.

Direct detection of dark matter is one of the most important tasks of cosmology and particle physics today. Although many groups around the world have paid a lot of efforts to directly detect DM particles, it has not yet been achieved.

Most of experiments aiming at DM detection assume that dark matter is mainly composed of Weakly Interacting Massive Particles (WIMPs) and looking for their elastic scattering off atomic nuclei. However, there exist alternative candidates which account for DM features, and Weakly Interacting Slim Particles (WISPs), like axions and hidden photons, can be the main component of DM via the misalignment mechanism. If DM is mainly composed of those light particles, apparatus for WIMPs would miss them because of their small mass.

Hidden photons X^μ are gauge bosons of light extra U(1) symmetry beyond standard model, and they interact with ordinary photons A^μ via a kinetic mixing term $(-\chi/2)F_{\mu\nu}X^{\mu\nu}$, where $F_{\mu\nu} = \partial_\mu A_\nu - \partial_\nu A_\mu$ and $X_{\mu\nu} = \partial_\mu X_\nu - \partial_\nu X_\mu$ and have non-zero mass $m_{\gamma'}$ via the Higgs or the Stueckelberg mechanism. We can thus survey hidden photons by using the mixing with ordinary photons, although the signal would be very faint because the photon-HP mixing parameter χ is assumed to be extremely small. We therefore need some amplification method, together with a sensitive detector, to search for hidden photon CDM.

One of the amplification methods is the use of a microwave cavity. It is pointed out that past experiments for axion DM is also sensitive for hidden photon, and their non-detection results for axion DM were translated to upper limits for the mixing parameter χ.

Additionally, a novel method using a dish antenna was recently proposed. Hidden photon CDM around a reflecting material would yield emission of photons perpendicularly to the surface. Using a spherical surface, we can therefore concentrate photons induced by non-relativistic hidden photons to the center of the sphere.

In this thesis, we report on the first experimental search for hidden photon CDM with this amplification method. We used an optical set-up, a photodetector and a concave mirror, to survey DM hidden photons in the eV mass range. The essential part of the experiment has already been published in the Journal of Cosmology and

Astroparticle Physics (cf. Ref. [49]).

The structure of this thesis is as follows. In Chapter 2, we make a short review of DM. Evidences for its existence are explained, and the status of experimental searches is reviewed. In Chapter 3, we introduce the theory of hidden photon and its experimental investigations of the past. The method with a dish antenna is explained in detail in Chapter 4. In the next chapter, we describe our apparatus utilizing the 'dish' method. The following chapter is devoted to the description of the experimental procedure and the analysis. We review future prospects for experimental searches for hidden photon CDM in Chapter 7, and conclude the thesis in the next chapter.

Chapter 2

Dark matter

The existence of dark matter is now firmly established by a lot of observational facts, though its direct/indirect detection has not yet been achieved. We know very little about the nature of dark matter, and a variety of theories have been proposed to account for the existence of particle dark matter.

Discussions on dark matter spread to a very wide range of length scales: from the cosmological scale to the scale of particle physics. The largest scale and the smallest scale of our knowledge should be unified to fully understand the nature of dark matter, which stimulates the progress in the understanding for the early ages of the universe. This fact attracts a lot of astronomers, particle physics theorists and experimentalists, and the study of dark matter is now one of the most exciting fields in the science community.

In this chapter, we make a brief review on dark matter, from the evidence for its existence to the latest status of direct detection experiments. The arguments in this chapter is based on Ref. [46, 50, 51, 52, 14].

2.1 The existence of dark matter

There are a lot of evidences for the existence of dark matter in a variety of scales: the galactic scale, the scale of galaxy clusters, and the cosmological scales. The following is a short summary of those evidences spreading many orders of magnitude in the length scales.

- The galactic scale: rotation curves of galaxies
- The scale of galaxy clusters: velocity dispersion of galaxies in a galaxy cluster, the bullet cluster 1E 0657-56
- The cosmological scale: CMB anisotoropies

In this section, we briefly review these observational facts and their interpretations to the existence of dark matter. For a thorough review, see, eg, Ref. [46].

2.1.1 The galactic scale: rotation curve of a galaxy

The flatness of rotation curves is the most prominent and classical evidence for the existence of dark matter in a galaxy. A rotation curve is a plot which has velocities

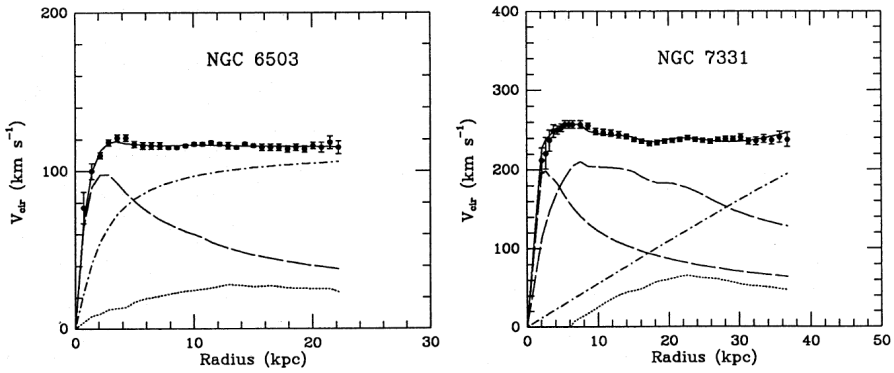

Figure 2.1: Rotation curves of spiral galaxies NGC 6503 and NGC 7331. The dashed curves show the visible components, the dotted curves for the gas, and the dash-dot curves are the contribution of dark matter. Taken from Ref. [1].

of stars and gas in a galaxy on the vertical axis and their distance from the galactic center on the horizontal axis.

By using Newtonian mechanics, the velocity $v(r)$ of objects in a galaxy at the radius r would obey

$$v\left(r\right)^{2} = G\frac{M\left(r\right)}{r},$$

where $M(r)$ is the mass within the radius r, and G is the gravitational constant. From this equation, we expect that the rotation speed would decrease as $v(r) \propto r^{-1/2}$ at the outer part of a galaxy, which, however, is not supported by the observation. Observations of Doppler shifts of the 21 cm line from cold hydrogen gas enable measurements of velocities at the outer part where there are no stars. Results of those measurements show flat rotation curves like Fig. 2.1, which indicate the existence of dark halo with profile $M(r) \propto r$, i.e., $\rho\left(r\right) \propto r^{-2}$.

Our Milky Way galaxy also has dark halo, and its study dates back to 1922 by J. H. Jeans [53], who claimed the discrepancy between the total mass and the mass of visible stars. Recent analysis [2] shows that the density of dark matter near the Solar system is found to be

$$\rho_{\mathrm{CDM}}^{\mathrm{local}} = (0.39 \pm 0.03)\,\frac{\mathrm{GeV}}{\mathrm{cm}^{3}} \tag{2.1}$$

by fitting a model of the galaxy to a variety of data. (The rotation curve of the Galaxy is shown in Fig. 2.2.) It is pointed out that this value may have to be multiplied by 1.2 ± 0.2 because of the departure of the density profile from spherical symmetry near the disk of the galaxy [54].

2.1.2 The scale of galaxy clusters: velocity dispersion, the bullet cluster

The evidence for the existence of dark matter in the scale of galaxy clusters first comes from the analysis of the movements of galaxies in the Coma cluster by Zwicky

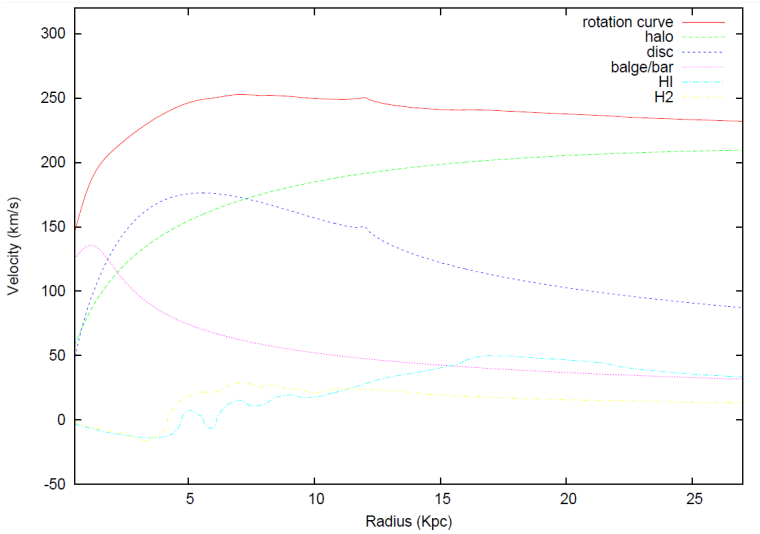

Figure 2.2: The rotation curve of the Galaxy assuming the Einasto profile for the local dark matter density. Taken from Ref. [2].

in 1933 [55, 56]. For virialized system, the virial theorem yields

$$\begin{array}{rcl} 2\langle T\rangle & = & -\langle V\rangle \\ \Updownarrow & & \Updownarrow \\ 2\times\frac{1}{2}m\times 3\sigma^2 & = & G\frac{Mm}{r}, \end{array}$$

which can be used to infer the total mass M in the cluster from the velocity standard deviation σ of the galaxies. Zwicky concluded that the luminous mass was far smaller than the total mass, which suggested that the cluster is dominated by invisible 'dark' matter.

Observations of X-ray emission by intracluster gas also provide strong evidence for the existence of dark matter in galaxy clusters. The equation of hydrostatic support reads

$$\frac{dP(r)}{dr} = -G\frac{M(r)\rho(r)}{r^2},$$

where $P(r)$ is the pressure and ρ the gas density at radius r. Assuming an ideal gas, the pressure P obeys $P = \rho k_B T/\mu m_p$, where μ is the average molecular weight and m_p the proton mass. Substituting it to the above equation, we get

$$\frac{d\log\rho}{d\log r} + \frac{d\log T}{d\log r} = -(\mu m_p G)\times\frac{1}{r}\times\frac{1}{k_B T}\times M(r).$$

This equation shows that we can estimate the total mass M within the cluster from the variation of ρ and T according to the radius, which can be obtained from high sensitivity X-ray intensity and spectral observations. Using X-ray imaging and spectroscopy of XMM-Newton, Pratt and Arnaud constructed profiles of gas density and temperature [57]. The result of the analysis shows that the gas density is only 20% of the total mass density, and provides a lot of ingredients for constructing DM models.

One of the most vivid and direct evidences of the existence of dark matter comes from the study of the 'bullet cluster', 1E0657-558 with $z = 0.296$ [3]. Fig.2.3 shows an

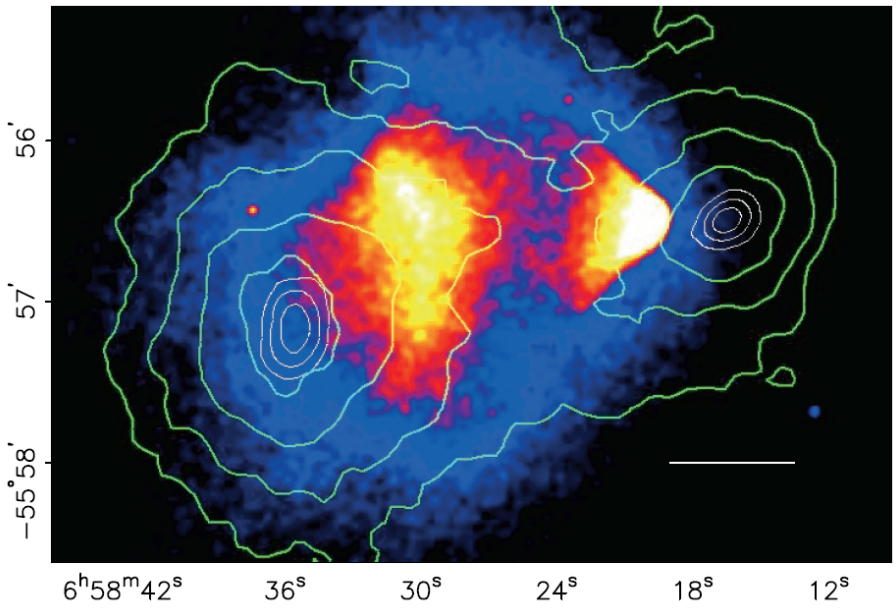

Figure 2.3: X-ray image of the cluster (Chandra 500 ks). Green contours show the mass distribution estimated by weak-lensing analysis. Taken from Ref. [3].

X-ray image by Chandra X-ray observatory overlaid by contours showing mass distribution estimated from gravitational lensing. The mass distribution has two distinct peaks of subclusters, while the gas distribution observed by X-ray emission is centered between the mass peaks. This strange feature can be interpreted as follows: the two clusters have collided, and the most masses dominated by collisionless dark matter pass through each other, while the gas content has collided and stayed near the collision point. Other colliding systems have been found in recent years [58, 59, 60, 61], and providing more and more materials for better understanding of dark matter.

2.1.3 The cosmological scale: CMB anisotropies

The serendipitous observation of the Cosmological Microwave Background (CMB) radiation by Penzias and Wilson in 1965 [62] opens up a new era of observational cosmology. The spectrum of the CMB radiation well resembles a blackbody radiation spectrum with $T \sim 2.7\,\mathrm{K}$, which strongly supports the Big Bang scenario for the early stage of the universe. The distribution of the intensity of the CMB radiation is extremely uniform down to the 10^{-3} level, where a dipole anisotropy associated with the motion of the earth appears. The observation by the COsmic Background Explorer (COBE) satellite revealed that there exist anisotropies at the 10^{-5} level [63], which stimulates activities for more and more precise mapping of the CMB sky, e.g., WMAP and Planck (Fig.2.4).

The CMB anisotropies provide an excellent test for models of the universe and can be used to estimate cosmological parameters [5, 14]. Anisotropies are usually expressed by a spherical harmonic expansion:

$$T(\theta, \phi) = \sum_{\ell m} a_{\ell m} Y_{\ell m}(\theta, \phi)\,.$$

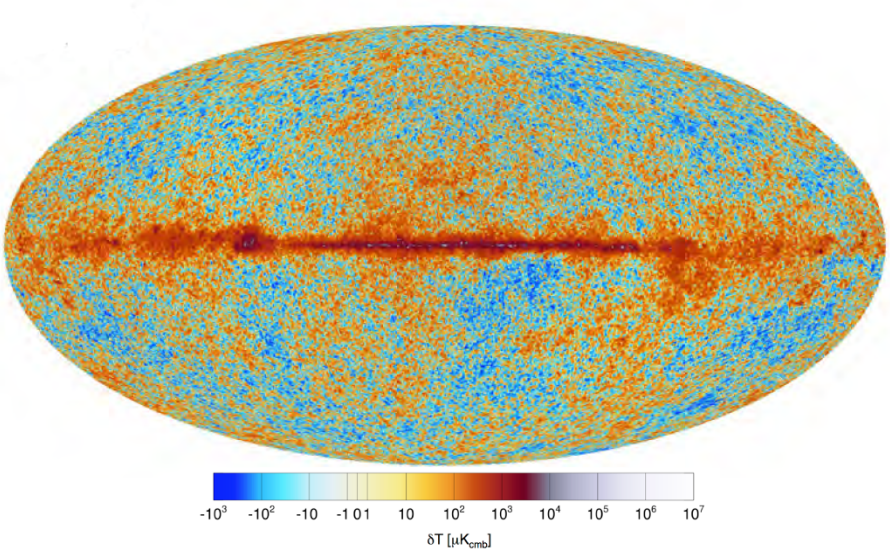

Figure 2.4: CMB temperature fluctuations at 70 GHz observed by Planck satellite. Taken from Ref. [4].

The variance C_ℓ is defined by

$$C_\ell \equiv \left\langle |a_{\ell m}|^2 \right\rangle \equiv \frac{1}{2\ell+1} \sum_{m=-\ell}^{\ell} |a_{\ell m}|^2 \,,$$

which has all information of the CMB if the sky is isotropic (i.e. no preferred m) and the fluctuations obey Gaussian statistics (i.e. no correlations between the modes). Figure 2.5 exhibits the sensitivity of the CMB angular power spectrum to cosmological parameters. The variation of the amount of baryons $\Omega_b h^2$ and the amount of matter $\Omega_m h^2$ have different effects on the spectrum, from which we can estimate the amount of dark matter.

Figure 2.6 shows the angular power spectrum of the CMB temperature taken by the Planck mission [6]. The red solid line is the best-fit theoretical spectrum based on the standard cosmological model (Λ-CDM). Although the Λ-CDM model has only ~ 10 free parameters, the line fits the data very well. From the CMB power spectra, together with the CMB lensing likelihood, the cosmological parameters $\Omega_b h^2$ and $\Omega_m h^2$ are estimated to be

$$\Omega_b h^2 = 0.02226 \pm 0.00023$$
$$\Omega_m h^2 = 0.1415 \pm 0.0019,$$

which suggest a large portion of the matter in the Universe is not baryons, in strong support of the existence of non-baryonic dark matter.

Apart from the CMB anisotropy, the big-bang nucleosynthesis (BBN) provides a good estimate of baryon density Ω_b. The BBN, based on the Standard Model physics, predicts the amount of the light elements, D, ^{3}He, ^{4}He, and ^{7}Li at the age of the Universe $t \sim 100\,\mathrm{sec}$. We can use the observed abundances of those light elements to test the theory, with the single free parameter η, the baryon-to-photon ratio. The observation is in good agreement with the theory, and provides the amount of baryons [14]

$$0.021 \leq \Omega_b h^2 \leq 0.025 \,(95\%\,\mathrm{CL}),$$

which agrees with the estimation from the CMB power spectra.

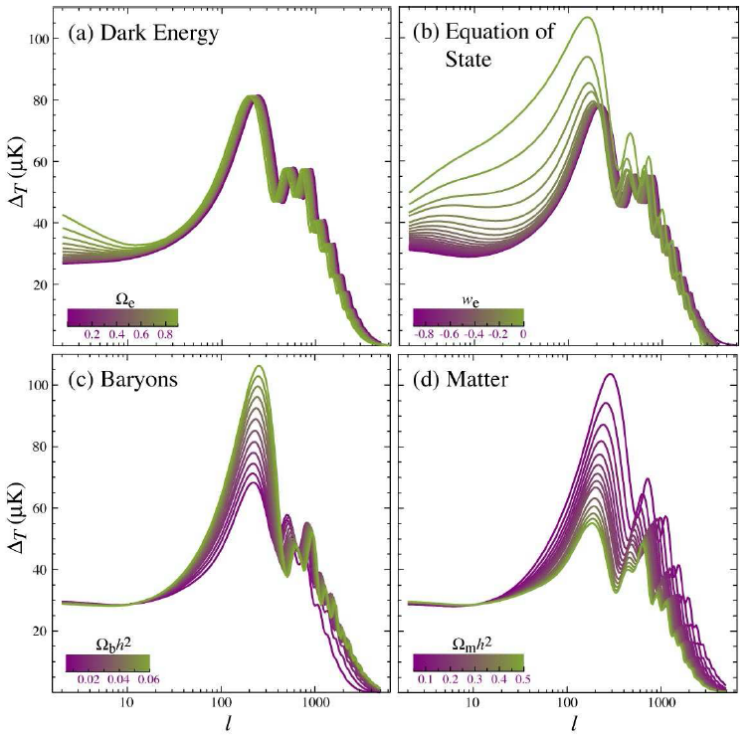

Figure 2.5: Sensitivity of the angular power spectrum of the CMB radiation to cosmological parameters. Δ_T is related to C_ℓ by $(\Delta_T)^2 = \ell\,(\ell+1)\,C_\ell/2\pi$. Taken from Ref. [5].

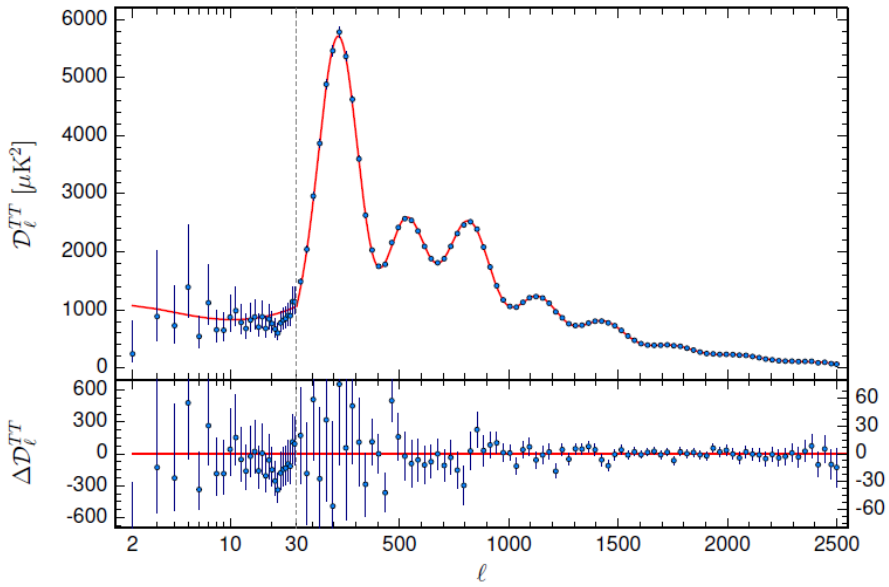

Figure 2.6: Angular power spectrum of the CMB temperature taken by the Planck mission [6]. The red solid line shows the best-fit theoretical spectrum based on Λ-CDM model. D_ℓ is defined as $D_\ell \equiv \ell(\ell+1)C_\ell/2\pi$.

2.2 Dark matter candidates

The identification of dark matter is a long-standing problem of cosmology and particle physics today. Although a lot of evidence indicates the existence of dark matter as described in the previous section, we still have little clues to specify the nature of dark matter.

Among a lot of candidates of dark matter, several scenarios have been proved to be unsuitable. One of those candidates is MAssive COmpact Hallo Objects (MACHOs). MACHOs are astronomical objects which emit so little radiation that they cannot be seen in ordinary observations. Despite their darkness, MACHOs could be found by looking for gravitational microlensing events. If such an astronomical object passes through the line of sight of a star, it would cause a transient amplification of the flux from the star. To search for such events, several collaborations, such as the EROS[64], had monitored stars in the Magellanic Clouds. As a result of these experiments, it was proved that such microlensing events do not occur as frequently as expected. Although the possibility for MACHO dark matter has not yet completely closed, the main focus has moved to other candidates.

Standard model neutrinos have also proved that they cannot account for the main component of dark matter. Neutrinos, which rarely interact with other SM particles, definitely contribute to dark matter: the relic density of neutrinos is calculated to be

$$\Omega_\nu h^2 \sim \frac{\sum_i m_{\nu_i}}{10^2\,\mathrm{eV}}.$$

Laboratory experiments, such as measurements of ^{3}H β decay[65], can be used to estimate the mass of the electron antineutrino, and they offer an upper limit $m_\nu < 2\,\mathrm{eV}$[14]. Combining this upper limit with mass-squared differences obtained in neutrino oscillation experiments, $\sum_i m_{\nu_i}$ is estimated to be far small to account for the density of dark matter.

The theory of structure formation also denies neutrinos to be the main component of dark matter. At the structure formation era, light particles like neutrinos still move at speed of light. Such collisionless relativistic particles erase fluctuations (free-streaming damping), and the study of large scale structure strongly limits the amount of those hot relics.

Although the standard model particles have been proved to be unsuitable for dark matter, particle physics beyond the standard model offers several candidates for dark matter. These candidates include WIMPs and axions. We devote the rest of this section to a review of these candidates.

2.2.1 WIMPs

Weakly Interacting Massive Particles (WIMPs) are the most prominent candidates for dark matter. WIMP is a generic name for massive particles with the masses in the range of GeV to TeV, which includes neutralinos from supersymmetric theories and $B^{(1)}$, the first Kaluza-Klein excitation state of the $\mathrm{U}(1)_Y$ gauge boson, from theories with extra dimensions.

Such heavy particles would decay into lighter particles along the history of the universe without any protection. Theories beyond the standard model offer some sort of conserved quantum numbers, which may let such heavy particles survive to the present.

WIMP has drawn attention because the abundance can be explained in standard thermal production scenario. At the early stage of the universe, WIMPs were created in thermal equilibrium with other particles. As the universe cooled down, the creation of WIMPs gradually stopped. The expansion of the universe diluted the density of WIMPs, preventing them from WIMP-WIMP annihilation. Then the number of WIMPs in a comoving volume fixed ('freeze out'). Expecting an annihilation cross section of the form $\langle\sigma v\rangle \sim g^4/m_\chi^2$, particles with the mass around $\sim 10^2\,\mathrm{GeV}$ can explain the right abundance $\Omega_\chi \sim 0.2$.

The following is a quick confirmation of the above argument [66]. Using the freeze-out temperature $T_{\mathrm{f.o.}}$ and the density $n_{\mathrm{f.o.}}$, we can estimate the current density as

$$\Omega_\chi = \frac{\rho_\chi}{\rho_c} = \frac{m_\chi n_0}{\rho_c} = \frac{m_\chi}{\rho_c}\frac{T_0^3}{T_{\mathrm{f.o.}}^3} n_{\mathrm{f.o.}}, \tag{2.2}$$

where we used $aT \sim$ const and the conservation of the number of particles in a comoving volume

$$n_0 a_0^3 \simeq n_{\mathrm{f.o.}} a_{\mathrm{f.o.}}^3 \Leftrightarrow \frac{n_0}{T_0^3} \simeq \frac{n_{\mathrm{f.o.}}}{T_{\mathrm{f.o.}}^3}.$$

Now our task is to estimate the freeze-out temperature $T_{\mathrm{f.o.}}$ and the density $n_{\mathrm{f.o.}}$ when the freeze-out occurs. The number density of non-relativistic particles in the equilibrium obeys

$$n = (m_\chi T)^{3/2} \exp\left(-\frac{m_\chi}{T}\right), \tag{2.3}$$

which relates $n_{\mathrm{f.o.}}$ to $T_{\mathrm{f.o.}}$. The freeze-out occurs when $n_{\mathrm{f.o.}} \cdot \langle\sigma v\rangle \sim H$, where H is the Hubble parameter which satisfies the Friedmann equation,

$$H^2 = \frac{8\pi G}{3}\rho.$$

In the radiation dominated era, ρ obeys $\rho = (\pi^2/30)\cdot g_* \cdot T^4$ with g_* the number of relativistic degrees of freedom. We approximate these relations as $H \simeq T^2/M_P$ with M_P the reduced Planck mass $M_P = 1/\sqrt{8\pi G}$. Then $n_{\mathrm{f.o.}} \cdot \langle\sigma v\rangle \sim H$ yields

$$n_{\mathrm{f.o.}} \sim \frac{T_{\mathrm{f.o.}}^2}{M_P \cdot \langle\sigma v\rangle}. \tag{2.4}$$

From Eq.(2.3) and (2.4), with $m_\chi/T \equiv x$, we derive

$$\begin{aligned} \frac{m_\chi^3}{x^{3/2}} e^{-x} &= \frac{m_\chi^2}{x^2 \cdot M_P \cdot \langle\sigma v\rangle} \\ \Leftrightarrow \sqrt{x}\cdot e^{-x} &= \frac{1}{m_\chi \cdot M_P \cdot \langle\sigma v\rangle}. \end{aligned}$$

Note that x is not quite sensitive to the value of right-hand side. Substituting suitable values yield $x \sim 20$. Using Eq.(2.2) and (2.4), we obtain

$$\begin{aligned} \Omega_\chi &= \left(\frac{T_0^3}{\rho_c M_P}\right)\frac{x_{\mathrm{f.o.}}}{\langle\sigma v\rangle} \sim \left(\frac{(10^{-4}\,\mathrm{eV})^3}{10^{-6}\,\mathrm{GeV/cm^3}\times 10^{18}\mathrm{GeV}}\right)\times\frac{x_{\mathrm{f.o.}}}{\langle\sigma v\rangle} \\ \Leftrightarrow \left(\frac{\Omega_\chi}{0.2}\right) &\sim \frac{x_{\mathrm{f.o.}}}{20}\left(\frac{10^{-8}\mathrm{GeV}^{-2}}{\langle\sigma v\rangle}\right). \end{aligned}$$

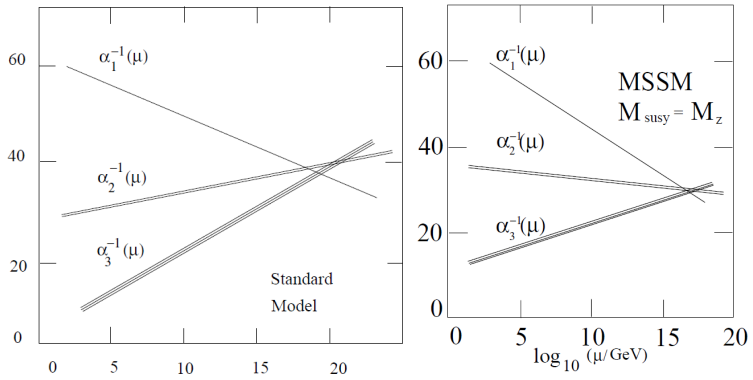

Figure 2.7: Convergence of the running coupling constants at the GUT scale. The figures are taken from Ref. [7].

If we suppose the annihilation cross section to have a form like

$$\sigma v \sim \frac{\pi\alpha^2}{m_\chi^2},$$

we get the right abundance when $m_\chi \sim 10^2\,\mathrm{GeV}$.

Supersymmetry

Among many theories beyond the Standard Model, supersymmetry (SUSY) is the most attractive extension, and a lot of effort has been devoted to study its potential. Supersymmetry is a continuous symmetry which connects bosons and fermions, and supersymmetric theories are expected to solve several problems of particle physics:

- Unification of the coupling constants
  Supersymmetry modifies the energy dependence of the coupling constants, which may bring them to converge at the GUT scale (see Fig. 2.7).

- Hierarchy problem
  The quadratic divergence of corrections to the Higgs mass would be canceled by corrections from superpartners.

Additionally, supersymmetric theories offer a good candidate for dark matter. By invoking a discrete symmetry called R parity, under which Standard Model particles are taken to be even and their superpartners to be odd, the lightest supersymmetric particle (LSP) would be stable.

One of the supersymmetric theories is the Minimal Supersymmetric Standard Model (MSSM), which is the supersymmetric version of the Standard Model. The MSSM contains

- Vector superfields for the gauge group
  the gauge bosons and the gauginos

- Chiral superfields L_{iI}, $\bar{E}_I$, $Q_{\alpha iI}$, $\bar{U}_I^\alpha$, $\bar{D}_I^\alpha$
  quarks, leptons, and their superpartners (squarks and sleptons)

- Chiral superfields H_i and $\bar{H}_i$
  two higgs fields and the higgsinos

The Lagrangian of the MSSM is specified by these constituents together with a superpotential

$$W = -y_{IJ}\varepsilon^{ij}H_i L_{jI}\bar{E}_J - y'_{IJ}\varepsilon^{ij}H_i Q_{\alpha jI}\bar{D}^\alpha_J - y''_{IJ}\bar{H}^i Q_{\alpha iI}\bar{U}^\alpha_J - \mu\varepsilon^{ij}\bar{H}_i H_j.$$

The MSSM has two higgs fields rather than a single field like in the Standard Model because a superpotential, with which we can derive terms invariant under supersymmetric transformation, cannot depends on conjugates of fields. By invoking R-parity conservation, terms of the form $\bar{H}^i L_{iI}$ are forbidden.

The constituents of the MSSM are listed in Table. 2.1 [45, 46]. Bino, Wino and two higgsino mix up to make four mass eigenstates, *neutralino*. The lightest neutralino is the most promising candidate of dark matter.

2.2.2 Axions

Axions are light pseudoscalar particles corresponding to the $\mathrm{U}(1)_{\mathrm{PQ}}$ symmetry, which was introduced to settle the strong CP problem. Non-perturbative effect of the strong interaction allows the Standard Model Lagrangian to include the term

$$\mathcal{L} \supset -\frac{g^2\theta}{32\pi^2}\tilde{F}^{a\mu\nu}F^a_{\mu\nu}\,,$$

where $F^a_{\mu\nu}$ is the SU(3) field strength and $\tilde{F}^{a\mu\nu} = (1/2)\epsilon^{\mu\nu\rho\sigma}F^a_{\rho\sigma}$ the dual field strength. This term causes CP violation and make the electric dipole moment of the neutron as

$$d_n = 3.2\times10^{-16}\theta\, e\,\mathrm{cm}.$$

The experimental investigations show $|d_n| < 2.9\times10^{-26}\, e\,\mathrm{cm}$ [67], from which we can conclude that $|\theta| < 10^{-10}$. Extreme smallness of this value needs some explanations. This problem is called the strong CP problem, and the solution to promote θ to a dynamical degree of freedom was proposed [68], in which the spontaneous symmetry breaking would lead to a new light boson, *axion* [69]. Its mass is connected to the breaking scale of the PQ symmetry f_a as

$$m_{a0} = \frac{F_\pi m_\pi}{f_a}\frac{\sqrt{m_d m_u}}{m_d+m_u} \approx 13\mu\mathrm{eV}\frac{10^{12}\,\mathrm{GeV}}{f_a}, \tag{2.5}$$

where $F_\pi = 184\,\mathrm{MeV}$ is the pion decay amplitude. The original model supposed that $f_a \sim 10^2\,\mathrm{GeV}$, but it was experimentally ruled out. Observations of the SN1987A were translated to the lower bound $f_a > 10^{10}\,\mathrm{GeV}$ [70]. After the original proposal, generalized models were proposed [71, 72, 73, 74], where f_a is taken to be a free parameter.

In addition to the solution to the strong CP problem, the axion is a candidate of dark matter. Thermal production scenario like WIMPs is not suitable for axions because its mass is expected to be very light as described above. Alternatively, misalignment of the axion field at the early stage of the universe can explain the abundance of the dark matter density today.

Without any fine tuning, the initial value of the axion field φ would be expected to be $\varphi_0 \sim f_a$. The effective action of the axion field φ is

$$I[\varphi] = \int d^4x\sqrt{-\mathrm{Det}g}\left(-\frac{1}{2}g^{\mu\nu}\partial_\mu\varphi\partial_\nu\varphi - \frac{1}{2}m_a^2\varphi^2\right).$$

Standard Model particles and fields		Supersymmetric partners			
		Interaction eigenstates		Mass eigenstates	
Symbol	Name	Symbol	Name	Symbol	Name
$q = d,\ c,\ b,\ u,\ s,\ t$	Quark	$\tilde{q}_L,\ \tilde{q}_R$	Squark	$\tilde{q}_1,\ \tilde{q}_2$	Squark
$l = e,\ \mu,\ \tau$	Lepton	$\tilde{l}_L,\ \tilde{l}_R$	Slepton	$\tilde{l}_1,\ \tilde{l}_2$	Slepton
$\nu = \nu_e,\ \nu_\mu,\ \nu_\tau$	Neutrino	$\tilde{\nu}$	Sneutrino	$\tilde{\nu}$	Sneutrino
g	Gluon	$\tilde{g}$	Gluino	$\tilde{g}$	Gluino
$W^\pm$	W-boson	$\tilde{W}^\pm$	Wino		
H^-	Higgs boson	$\tilde{H}_1^-$	Higgsino	$\tilde{\chi}_{1,2}^\pm$	Chargino
H^+	Higgs boson	$\tilde{H}_2^+$	Higgsino		
B	B-field	$\tilde{B}$	Bino		
W^3	W^3-field	$\tilde{W}^3$	Wino		
H_1^0	Higgs boson			$\tilde{\chi}_{1,2,3,4}^0$	Neutralino
H_2^0	Higgs boson	$\tilde{H}_1^0$	Higgsino		
H_3^0	Higgs boson	$\tilde{H}_2^0$	Higgsino		

Table 2.1: The constituents of the MSSM [45, 46]. Bino, Wino and two higgsino mix up to make four mass eigenstates, neutralinos.

Neglecting the spatial variation and assuming a Robertson-Walker metric, we derive the field equation

$$\ddot{\varphi} + 3H(t)\dot{\varphi} + m_a^2(t)\varphi = 0. \tag{2.6}$$

Substituting $\varphi \sim e^{-i\int^t \omega(t')dt'}$ and omitting $\dot{\omega}$ term, we find

$$-\omega^2 - 3iH\omega + m_a^2 = 0.$$

Solving this equation yields

$$\begin{aligned}\omega_\pm &= \frac{1}{2}\left[-3iH \pm \sqrt{-9H^2 + 4m_a^2}\right] \\ &= \begin{cases} -3iH,\ -\frac{im_a^2}{3H} & (H \gg m_a) \\ m_a - i\frac{3}{2}H,\ -m_a - i\frac{3}{2}H & (H \ll m_a) \end{cases}\end{aligned}$$

1. $H \gg m_a$

At the early stage of the universe, we find two solutions

$$\begin{aligned}\varphi_+ &= \varphi_0 e^{-3\int_{t_0}^t H(t')dt'} = \varphi_0 \left(\frac{t}{t_0}\right)^{-3/2} = \varphi_0 \left(\frac{a_0}{a}\right)^3 \\ \varphi_- &= \varphi_0 e^{-m^2\int_{t_0}^t (1/3H)dt'} = \varphi_0 e^{-m^2 t^2/3},\end{aligned}$$

where we used $H(t) = 1/2t$ and $a(t) \propto \sqrt{t}$ supposing the radiation dominated era. φ_+ is not suitable because it is singular. Noting that $H \gg m \Leftrightarrow mt \ll 1$, the solution$\varphi = \varphi_-$ can be approximated as constant: at the early times, φ is frozen at the initial value $\varphi_0 \sim f_a$ because of the friction term $3H\dot{\varphi}$.

2. $H \ll m_a$

After cooling, φ behaves as

$$\begin{aligned}\varphi_\pm &= \varphi_1 e^{\pm i\int_{t_1}^t m_a(t)dt + \alpha} \exp\left(-\frac{3}{2}\int_{t_1}^t H(t')dt'\right) \\ &= \varphi_1 e^{\pm i\int_{t_1}^t m_a(t)dt + \alpha} \left(\frac{t_1}{t}\right)^{3/4} = \varphi_1 e^{\pm i\int_{t_1}^t m_a(t)dt + \alpha} \left(\frac{a(t_1)}{a(t)}\right)^{3/2}\end{aligned} \tag{2.7}$$

where t_1 is the time defined by $H(t_1) \sim m_{a0}$, $\varphi_1 \sim \varphi_0$, and α a phase. The energy density for the era $H \ll m_a$ is calculated to be

$$\rho_a = \frac{1}{2}\dot{\varphi}^2 + \frac{1}{2}m_a^2\varphi^2 \sim \frac{1}{2}m_a^2\varphi_1^2\left(\frac{a(t_1)}{a(t)}\right)^3. \tag{2.8}$$

This dilution behavior is akin to that of non-relativistic matter.

Using

$$\frac{T(t)}{T(t_1)} = g_*^{1/3}\left(\frac{a(t_1)}{a(t)}\right)$$

and the definition of t_1

$$m_a = H(t_1) = \sqrt{\frac{8\pi G}{3}}\sqrt{\frac{g_*}{2} \times 4\sigma T_1^4} = \sqrt{\frac{4\pi^3 G g_*}{45}}T_1^2,$$

where σ is the Stephan-Boltzmann constant $\sigma = \pi^2/90$, Eq. 2.8 gives

$$\rho_a\left(t_{\text{present}}\right) = \frac{1}{2} m_a^{1/2} g_*^{-1/4} \varphi_1^2 \left(\frac{4\pi^3 G}{45}\right)^{3/4} T_{\text{present}}^3.$$

Assuming $\varphi_1 \sim \varphi_0 \sim f_a$ and using Eq. 2.5, we obtain

$$\Omega_a = \frac{\rho_a}{\rho_c} \sim \left(\frac{m_a}{10^{-5}\,\text{eV}}\right)^{-3/2}.$$

The axion with the mass $m_a \sim 10^{-5}$eV thus can explain the right abundance of dark matter today.

This scenario, called the misalignment mechanism, may also explain the feasibility of hidden photons to be the main component of dark matter. We explain this possibility in detail in the next chapter.

2.3 Direct detection experiments

As described in Sec. 2.1, the discrepancy between luminous mass and total mass has been confirmed for several distance scales. Although these evidences strongly support the existence of dark matter, its direct/indirect detection has not yet been achieved. Nowadays, a lot of experiments have been running or planned for dark matter detection.

Indirect detection is one of the courses for the confirmation of dark matter, which aims the detection of products of dark matter annihilations. We list the channels for indirect dark matter detection in the following (for review, see, e.g., Ref. [75]):

- Gamma-ray detection
  Dark matter density is expected to be high near the centers of galaxies, which may increase the rate of dark matter annihilation and enable the indirect detection. Dwarf galaxies, whose dark matter density can be determined better than other targets, are also studied extensively.

- Charged cosmic-ray
  Anti particles, such as antiprontons or positrons, created by dark mater annihilations may be detected as an increase in the positron/electron or antiproton/proton ratio.

- Neutrinos
  Dark matter particles may be trapped in the gravity potential of the Sun. Neutrinos produced in the annihilation can be used to search for dark matter in the Sun because they can penetrate the dense medium of the Sun.

Particle colliders, such as the Large Hadron Collider (LHC), also have an ability to search for the dark matter. On the contrary to the indirect detection, colliders try to produce dark matter from ordinary Standard Model particles.

Apart from these two methods, direct detection experiments search for effects in the apparatus in the laboratory caused by dark matter particles. Fig.2.8 summarizes three pathways for dark matter investigation. In the following, we describe the basics and the status of direct detection experiments.

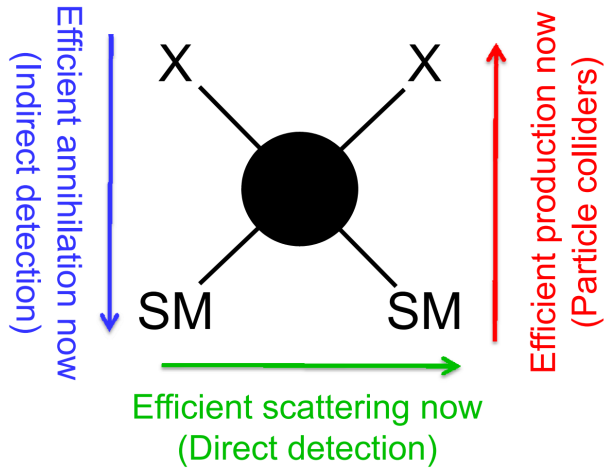

Figure 2.8: Three pathways for dark matter investigation[8]. Indirect detection searches for products of dark matter annihilation, and particle colliders aim to produce dark matter from Standard Model particles, while direct detection experiments look for effects in SM particles caused by dark matter particles.

2.3.1 WIMP

As described in Sec. 2.1, our Milkyway galaxy also is thought to be filled with dark matter, and its density around the Solar system is estimated as Eq.2.1. As a result, dark matter particles may leave some effects on the material in the laboratory, though the effects are assumed to be extremely faint.

WIMPs may be detected via nuclear recoil. Assuming the mass $m_\chi \sim 100\,\mathrm{GeV}$, the kinetic energy of WIMPs would be

$$E_{\mathrm{kin}} = \frac{1}{2} m_\chi v^2 \sim 50\,\mathrm{keV} \times \left(\frac{m_\chi}{100\,\mathrm{GeV}}\right),$$

and they would cause the same order of energy deposit to the material in the laboratory.

The rate of the scattering is approximately given by

$$R \approx n_{\mathrm{CDM}}^{\mathrm{local}} \times v \times \sigma \times N, \tag{2.9}$$

where $n_{\mathrm{CDM}}^{\mathrm{local}} = \rho_{\mathrm{CDM}}^{\mathrm{local}}/m_\chi$ is the number density of dark matter particles, σ the cross-section, N the number of the nuclei in the target. The de Broglie wave length of WIMPs in the galaxy is

$$\lambda = \frac{2\pi}{m_\chi v} \sim 10\,\mathrm{fm} \times \left(\frac{100\,\mathrm{GeV}}{m_\chi}\right).$$

For nuclei with atomic number A, the crosssection σ (for spin-independent case) would be proportional to A^2 rather than A because λ is larger than the size of atomic nuclei $\sim 10\,\mathrm{fm}$, which induces coherent scattering. Assuming $\sigma = A^2\sigma_p$ and using Eq.2.9, the expected event rate would be

$$R \approx \frac{10\,\mathrm{counts}}{\mathrm{year}} \frac{\rho_{\mathrm{CDM}}^{\mathrm{local}}}{0.3\,\mathrm{GeV/cm^3}} \frac{100\,\mathrm{GeV}}{m_\chi} \frac{v}{10^{-3}c} \frac{A}{56} \frac{m_{\mathrm{target}}}{100\,\mathrm{kg}} \frac{\sigma_p}{10^{-42}\,\mathrm{cm^2}},$$

where we used $N = m_{\mathrm{target}}/m_A \sim m_{\mathrm{target}}/(A \times m_p)$.

Apparatus for WIMP detection thus requires

- Low background
  Because the event rate is expected to be very small, quiet environment is of great importance. A large amount of effort has been paid for using radiopure materials for the instruments and the target mass.

- Large volume of the target mass
  We need $\sim 10^3$ kg target mass to obtain a significant count rate.

- Low energy threshold
  To search for low-mass WIMPs, the low energy threshold should be accomplished despite the need for background rejection.

Two sources for modulation are predicted for WIMP signal:

- Daily modulation
  Because of the rotation of the Earth, bias on the direction of nuclear recoil moves in a day. Detectors sensitive for recoil direction can use this modulation signal.

- Annual modulation
  The event rate varies a few percent because of the Earth's motion around the Sun in a year.

Searches using liquid noble gases

Detectors using liquid noble gas for the target mass enable relatively easy scaling of the mass to $\sim 10^3$ kg size, and are developed by several groups, including the XENON collaboration, the XMASS collaboration , the ArDM project [76], and the LUX collaboration [9].

Dual phase technique is widely used for sensitive detection of dark matter. Fig. 2.9 is a schematic diagram of a dual phase detector. As a result of WIMP-nucleous interaction in the liquid phase, scintillation light is produced (S1). An electric field moves the ionization electrons produced in the primary interaction to the gas phase above the liquid phase. In the gas phase, the transported electrons create electroluminescence light (S2). By measuring time between S1 and S2 (drift time), we can estimate the depth at which the interaction occurs.

Among a lot of detectors using liquid xenon for the target mass, the LUX experiment [9] is in the front line. The LUX detector is a double phase xenon detector with total xenon volume of 370 kg, in which ~ 100 kg is used as the fiducial volume. The detector is installed in the Sanford Underground Research Facility (SURF) at Homestake, South Dakota. Fig. 2.10 shows an overview of the LUX detector. A large water shield instrumented with PMTs for muon veto surrounds the cryostat, inside which liquid xenon, cathode and anode grids, and photomultiplier tubes are installed. Fig. 2.11 is a photograph taken in the water tank of the LUX apparatus. The LUX collaboration has recently published the first result from 85.3 live days of data, which found no significant excess in counts [77]. The result set the most stringent upper limit on the WIMP-nucleus cross-section in the mass region $m_\chi \gtrsim 10$ GeV.

The XENON collaboration [78] is another group using liquid xenon for the target mass. They published a result [79] based on the exposure of 224.6 live days $\times$ 34 kg by the XENON100 detector, which found no evidence for dark matter interactions. The successor of this experiment, XENON1t [80], is now under construction and the sensitivity of the XENON1t is expected to surpass that of the LUX experiment.

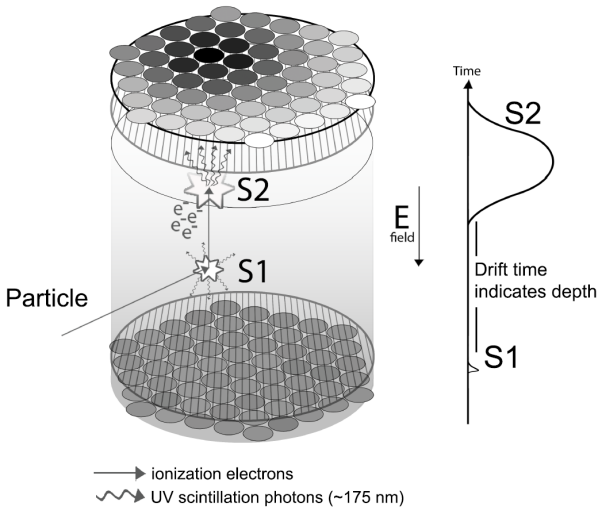

Figure 2.9: Schematic diagram of a dual phase detector. As a result of a WIMP-nucleus interaction in the liquid phase, scintillation light is produced (S1). An electric field moves the ionization electrons produced in the primary interaction to the gas phase above the liquid phase. In the gas phase, the electrons create electroluminescence light (S2). By measuring time between S1 and S2 (drift time), we can estimate the depth at which the interaction occurs. Taken from Ref.[9]

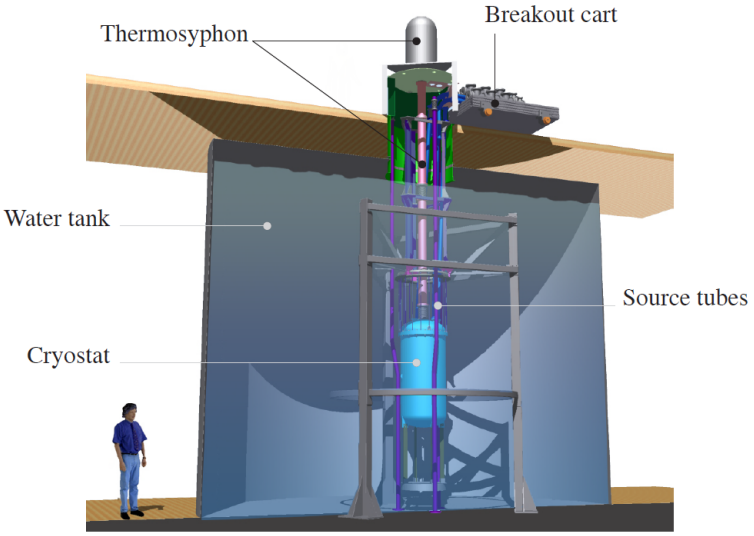

Figure 2.10: Overview of the LUX detector. Taken from Ref.[9]

Figure 2.11: Inside the water tank of the LUX detector. 20 large PMTs are installed for veto. Taken from Ref. [10].

The XMASS collaboration uses a single phase detector filled with liquid xenon located at the Kamioka Observatory in Japan, and recently announced the result of 359.2 live days $\times$ 832 kg of exposure, where they found a slight negative amplitude for the annual modulation [81]. The result excludes the most part of the DAMA/LIBRA favored region described below.

There are several experiments using liquid argon instead of liquid xenon. Argon is much cheaper than xenon, which enables to have a huge target volume. The ArDM [76] is a double phase detector with 1,100 kg argon in total. It is installed at the Canfranc laboratory, and is now under operation.

Solid detectors: semiconductors and scintillators

Semiconductor detectors with high purity are also used to search for WIMP dark matter. These detectors collect ionization electrons and/or phonons produced by scattering of WIMPs off nuclei.

The CoGeNT collaboration used a 440 g Germanium detector to search for WIMPs in the Soudan Underground Laboratory. The CoGeNT, an acronym for Coherent Germanium Neutrino Technology, was originally a plan aiming at the detection of coherent neutrino-neucleus scattering from nuclear power plants, and later the detector was used for WIMP detection. The adoption of a Point Contact detector greatly reduces the electric noise and enables lowering the energy threshold. Fig. 2.12 shows a comparison between a Point Contact detector and a standard coaxial design. The CoGeNT collaboration claimed the positive signal [82, 83], which prompted a huge controversy.

The CDMS collaboration uses detectors cooled down to mK temperature. This enables measurements of phonons, together with ionization electrons, created in a WIMP-nucleus scattering. Fig. 2.13 shows a schematic of the detector, iZIP, used in the SuperCDMS. The Ge crystal has dimensions of 76 mmϕ $\times$ 25 mm, and top and bottom faces are implemented with phonon sensors and electrodes to read out the ionization signal. Recently, the CDMS collaboration announced a possible excess of events [84]. In the exposure of the silicon detectors of the CDMS II for 140 kg $\cdot$ day, they found three WIMP-candidate events. The allowed region calculated from this result shows some overlap with the claim of the CoGeNT experiment.

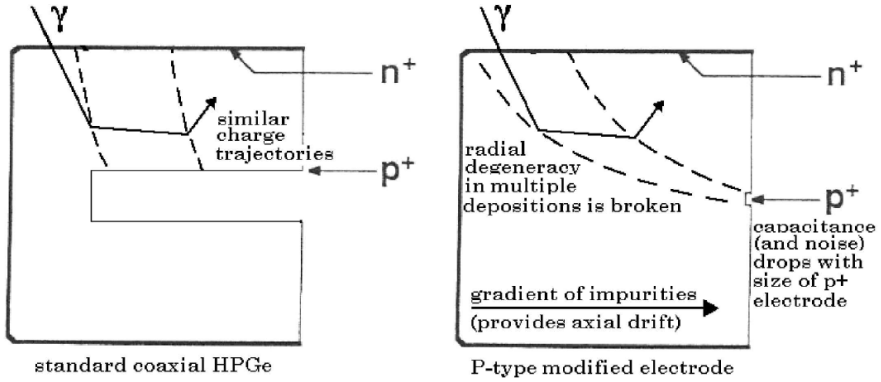

Figure 2.12: Comparison of designs of Germanium detectors[11]. The crosssection of a standard coaxial detector is shown on the left, while a P-type point contact detector on the right. Small electrodes lead to small capacitance, which result in low electric noise.

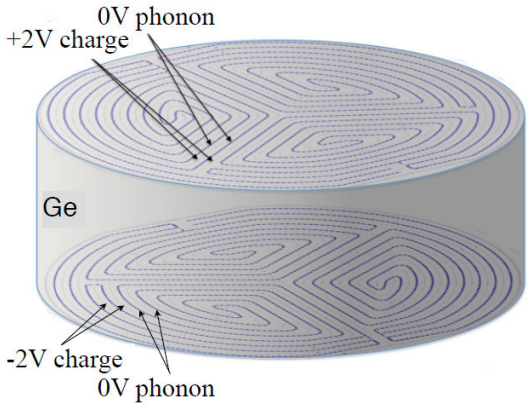

Figure 2.13: Schematic view of the detector, iZIP, used in the CDMS experiment. The Ge crystal has dimensions of 76 mm$\phi \times$ 25 mm. Top and bottom faces are implemented with phonon sensors and electrodes for the ionization signal. Taken from Ref. [12].

Scintillation detectors have been used from the early era of the WIMP direct detection. One of the most famous experiments using scintillators is the DAMA experiment. In 1997, the DAMA collaboration claimed the positive annual modulation signal [85] by operating CsI(Tl) scintillators, and subsequent measurements also support the claim, attaining 8.9σ deviation from no-modulation hypothesis [86]. The report evoked long-standing controversy in the direct-detection community, but a lot of experiments with different detection methods have denied the parameter region favored by the DAMA result. Recently, the KIMS collaboration [87] announced the result of the exposure of 104.4 kg CsI(Tl) scintillators, where they denied the DAMA favored region around $m_\chi \sim 60\,\mathrm{GeV}$ despite using the same target material.

Other experiments employing scintillation detectors are now operating or under construction. The ANAIS project [88] is planning to use a 100 kg NaI(Tl) scintillator at the underground laboratory of Canfranc, while the DM-ice collaboration [89] is preparing for the operation of NaI(Tl) scintillators at the center of the IceCube array.

Gas detectors

Although gas detectors have a disadvantage from their low density compared to solid or liquid detectors, they are widely studied for WIMP detection because of the possibility to measure the direction of nuclear recoils. Using the direction information in analysis, we can use the daily modulation to distinguish the WIMP signal from noise. This advantage provides a concrete evidence for dark matter if we find positive signal, and enables further study for the nature of the dark matter halo of the Galaxy.

The NEWAGE (an acronym for NEw generation WIMP-search with Advanced Gaseous tracking device Experiment) collaboration in Japan uses the μ-TPC (Fig.2.14) for WIMP detection. The μ-TPC consists of a detection volume of $30 \times 30 \times 41\,\mathrm{cm}^3$ filled with CF_4 gas, a gas electron multiplier, and a micro-pixel chamber for readout. Nuclei scattered by WIMPs make a track of ionization in the gas, then the ionized electrons are drifted to the μ-PIC. By measuring the drift time, the information of z-axis can be obtained together with xy position by μ-PIC. The present sensitivity does not reach to the level of other experiments using liquid or solid detectors.

The experimental bounds and the region of the claim for WIMPs are plotted in Fig. 2.15. The vertical axis shows the crosssection of WIMP-nucleus scattering, and the horizontal axis shows the WIMP mass m_χ. Colored areas at the bottom-right are regions favored by theories [90, 91]. Experimental apparatus for WIMP direct detection have been becoming more and more sensitive. In the next generation of detectors using liquid noble gas, such as LZ, DARWIN, and the MAX project, neutrino backgrounds from e.g. the Sun may cause serious degradation of sensitivity [92]. There are several ways to go beyond the sensitivity limit from neutrinos:

- Improving the estimation of the neutrino fluxes from both theoretical and experimental ground
- Making use of the annual modulation effect
- Employing detectors sensitive to the direction of nuclear recoils.

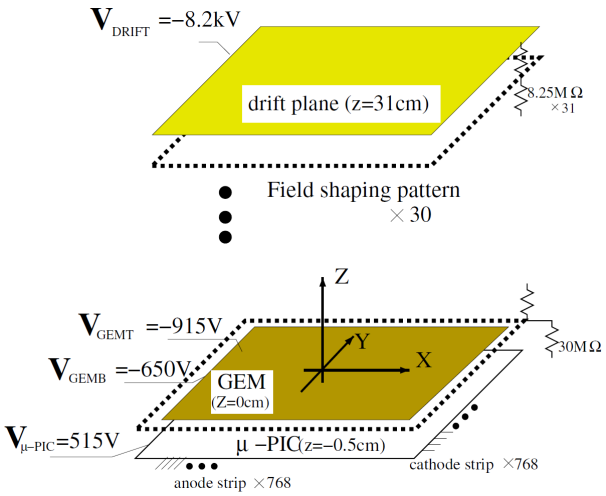

Figure 2.14: Schematic of the μ-TPC used in the NEWAGE group.The μ-TPC consists of a detection volume of $30 \times 30 \times 41\,\mathrm{cm}^2$ filled with CF_4 gas, a gas electron multiplier, and a micro-pixel chamber for readout. Taken from Ref.[13]

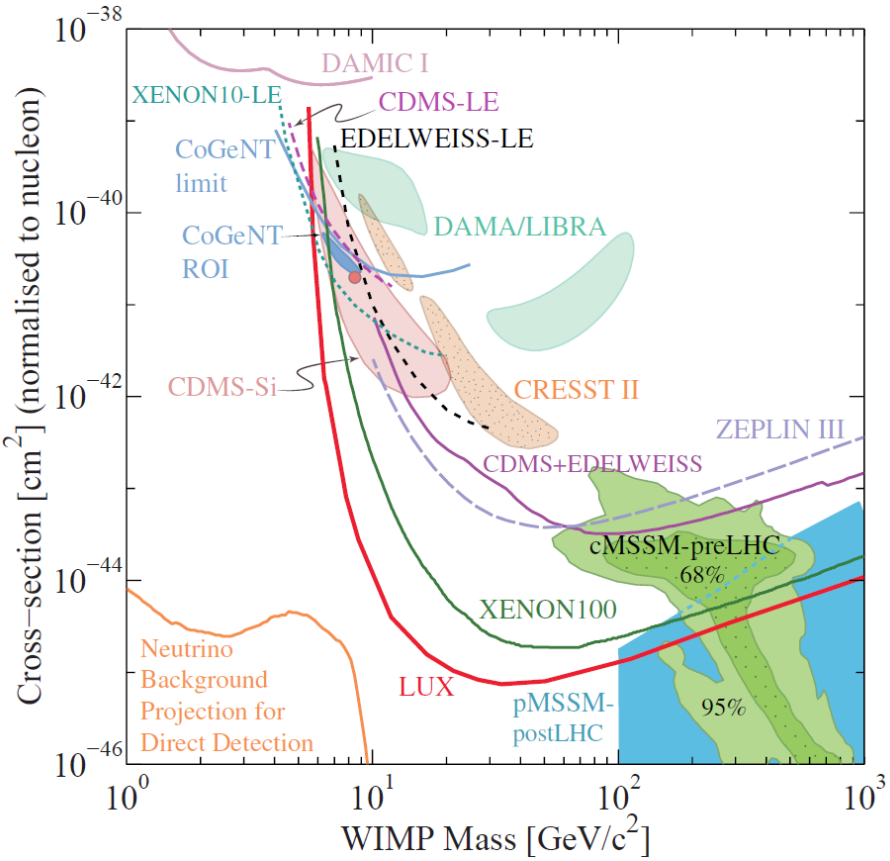

Figure 2.15: Experimental bounds and the regions of detection claims for spin-independent coupling. The vertical axis shows the crosssection of WIMP-nucleus scattering, and the horizontal axis shows the WIMP mass m_χ. Taken from Ref.[14].

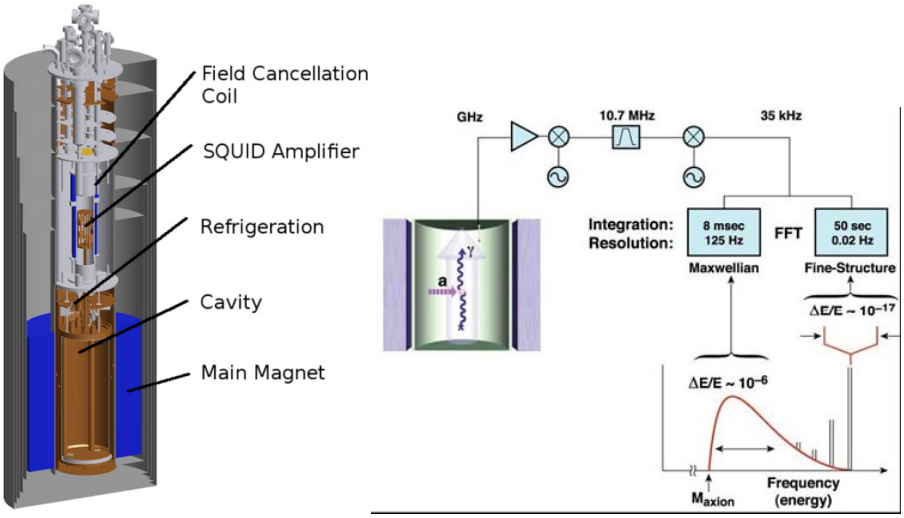

Figure 2.16: The concept of the ADMX experiment. (Left) Design of the ADMX detector. (Right) Schematic of the search method using a microwave cavity. Taken from Ref.[15]

2.3.2 Axion

Axions are assumed to be very light $m_a \sim \mu$eV compared to the WIMP mass $\gtrsim$ GeV, and cannot be detected via nucleus scattering. The axion field φ, fortunately, is expected to have an interaction with the Standard Model electromagnetic field via the following term:

$$g_{a\gamma\gamma}\varphi \mathbf{E} \cdot \mathbf{B}, \tag{2.10}$$

where $g_{a\gamma\gamma}$ is a coupling constant of order $\alpha/2\pi f_a$, and $\mathbf{E}$ and $\mathbf{B}$ are the electric field and the magnetic field, respectively.

The Axion Dark Matter Experiment (ADMX) uses microwave cavity with a strong magnetic field to convert axions in the Galactic halo to an electric signal. Fig. 2.16 shows a schematic view of the method using a microwave cavity, and the design of the ADMX detector. The dark matter axion in the Galaxy induces the excitation of the electric field in the cavity under a strong magnetic field. The excitation is then read out by the SQUID amplifier. The axion signal would be seen as a spike in the spectrum, and the position of the signal corresponds to the mass of the axion m_a.

The exclusion plot from the recent result of the ADMX experiment [16] is shown in Fig. 2.17. The current experimental reach is limited in both the sensitivity and the frequency range.

Apart from DM axion surveys, there are a lot of activities searching for axions created in the Sun or by creating them in a laboratory. They solely assume the interaction between axions and Standard Model particles, such as the one described in Eq. 2.10.

Solar axion helioscopes [93] searches for axions produced in the inner part of the Sun, then coming to the Earth. Making use of the interaction described in Eq. 2.10, incoming axions are converted to ordinary photons under strong magnetic field, then X-ray detectors catch the signal (Fig. 2.18). Tokyo Axion Helioscope, Sumico (Fig. 2.19), is the first dedicated apparatus to search for solar axions [94]. The CAST experiment [95] at CERN is the successor of Sumico, and now the next generation helioscope, IAXO [88], is being planned.

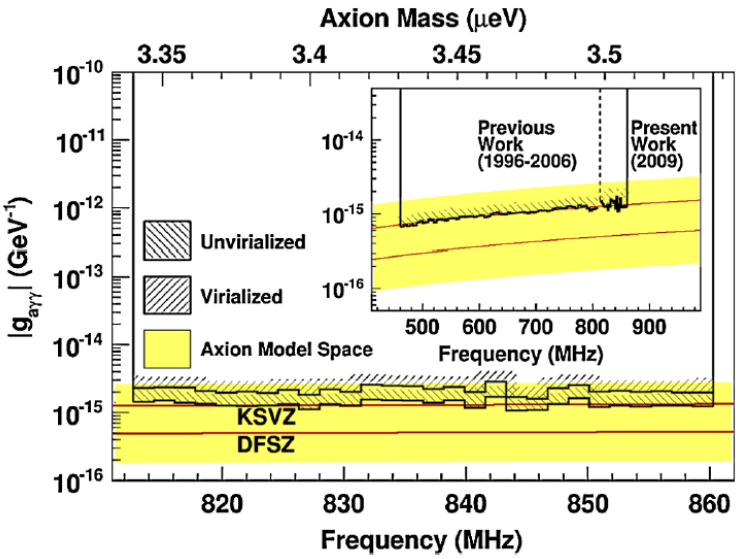

Figure 2.17: The recent result of the ADMX experiment[16].

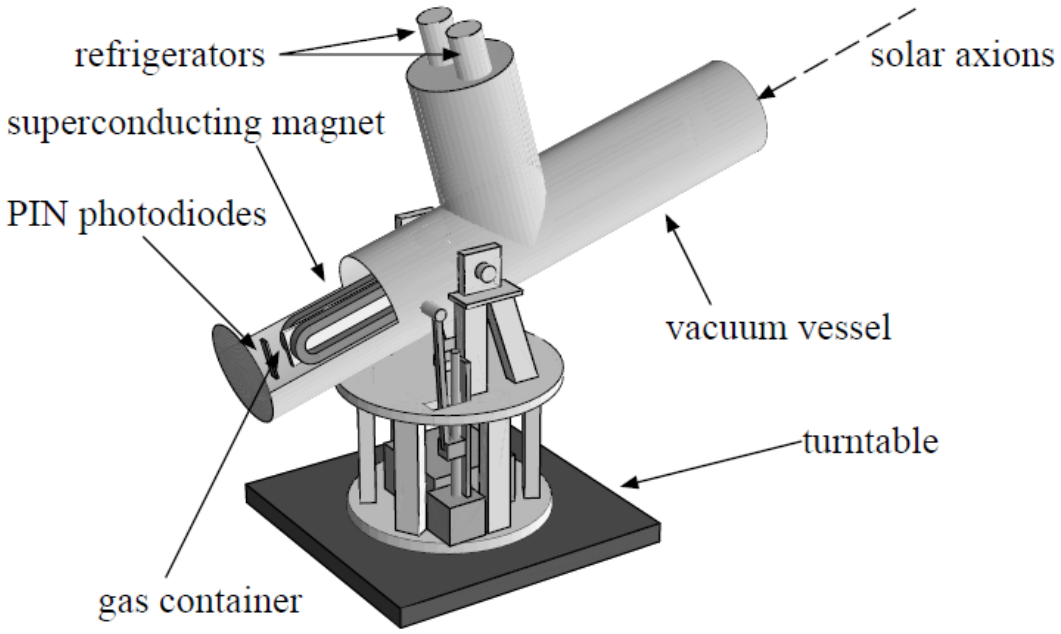

Figure 2.18: Schematic of a solar axion helioscope. Incoming axions are converted to ordinary photons under strong magnetic field, then X-ray detectors catch the signal.

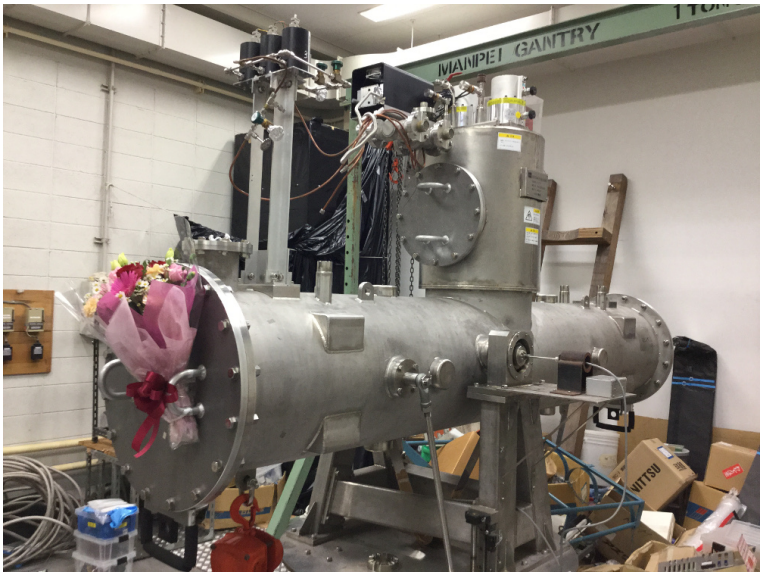

Figure 2.19: Tokyo Axion Helioscope, Sumico.

The interaction of axions with Standard Model particles is extremely weak. As a consequence of this nature, we can test whether axion exists or not by a 'Light Shining through a Wall' (LSW) set-up. Axions are produced from intense laser sources under strong magnetic fields, then they pass through a wall which can perfectly block ordinary photons. Photons are now re-generated from axions by applying a strong magnetic field, and then detected by a photodetector. These experiments are also sensitive to hidden photons, and we describe it in detail in the next chapter.

The ALPS experiment [96] at DESY, equipped with a HERA dipole magnet, uses LSW method to search for Axion-Like Particles (ALP). The result of a test run is reported in Ref. [97]. An update to experiment is planned [98] and the experimental reach may surpass existing bounds coming from other experiments.

Figure 2.20 depicts experimental bounds and the region of interest in the parameter space of the axion model. The vertical axis shows the coupling constant $g_{a\gamma\gamma}$ and the horizontal axis the mass of the axion m_a. The hatched area shows the parameter region suited as a strong-CP solution.

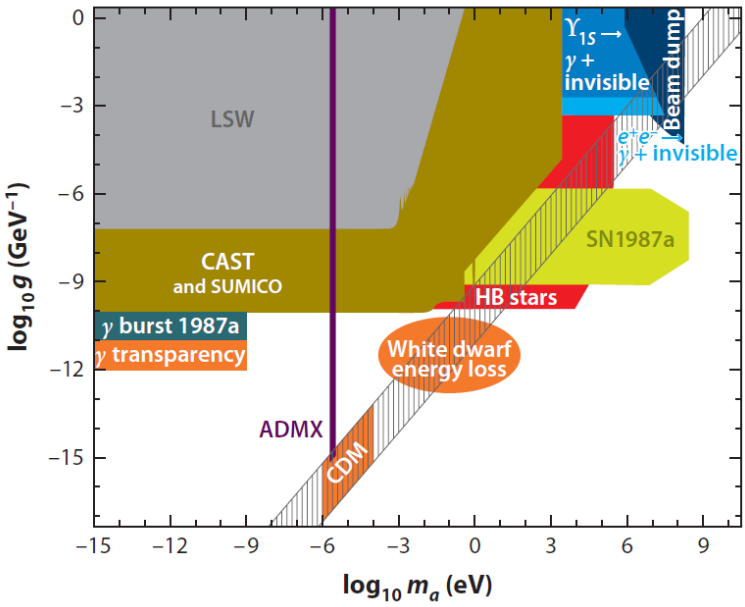

Figure 2.20: Experimental bounds and the region of interest in the parameter space of the axion. Taken from Ref.[17].

Chapter 3

Hidden photon

The study of the Standard Model of particle physics and cosmology prompts a lot of problems, including

- Strong CP problem
  Non-perturbative effects of the strong interaction predicts a term

  $$\mathcal{L} \supset -\frac{g^2\theta}{32\pi^2}\tilde{F}^{a\mu\nu}F^a_{\mu\nu},$$

  where θ is naturally assumed to be a value of $\mathcal{O}(1)$, which however is experimentally confirmed to be $|\theta| < 10^{-10}$.

- Hierarchy problem
  Unnatural fine tuning is required to settle the mass of the higgs boson, which is predicted to diverge quadratically.

- Flatness problem
  Density parameter Ω is required to be fine tuned to unity with an accuracy of $\mathcal{O}(10^{-15})$ at the early era of the universe.

- Integration of gravity
  Quantum field theory cannot contain gravity, which though seems to be a fundamental force of the nature.

A lot of theories have been invented to overcome the problems listed above, and not a few of them predict new symmetries in addition to the Standard Model gauge symmetry $\mathrm{SU}(3) \times \mathrm{SU}(2) \times \mathrm{U}(1)$ [17]. Theories beyond the Standard Model have been searched by particle colliders, such as the Large Hadron Collider built by CERN, utilizing high-energy techniques. On the other hand, we can explore physics beyond the Standard Model with low-energy techniques and precision measurements.

Theories beyond the Standard Model sometimes predict an extra U(1) symmetry, and phenomenological studies on the symmetry and the gauge boson, dubbed 'hidden photon', 'hidden-sector photon', 'paraphoton' or 'dark photon', have received growing attention. The hidden photon (HP) field X^μ might interact with the constituents of the Standard Model via a kinetic mixing to the ordinary electromagnetic field

$$-\frac{\chi}{2}F_{\mu\nu}X^{\mu\nu},$$

	Mass	Coupling constant
A_1	m_1	e_1
A_2	$m_2(> m_1)$	e_2

Table 3.1: Masses and coupling constants of A_1, A_2 fields assumed in the model in Ref. [47].

where $F_{\mu\nu} = \partial_\mu A_\nu - \partial_\nu A_\mu$ is the field strength of the electromagnetic field A^μ, $X_{\mu\nu} = \partial_\mu X_\nu - \partial_\nu X_\mu$ the field strength of the hidden-sector field X^μ, and χ the photon-HP mixing parameter. In addition to the kinetic mixing, hidden photons might have a mass $m_{\gamma'}$ via the Higgs or the Stueckelberg mechanism. These properties enrich phenomenology of hidden photons, where, for example, hidden photons are assumed to solve the muon $g-2$ problem [99], or are suspected as a candidate for dark matter [25]. The kinetic mixing and the non-zero mass also enable experimental searches for hidden photons.

In this chapter, we review the theory of hidden photons, and experimental searches performed or planned with a variety of methods.

3.1 Hidden photon

A phenomenology of an extra U(1) gauge field was argued, for the first time, by L. Okun [47] to measure the depth of our knowledge to the electromagnetic interaction. At a later time, it has been found to appear as a part of extensions to the Standard Model, e.g. super gravity or string theories [100].

3.1.1 Paraphoton model by Okun

In 1982, L. Okun introduced an extension to the electromagnetism, and tested the model with experimental results [47]. Another U(1) field in addition to the electromagnetic field would modify the electrostatic potential and make a deviation of the propagation eigenstate from ordinary photons, which might be tested by precise experiments in laboratories, or studies on astronomical sources.

The model argued in Ref. [47] consists of two fields A_1, A_2 with masses and coupling constants listed in Tab. 3.1.

The model is described by the Lagrangian

$$\mathcal{L} = -\frac{1}{4}F_{i\mu\nu}F_i^{\mu\nu} + \frac{1}{2}m_i^2 A_{i\mu}A_i^\mu + j_\mu e_i A_{i\mu}, \tag{3.1}$$

where

$$F_{i\mu\nu} = \partial_\mu A_{i\nu} - \partial_\nu A_{i\mu} \qquad (i = 1,\, 2)$$

and j_μ is the ordinary electromagnetic current.

Potential

The existence of another field A_2 modifies the shape of the electromagnetic potential.

For extremely small distances $r \ll 1/m_2 < 1/m_1$, A_1 and A_2 behave identically as massless fields, and the fine structure constant would be

$$\frac{e^2}{4\pi} = \alpha = \alpha_1 + \alpha_2 = \frac{e_1^2}{4\pi} + \frac{e_2^2}{4\pi}$$

for the potential

$$U(r) = \frac{\alpha}{r},$$

which is in proportion to $1/r$ in accordance with the standard electromagnetism.

For $1/m_2 \lesssim r \ll 1/m_1$, non-negligible mass m_2 modifies the potential to

$$U(r) = \frac{\alpha_1}{r} + \frac{\alpha_2 e^{-m_2 r}}{r}\,. \tag{3.2}$$

In ordinary electromagnetism, electric fields would vanish and the electric potential would be constant inside a uniformly charged sphere. However, it does not hold for the modified potential in Eq. (3.2). The potential $V(r)$ of a uniformly charged sphere of radius R for an arbitrary potential $U(r)$ is given by

$$V(r) = \frac{1}{2Rr}\left[f(R+r) - f(|R-r|)\right]$$
$$\left(f(r) = \int_0^r sU(s)\,ds\right),$$

where r is a distance from the center of the sphere. Substitution of (3.2) to the formula for $f(r)$ yields

$$f(r) = \alpha_1 r + \frac{\alpha_2}{m_2}\left(1 - e^{-m_2 r}\right).$$

Assuming a charged sphere with radius R_1 and a concentric uncharged sphere with smaller radius R_2, the potential difference $V(R_1) - V(R_2)$ would be

$$\begin{aligned} V(R_1) - V(R_2) &= \frac{\alpha_2}{\alpha_1} e^{-m_2 R_1}\left(\frac{\sinh m_2 R_2}{m_2 R_2} - \frac{\sinh m_2 R_1}{m_2 R_1}\right) \\ &\quad \times \left[1 + \frac{\alpha_2}{\alpha_1} e^{-m_2 R_1}\left(\frac{\sinh m_2 R_1}{m_2 R_1}\right)\right]^{-1} V(R_1)\,, \end{aligned}$$

which results in

$$\frac{V(R_1) - V(R_2)}{V(R_1)} = \begin{cases} \frac{\alpha_2}{\alpha}\frac{m_2^2}{6}\left(R_2^2 - R_1^2\right) & (m_2 R_1 \ll 1) \\ \frac{\alpha_2}{\alpha}\frac{1}{2m_2 R_1} & (m_2 R_1 \gg 1) \end{cases}$$

in the two extreme cases. We thus find that we can investigate the deviation from the ordinary electromagnetism by measuring a difference between the potential.

Oscillation

The interaction term in the Lagrangian Eq. (3.1)

$$\mathcal{L}_{\rm int} = j_\mu e_i A_{i\mu} = j_\mu e \times \frac{e_1 A_1 + e_2 A_2}{e}$$

tells that the linear superposition

$$B_1 = \frac{e_1 A_1 + e_2 A_2}{e}$$

interacts with the current j_μ, while the superposition orthogonal to B_1

$$B_2 = \frac{-e_2 A_1 + e_1 A_2}{e}$$

does not interact with ordinary matter. We thus find that the interaction eigenstates B_1, B_2 differ from the mass eigenstates A_1, A_2, which induces 'oscillation' between B_1 and B_2 along their propagation, similarly to the neutrino oscillation.

Wave numbers k_1 and k_2 of A_1 and A_2 field differ from its frequency ω as a result of non-zero mass of the fields by

$$\begin{aligned} k_1 &= \left(\omega^2 - m_1^2\right)^{1/2} \simeq \omega - \frac{m_1^2}{2\omega} \\ k_2 &= \left(\omega^2 - m_2^2\right)^{1/2} \simeq \omega - \frac{m_2^2}{2\omega} \\ q &\equiv k_1 - k_2 \simeq \frac{(m_2^2 - m_1^2)}{2\omega} \simeq \frac{m_2^2}{2\omega}. \end{aligned}$$

The difference between the wave numbers k_1 and k_2 mixes the active photon B_1 and the sterile photon B_2 during propagation. The active field B_1 is modified at some position r from the point of emission as

$$\begin{aligned} B_1 \;\rightarrow\; & \frac{1}{e}\left(e_1 A_1 e^{-i(\omega t - k_1 r)} + e_2 A_2 e^{-i(\omega t - k_2 r)}\right) \\ & = e^{-i(\omega t - k_1 r)}\left(e_1 A_1 + e_2 A_2 e^{-iqr}\right)\frac{1}{e} \\ & = e^{-i(\omega t - k_1 r)}\left(\left(e_1^2 + e_2^2 e^{-iqr}\right) B_1 + e_1 e_2\left(-1 + e^{-iqr}\right) B_2\right)\frac{1}{e^2}. \end{aligned}$$

We thus find that the relative intensity of the sterile field B_2 oscillates as

$$\rho_s = 4\frac{\alpha_1\alpha_2}{\alpha^2}\sin^2\left(\frac{qr}{2}\right) \tag{3.3}$$

and the intensity of the active field B_1 is

$$\rho_a = 1 - 4\frac{\alpha_1\alpha_2}{\alpha^2}\sin^2\left(\frac{qr}{2}\right).$$

This 'oscillation' between active and sterile components might be used to test the existence of paraphotons, and actually utilized by 'Light Shining through a Wall' experiments and solar hidden photon searches as reviewed below.

	Coupling to A_1	Coupling to A_2	Mass
f_1	e_1	0	m_1
f_2	0	e_2	m_2
f_{12}	e_1	e_2	m_{12}
f'_{12}	e_1	$-e_2$	m'_{12}

Table 3.2: Coupling constants and masses of fermions which appear in the model in Ref. [48].

3.1.2 Kinetic mixing by Holdom

Introduction of an additional U(1) field was argued from another point of view by B. Holdom in 1986 [48], where two U(1) gauge fields and fermions carrying both charges produce a kinetic mixing

$$-\frac{\chi}{2}F_{1\mu\nu}F_2^{\mu\nu}$$

between two fields, effectively in low energy limit.

The model in Ref [48] introduces four fermions with charges and masses listed in Tab. 3.2, and two U(1) gauge fields A_1^μ of $\mathrm{U}_1(1)$ and A_2^μ of $\mathrm{U}_2(1)$. The masses in Tab. 3.2 are assumed to fulfill the relation

$$m'_{12} > m_{12} > m_1 \simeq m_2.$$

The fermions f_1 and f_2 do not interact with each other in tree level by definition. However, fermions carrying both charges would make a loop to couple f_1 and f_2.

In this model, two diagrams depicted below are allowed:

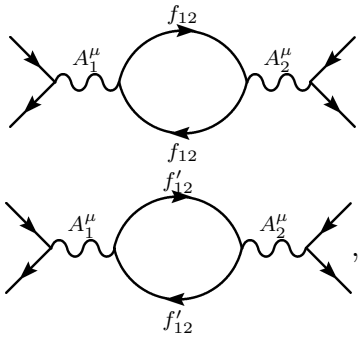

corresponding to two fermions f_{12} and f'_{12} charged under both gauges. The fermions f_{12} and f'_{12} are defined to have charges of $\mathrm{U}_2(1)$ field with opposite signs, which works to cancel the contributions of two diagrams. The assumption $m'_{12} > m_{12}$ leaves a slight residue, and the effective Lagrangian of the model at some scale Λ, $m_{1,2} < \Lambda < m_{12}$ would be

$$\mathcal{L} = -\frac{\chi_1}{4}F_1^{\mu\nu}F_{1\mu\nu} - \frac{\chi_2}{4}F_2^{\mu\nu}F_{2\mu\nu} - \frac{\chi}{2}F_1^{\mu\nu}F_{2\mu\nu}$$

where

$$\chi = \frac{e_1 e_2}{6\pi^2}\ln\left(\frac{m'_{12}}{m_{12}}\right).$$

The kinetic mixing term appeared above can be eliminated by a redefinition of gauge fields A_1 and A_2. New gauge fields $A'^{\mu}_{1,2}$ are defined by

$$\begin{aligned} A'^{\mu}_{1,2} &= D^{1/2} O^T A^{\mu}_{1,2} \\ A_{1,2}{}^{\mu} &= O D^{-1/2} A'^{\mu}_{1,2} \end{aligned}$$

where D is a diagonal matrix and O an orthogonal matrix, which satisfies

$$\begin{pmatrix} \chi_1 & \chi \\ \chi & \chi_2 \end{pmatrix} = O D O^{\mathrm{T}}.$$

Orthonormal combinations of the A' fields

$$A''^{\mu}_{1,2} = \begin{pmatrix} \cos\theta & -\sin\theta \\ \sin\theta & \cos\theta \end{pmatrix} A'^{\mu}_{1,2}$$

also do not have the kinetic mixing term in the Lagrangian written in terms of them. Now A''_1 and A''_2 are defined to couple and not to couple to f_1, respectively. We thus have $A''_1 \propto A_1$ and

$$e_1 A^{\mu}_1 = e_1 \left(O D^{-1/2} A'^{\mu} \right)_1 = e_1 \chi_1^{-1/2} A''^{\mu}_1 \equiv e''_1 A''^{\mu}_1$$

to lowest order of $\chi_1 - 1$, $\chi_2 - 1$, and χ. We similarly find

$$\begin{aligned} e_2 A^{\mu}_2 &= e_2 \left(O D^{-1/2} A'^{\mu} \right)_2 \\ &= e_2 \chi_2^{-1/2} \left(A''^{\mu}_2 \cos\theta - A''^{\mu}_1 \sin\theta \right) \\ &\equiv e''_2 \left(A''^{\mu}_2 \cos\theta - A''^{\mu}_1 \sin\theta \right) \end{aligned}$$

where $\sin\theta = \chi$ to lowest order. Therefore, A''^{μ}_1 couples to both fermions f_1 and f_2, and the ratio of the couplings would be

$$\epsilon = -\frac{e''_2}{e''_1} \chi$$

3.2 Experimental search for hidden photons

The kinetic mixing $-(\chi/2) F_{\mu\nu} X^{\mu\nu}$ and the non-zero mass of hidden photons $(m^2_{\gamma'}/2) X_{\mu} X^{\mu}$ allow a variety of experimental methods to search for hidden photons. Figure 3.1 is a plot of the $\chi - m_{\gamma'}$ parameter space of the model of hidden-sector photons [17]. The vertical axis is the photon-HP mixing parameter χ in logarithmic scale, and the horizontal axis shows the mass of hidden photon $m_{\gamma'}$ in logarithmic scale. The filled regions are excluded by experiments or studies on astronomical sources.

We quickly review the origins of excluded regions in Fig. 3.1 in the following.

The regions labeled "Jupiter" and "Earth" around $m_{\gamma'} \sim 10^{-14}\,\mathrm{eV}$ are constraints obtained from observations of the magnetic fields of the Jupiter and the Earth [101, 102, 103], respectively. If there exist the hidden photon field in addition to the ordinary electromagnetic field, the shape of the magnetic field is modified from its expectation from the ordinary electromagnetism.

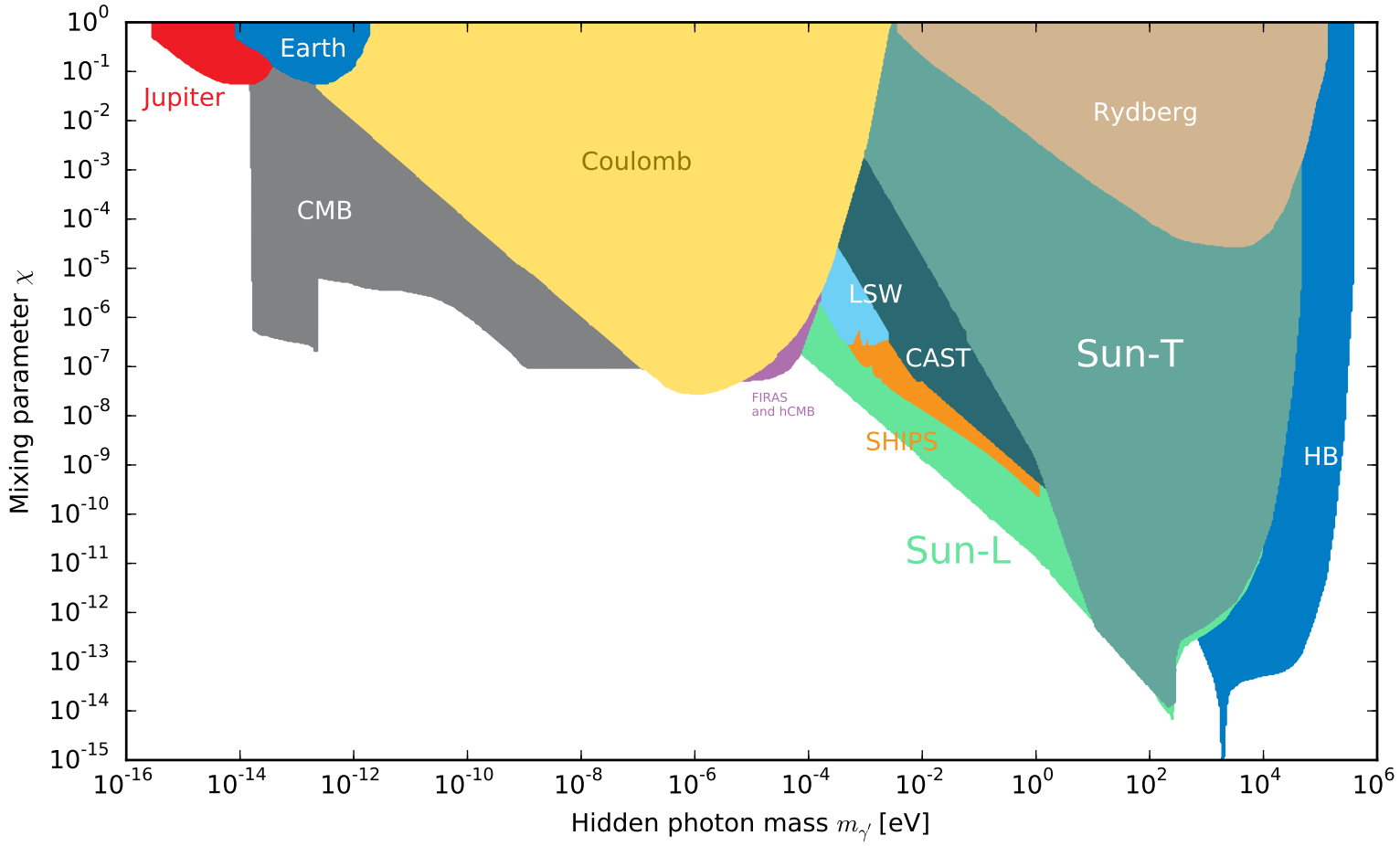

Figure 3.1: Plot of the $\chi - m_{\gamma'}$ parameter space. The colored regions are excluded by experiments or studies on astronomical sources [17].

The limit of yellow region labeled "Coulomb" is obtained by precision tests of Coulomb's inverse-square law [32], the origin of which dates back to the experiment carried out by H. Cavendish in 1773 [104]. The inverse-square law is modified as

$$U(r) = \frac{\alpha_1}{r} + \frac{\alpha_2}{r} e^{-m_{\gamma'} r}$$

by the existence of massive states (cf. Eq. (3.2)), which enables tests of the hidden photon model by precision measurements.

A similar constraint comes from the study of electric fields in atomic scales [105], which is labeled "Rydberg" around $m_{\gamma'} \sim 10^2\,\mathrm{eV}$. Depending on scales, from the size of planets to the atomic scale, experiments are sensitive in different mass ranges.

The constraint labelled "CMB" is from the observation of the spectrum of the Cosmic Microwave Background radiation by the FIRAS (Far InfraRed Absolute Spectrometer) [39, 106]. The spectrum of the CMB radiation is distorted from the ordinary black-body radiation spectrum as a consequence of the existence of hidden-sector photons.

Experiments designed for other usages sometimes have a sensitivity for hidden photons. The region labeled "CAST" is the limit translated [37] from the result of the experimental search for solar axions [107] by the CERN Axion Solar Telescope (CAST) [95], which converts axions from the Sun to X-rays via the inverse Primakov conversion using a LHC prototype dipole magnet. As we will mention below, hidden photons also would be produced in the Sun, and could be detected by the same apparatus. WIMP detectors with low energy threshold also have sensitivity to hidden photons produced in the Sun, and the constraint from the XENON data [108, 109] is shown in Ref. [110, 111].

Dedicated detectors for hidden photon searches have recently been constructed, and the region labeled "SHIPS" is the result of the experimental search using an apparatus designed for the solar hidden photon search. We will review the search for solar hidden photons in detail in Sec. 3.2.2.

"LSW" around $m_{\gamma'} \sim$ meV comes from another experimental effort, where hidden photons are created in a laboratory using high-intensity lasers. We summarize the method and apparatus in Sec. 3.2.1.

"Sun-T" and "Sun-L" are the constraints from theoretical studies on the Sun based on helioseismology. "T" only accounts for the transverse modes of hidden photons [37], while "L" includes the longitudinal mode of the massive state [40, 41].

3.2.1 LSW

Figure 3.2 shows a schematic of the method of "Light Shining through a Wall" (LSW) experiments. Photons from a light source are converted to hidden photon with a probability

$$P\left(\gamma \to \gamma'\right) \simeq 4\chi^2 \times \sin^2\left(\frac{m_{\gamma'}^2 L}{4\omega}\right), \tag{3.4}$$

where ω is the energy of the photons and L is the distance from the light source (cf. Eq. 3.3). A sufficiently thick wall prevents photons to pass through it, while hidden photons, which do not interact with ordinary matter, penetrate the wall without disturbed. Hidden photons selected out of a large amount of photons by the wall are

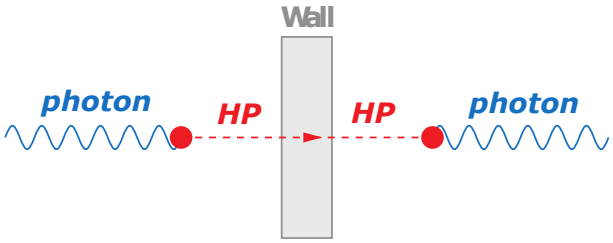

Figure 3.2: Schematic of LSW experiments. Adapted from Ref. [17].

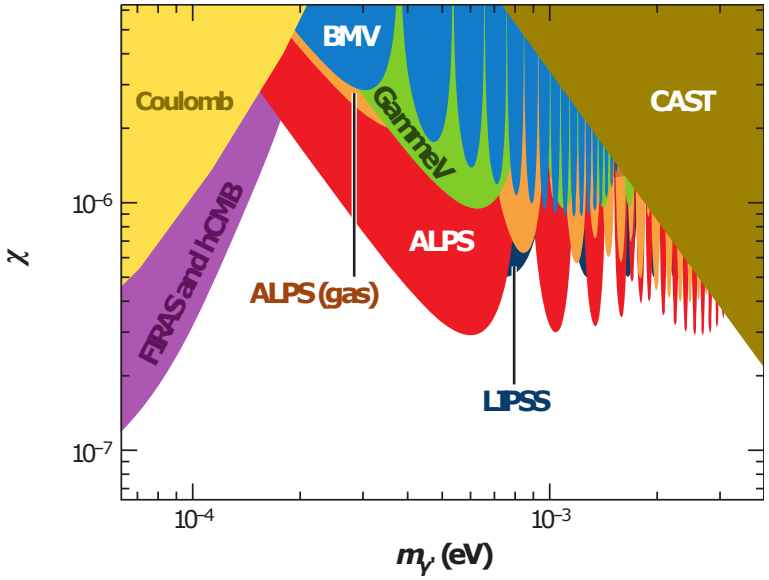

Figure 3.3: Experimental bounds on the photon-HP mixing parameter χ using the LSW method. Adapted from Ref. [17]

then reconverted to photons with the same probability as Eq. 3.3, and is caught by a photodetector.

This method was originally invented to search for axions by K. van Bibber and others [112], which requires strong magnetic fields before and after penetrating the wall to convert axions to photons and vice versa via the Primakov conversion. Hidden photon searches, which do not require the magnetic field, can be done simultaneously to axion searches.

Experiments employing the LSW method are carried out by several groups, such as BMV [113], GammeV [36], and ALPS [18], and they set upper limits on the photon-HP mixing parameter χ from the non-observation results as shown in Fig. 3.3. Equation (3.4) can be written as

$$P\left(\gamma \to \gamma'\right) \simeq 4\chi^2 \times \sin^2\left(1.27 \times \frac{\left(m_{\gamma'}^2/\mathrm{meV}\right)^2 \left(L/\mathrm{m}\right)}{\omega/\mathrm{eV}}\right),$$

from which we find that using light sources of $\sim$ eV energy and vacuum pipes of $\sim$m, LSW experiments are sensitive for hidden photons with mass around $\sim$ meV.

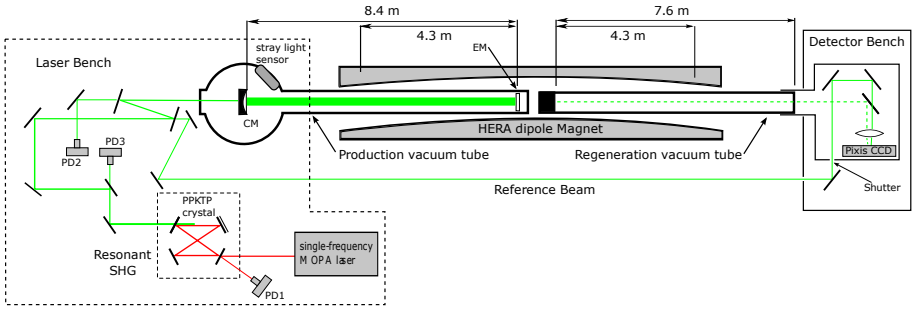

Figure 3.4: Schematic diagram of the experimental set-up of the ALPS experiment. Taken from Ref. [18].

ALPS

As an example of experiments employing the LSW method, we review the ALPS experiment [18] in DESY.

Figure 3.4 shows a schematic diagram of the experimental set-up of the ALPS experiment. The MOPA laser system [114] emits light of 1064 nm wavelength at an intensity of 35W. The laser light is introduced into a non-linear PPKTP (Periodically Poled $KTiOPO_4$) crystal to modify the wavelength to fit the reception frequency of the photodetector, then into a vacuum pipe. The Coupling Mirror (CM) and the End Mirror (EM) are installed in the vacuum pipe, and work as an optical resonator. Another vacuum pipe for regeneration of photons is equipped with a thick light absorber (the wall) between the pipes. A HERA superconducting dipole magnet surrounds the pipes to apply a magnetic field for axion searches. The CCD camera PIXIS 1024B is utilized as a photodetector, which has 1024×1024 pixels of $13\mu\text{m} \times 13\mu\text{m}$. The dark-count rate of the detector is $0.001\, e^-$/pixels/s, and the read-out noise is $3.8\, e^-$/pixels RMS. The camera operates at $-70°\text{C}$ and have the quantum efficiency of 96 % at 532 nm. A convex lens is installed in front of the camera, and the beam is focused to 30 μm, which exceeds the size of a pixel. In order to minimized the effect of the read-out noise, a 3×3 binning is employed and the exposure times is set to 1 hour.

The measurements were carried out varying

- ON/OFF of the magnetic field
- the polarization of the laser light parallel/perpendicular to the magnetic field
- vacuum / a small amount of argon gas in the tubes

The experimental result for hidden photon is obtained combining 23 frames without gas and 9 frames with gas, where they found no excess in the signal, and set an upper limit shown in Fig. 3.3 labeled "ALPS".

The ALPS experiment is planning for an update to the apparatus [19], where they expect a sensitivity for hidden photon as shown in Fig. 3.5. The magnetic length $468\,\text{T} \cdot \text{m}$ is achieved using $10 + 10$ HERA superconducting dipole magnets, and a transition edge sensor is employed for a photodetector, which allows for high detection efficiency in infrared region.

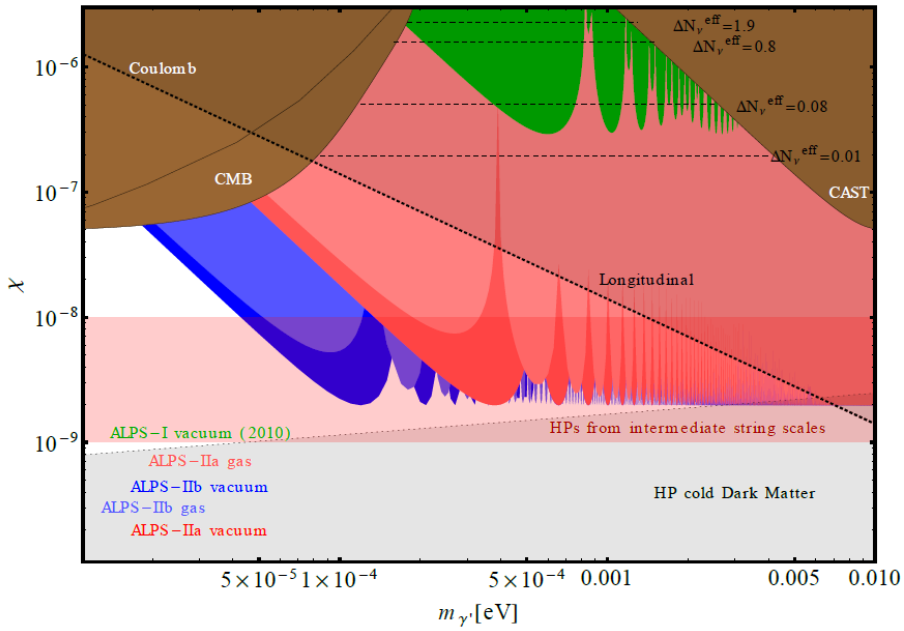

Figure 3.5: Expected sensitivity for the photon-HP mixing parameter χ reached by the updated apparatus of the ALPSII experiment. Taken from Ref [19].

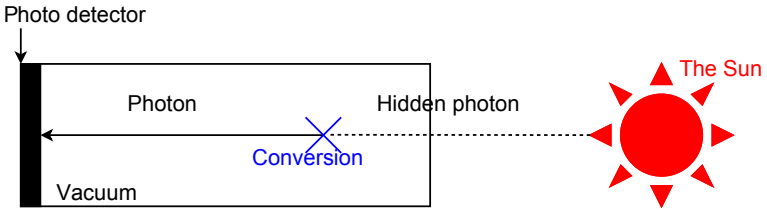

Figure 3.6: Schematic of a solar hidden photon search using a helioscope. Hidden photons from the Sun are converted to ordinary photons in a vacuum chamber with a probability Eq. 3.4, then caught by a photodetector. The vacuum chamber has to be mounted on an altazimuth mount to trace the movement of the Sun.

3.2.2 Solar hidden photon search

The Sun would be a strong emitter of hidden photons, and several experiments have searched for solar hidden photons using the method originally invented by Sikivie [93] to search for axions similarly produced in the Sun. Photons inside the Sun could oscillate into hidden photons, which do not interact with ordinary matter and leave the Sun without being interrupted. We thus have opportunity to observe those hidden photons coming to a laboratory and converted to ordinary photons with a probability Eq. 3.4 inside a vacuum chamber. Figure 3.6 depicts a schematic of a helioscope for solar hidden photon search. The vacuum chamber has to be mounted on an altazimuth mount to trace the movement of the Sun.

The calculation of the flux of hidden photons from the Sun was performed in Ref. [20] and the result is shown in Fig. 3.7. The figure plots spectra of hidden photons produced in the Sun for the mass of hidden photon $m_{\gamma'} = 10^{-3}$, 3.16×10^{-3}, 10^{-2}, 3.16×10^{-2}, 10^{-2}, 10^{-1}, 0.316 eV (bottom to up, the thresholds are out of the plot) and $m_{\gamma'} = 1$, 3.16, 10, 31.6, 100, 316, 10^3 eV (the thresholds are found inside the plot). Hidden photons with the mass around meV − eV are resonantly produced in

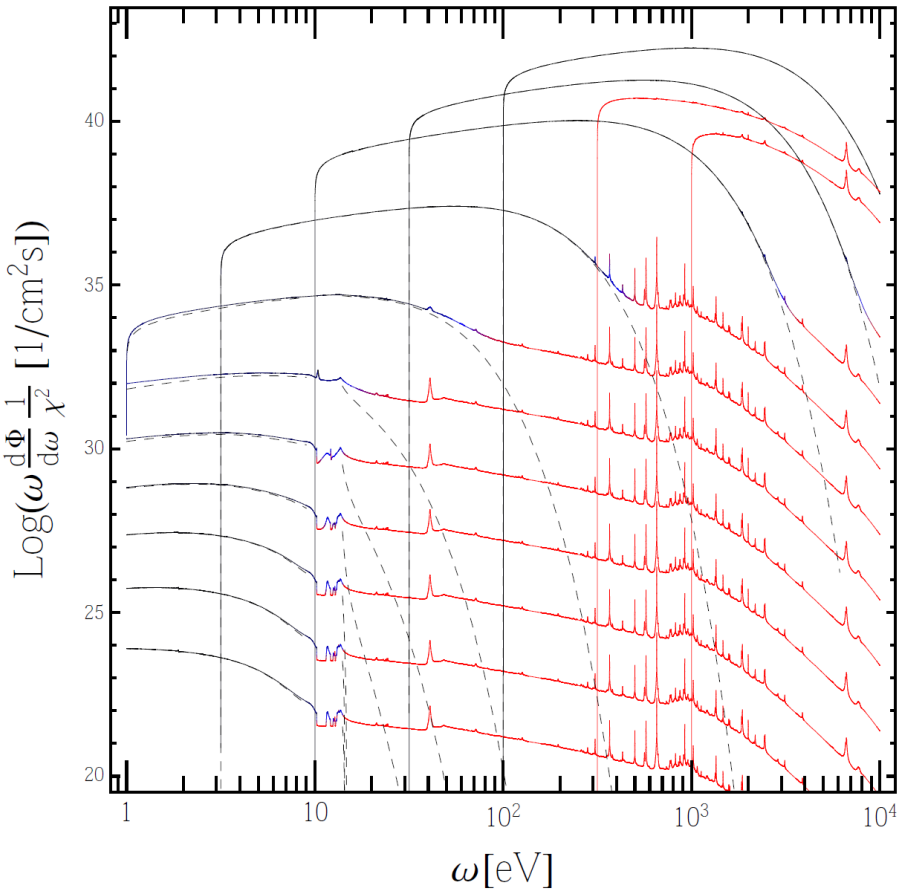

Figure 3.7: Spectra of hidden photons produced in the Sun for the mass of hidden photon $m_{\gamma'} = 10^{-3}$, 3.16×10^{-3}, 10^{-2}, 3.16×10^{-2}, 10^{-2}, 10^{-1}, 0.316 eV (bottom to up, the thresholds are outside the plot) and $m_{\gamma'} = 1$, 3.16, 10, 31.6, 100, 316, 10^3 eV (the thresholds are found inside the plot). Taken from Ref. [20].

a tiny shell close to the photosphere, where the effective mass of photons in the solar plasma corresponds to the mass of hidden photons.

The experimental reach of this method depends on parameters of the apparatus as

$$\begin{aligned} \chi \;<\; & 10^{-7} \times \left(\frac{m_{\gamma'}}{\mathrm{meV}}\right)^{-1} \left(\frac{\nu}{\mathrm{Hz}} \frac{100\,\mathrm{day}}{T}\right)^{1/8} \left(\frac{1000\,\mathrm{cm}^2}{A}\right)^{1/4} \\ & \times \left(\int \frac{d\omega}{\mathrm{eV}} \frac{FF\,\mathrm{eVcm}^2\mathrm{s}}{10^{35}} \eta_{\mathrm{mirror}} \left(\frac{\eta_{\mathrm{PMT}}}{0.1}\right) \left(\frac{P_{\gamma\to\gamma'}}{\chi^2}\right)\right)^{-1/4} \\ & (95\%\,\mathrm{CL}) \end{aligned}$$

where ν is the dark count rate of the detector, T the duration of the measurement, A the crosssection of the chamber, η_{mirror} the reflectivity of the mirror, η_{PMT} the efficiency of the photodetector, $P_{\gamma\to\gamma'}$ the probability of the $\gamma \to \gamma'$ conversion (cf. Eq. (3.4)), and

$$FF \equiv \frac{d\Phi}{d\omega} \frac{1}{\chi^2} \left(\frac{\mathrm{eV}}{m_{\gamma'}}\right)^4$$

for solar flux of hidden photons $d\Phi/d\omega$.

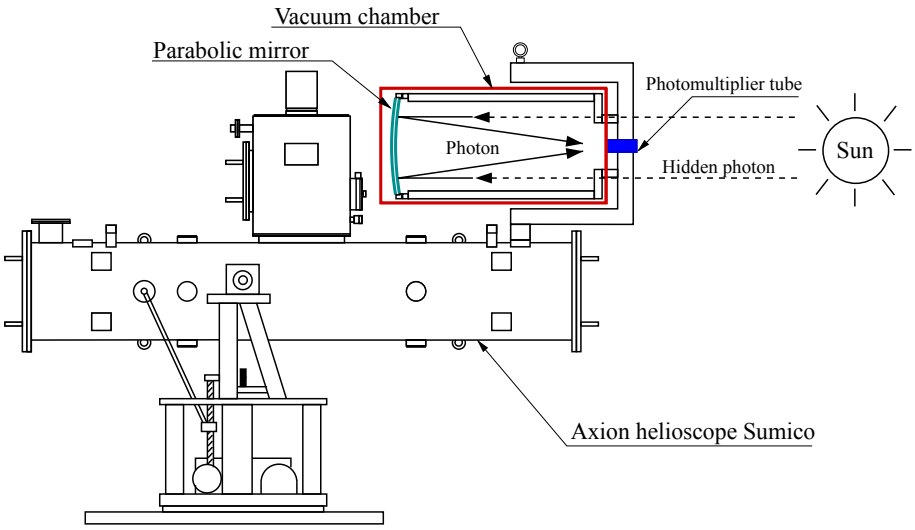

Figure 3.8: Schematic diagram of the experimental set-up of the solar hidden photons search described in Ref. [21, 22].

Sumico

The first dedicated search for solar hidden photons was carried out by the Sumico group [21, 22], where a vacuum chamber equipped with a large parabolic mirror was mounted on the axion helioscope Sumico described in Sec. 2.3.2. Figure 3.8 depicts a schematic of the experimental set-up. The employment of a parabolic mirror instead of a photodetector with a large effective area reduces the signal-to-noise ratio and leads to a sensitive search.

Hidden photons from the Sun oscillate into photons in a vacuum chamber of 570 mm diameter and 1.2 m long, and then are focused by a parabolic mirror to a photodetector. A photomultiplier tube, R3550P (Hamamatsu, Japan) was selected for the photodetector because of its low dark-count rate. The parabolic mirror is 500 mm in diameter, and has a focal length of 1007 mm. Figure 3.9 is a photograph of the apparatus mounted on the axion helioscope Sumico.

The tracking accuracy required to keep the image of the entire Sun inside the effective area of the photodetector is $\sim$ 5 mrad, and the axion helioscope on which the chamber was mounted can trace the Sun with an accuracy of 0.5 mrad. The axion helioscope Sumico is driven by a turntable for azimuth direction and a ball screw for altitude, both of which are powered by AC servo motors. The elevation and the azimuthal angle are monitored by rotary encoders (R-1L, Canon, Japan), and the feedback control system was constructed to achieve high tracking accuracy. The control system combines

- Obtaining values of the encoders (azimuth, altitude) via a dedicated CAMAC module [115]
- Sending pulses for the motors (azimuth, altitude) via a dedicated CAMAC module [116]
- Calculation of the position of the Sun using the U. S. Naval Observatory Vector Astronomy Subroutines (NOVAS) [117]

and works on the FreeBSD 2.2.8-RELEASE.

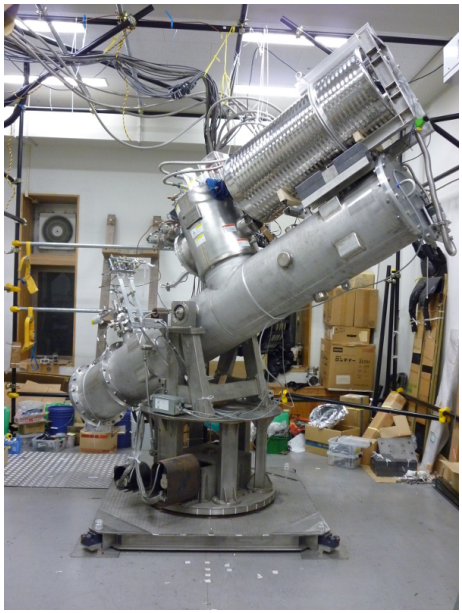

Figure 3.9: Photograph of the apparatus mounted on the axion helioscope Sumico.

The output of the photomultiplier is connected to a charge-sensitive amplifier (ORTEC 113) followed by a shaper (ORTEC 572), and a Wilkinson-type ADC (2201A, Laboratory Equipment Corp., Japan), which works in coordination with a dedicated multichannel analyzer (MCA/PC98, Laboratory Equipment Corp., Japan).

The experimental run was done from October 26, 2010 to November 16, 2010, and the data obtained during solar tracking and the background measurement were compared, where no significant excess was observed. The non-observation of the signal gives an upper limit on the photon-HP mixing parameter χ using the flux of hidden photons calculated in Fig. 3.7. The result is shown in Fig. 3.10.

SHIPS

A similar experiment was performed by the SHIPS group [23] at DESY. Figure 3.11 is a schematic diagram of the apparatus used by the SHIPS group, where they employed a Fresnel lens to collect generated photons to a photodetector instead of a parabolic mirror. The length of the vacuum tube is 4.3 m and the inner diameter is 26 cm. A photomultiplier tube (9893/350B, ET Enterprises, the United Kingdom) was employed for a photodetector, and cooled down to $-21°$C by a ET FACT 50 cooler housing (ET Enterprises).

The experimental run was done between March 18, 2013 and May 7, 2013, and the final data consist of 660 hours in total, where they found no excess of counts in solar tracking data. Figure 3.12 shows the experimental bound for the photon-HP mixing parameter χ obtained by the SHIPS experiment, which slightly surpass that of the experiment in Ref. [21] (labeled "Sumico" in Fig. 3.12).

XENON10

Recently, it was pointed out by An et al. [118] that experiments to detect WIMPs with low energy threshold also have sensitivity to hidden photons produced in the Sun. Having a non-zero mass $m_{\gamma'}$, hidden photons allow a longitudinal mode unlike

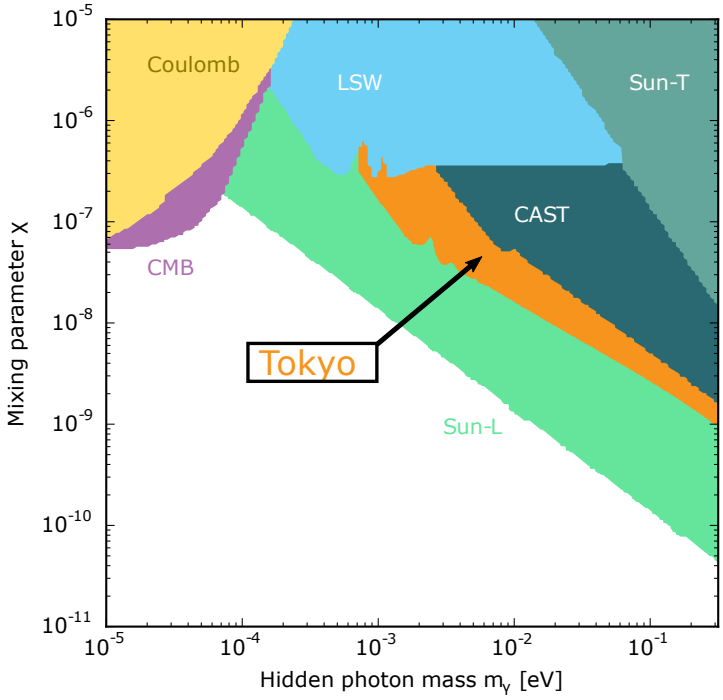

Figure 3.10: 95% confidence level upper limits to the mixing angle χ set by the non-observation of the excess ("Tokyo"). Other filled areas are excluded by experiments and theoretical studies on astronomical objects described at the beginning of this section.

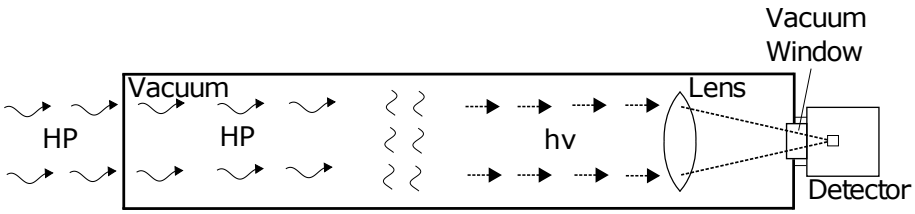

Figure 3.11: Schematic of the SHIPS apparatus and the detection process. Generated photons are collected by a Fresnel lens to a photodetector. Taken from Ref. [23].

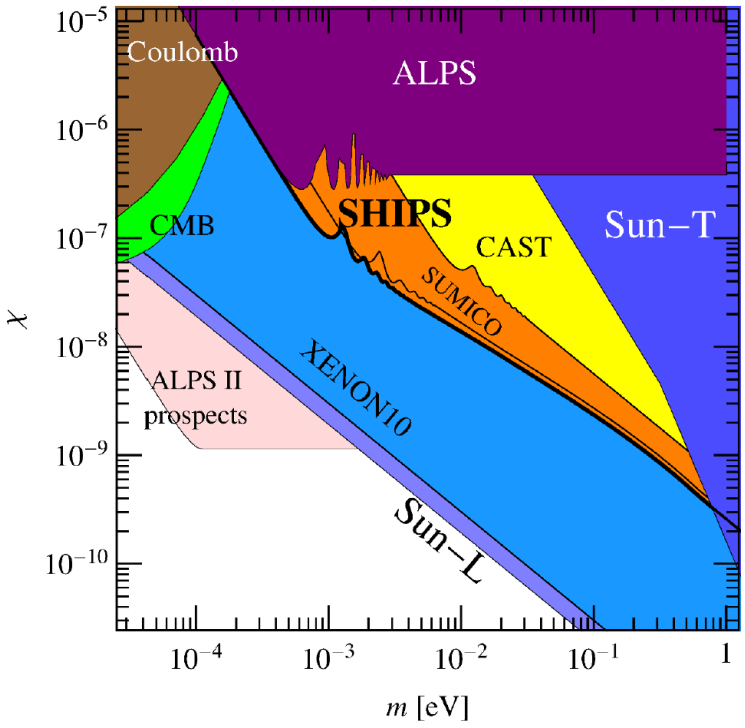

Figure 3.12: Experimental bound for the photon-HP mixing parameter χ obtained by the SHIPS experiment. Taken from Ref. [23].

ordinary photons, and the emission rate in the longitudinal mode is found to be several orders of magnitude greater than that in the transverse mode [40, 41]. Although those longitudinal excitations cannot be detected by the experiments described above, in which hidden photons are converted to photons in vacuum, dark matter detectors utilizing liquid noble gas or semiconductors, where hidden photons might induce atomic ionizations, have opportunity to detect them.

The amplitude for the absorption of hidden photons can be written as

$$\begin{aligned}\mathcal{M}_{i+\gamma'_{T,L}\to f} &= -\chi m_{\gamma'}^2 \langle A^\mu | A^\nu \rangle \langle f \,|[eJ_{\mathrm{EM}\mu}]|\, i\rangle \,\epsilon_\nu^{T,L} \\ &= -\frac{\chi m_{\gamma'}^2}{m_{\gamma'}^2 - \Pi_{T,L}} \langle f \,|[eJ_{\mathrm{EM}}^\mu]|\, i\rangle \,\epsilon_\mu^{T,L}\end{aligned}$$

because, to leading order in χ, $\partial_\mu X^\mu = 0$ yields

$$\mathcal{L}_{\mathrm{int}} = -\frac{\chi}{2} F_{\mu\nu} X^{\mu\nu} + eJ_{\mathrm{EM}}^\mu A_\mu \to -\chi m_{\gamma'}^2 A_\mu X^\mu + eJ_{\mathrm{EM}}^\mu A_\mu.$$

The propagation of the electromagnetic field inside a medium is determined by the polarization tensor

$$\Pi^{\mu\nu} = e^2 \left\langle J_{\mathrm{EM}}^{\mu\dagger},\, J_{\mathrm{EM}}^\nu \right\rangle = \Pi_T \sum_{i=1,2} \epsilon_i^{T\mu} \epsilon_i^{T\nu} + \Pi_L \epsilon^{L\mu} \epsilon^{L\nu}$$

The absorption rate can be written as[1]

$$\Gamma = \frac{\chi_{T,L}^2 e^2 \epsilon_\mu^{T,L*} \epsilon_\nu^{T,L}}{2\omega} \int d^4x e^{iq\cdot x} \left\langle i \left| J_{\mathrm{EM}}^{\mu\dagger}(x) J_{\mathrm{EM}}^\nu(0) \right| i \right\rangle = -\frac{\chi_{T,L}^2 \mathrm{Im}\Pi_{T,L}}{\omega},$$

[1]The last equality holds as a consequence of the optical theorem (the unitarity of S-matrix)

where q is the four-momentum of the hidden photon with $\omega = q^0$ and

$$\chi^2_{T,L} \equiv \frac{\chi^2 m^4_{\gamma'}}{\left(m^2_{\gamma'} - \mathrm{Re}\Pi_{T,L}\right)^2 + \left(\mathrm{Im}\Pi_{T,L}\right)^2}. \tag{3.5}$$

In an isotropic non-magnetic material, we have

$$\begin{aligned} \Pi_T &= -\omega^2 \Delta\varepsilon_r \\ \Pi_L &= -q^2 \Delta\varepsilon_r \end{aligned}$$

where $\Delta\varepsilon_r \equiv \varepsilon_r - 1$ for the relative perimittivity of the target material ε_r. We thus find the absorption rates to be

$$\begin{aligned} \Gamma_T &= \left(\frac{\chi^2 m^4_{\gamma'} \mathrm{Im}\varepsilon_r}{\omega^3 \left|\Delta\varepsilon_r\right|^2}\right)\left[1 + \frac{2m^2_{\gamma'}\omega^2 \mathrm{Re}\Delta\varepsilon_r + m^2_{\gamma'}}{\omega^4 \left|\Delta\varepsilon_r\right|^2}\right]^{-1}, \\ \Gamma_L &= \frac{\chi^2 m^2_{\gamma'} \mathrm{Im}\varepsilon_r}{\omega \left|\varepsilon_r\right|^2}. \end{aligned}$$

Since $\mathrm{Re}\Delta\varepsilon_r$ and $\mathrm{Im}\varepsilon_r$ are proportional to the number density of atoms of the material n_A, we find that

$$\begin{aligned} \Gamma_T &\propto n_A^{-1}, \\ \Gamma_L &\propto n_A, \end{aligned}$$

which suggests that low density material is suited for T-mode detection, while high density is required to detect L-mode hidden photons.

From the absorption rate derived above and the flux of hidden photons from the Sun [40], we can compute the event rate inside the detector's material as

$$N_{\mathrm{exp}} = VT \int_{\omega_{\mathrm{min}}}^{\omega_{\mathrm{max}}} \frac{\omega d\omega}{|\vec{q}|}\left(\frac{d\Phi_T}{d\omega}\Gamma_T + \frac{d\Phi_L}{d\omega}\Gamma_L\right)\mathrm{Br},$$

where V is the fiducial volume of the detector, T the exposure time, and Br the branching ratio (photoionization rate)/(total absorption rate). In Ref. [118], a conservative upper limit for the photon-HP mixing parameter χ was calculated using a study on low-energy ionization events by the XENON10 Collaboration [108], and the result is shown in Fig. 3.12 (labelled "XENON10"), which by far exceeds the bounds from the searches employing vacuum chambers.

3.3 Hidden photon dark matter

In Chapter 2, we saw a lot of evidence for the existence of non-baryonic matter which occupies about 27 % of the total energy density of the universe. Despite concrete evidence for the existence, dark matter has not been directly detected, and its nature is still unknown.

WIMPs are assumed to be the most feasible candidates because the abundance is naturally derived in thermal production as we explained in Sec. 2.2.1. We also show that axions with their mass $\sim \mu$eV might be the main component of dark matter via the misalignment mechanism.

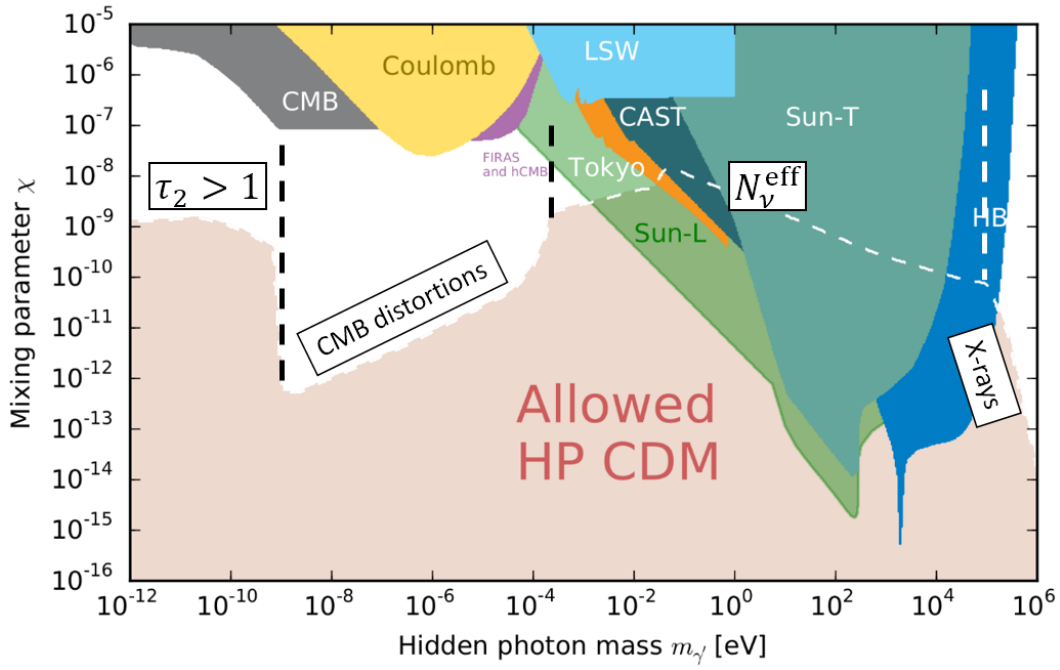

Figure 3.13: Plot of the parameter space allowed for dark matter (colored pink).

Recently, it was pointed out by several authors [24, 25] that hidden photons can account for dark matter. Figure 3.13 plots the parameter space allowed for dark matter in the $\chi - m_{\gamma'}$ plane of the hidden photon model. The mass $m_{\gamma'}$ for the allowed region is quite smaller than that of WIMPs ($m_\chi \sim$ GeV $-$ TeV), and it cannot be thermally produced. Instead, the hidden photon DM scenario postulates that the hidden-photon field has a non-zero field value at the early era of the universe, and it remains until today to work as non-baryonic mass. It is similar to the axion DM scenario, and the difference is that the field is a vector field instead of a scalar field and there is no preferable scale for the initial value of the field for the hidden photon DM.

The rest of this chapter is devoted to the explanation of the mechanism, constraints from cosmology.

3.3.1 Misalignment mechanism

The mechanism to generate a population of hidden photons is quite similar to the axion case, which we described in Sec. 2.2.2. A slight difference comes from its vector nature of the field [119].

The action of the hidden photon field we are concerned here is

$$S = \int \mathrm{d}x^4 \sqrt{-g} \left(-\frac{R}{16\pi G} - \frac{1}{4} X_{\mu\nu} X^{\mu\nu} + \frac{m_{\gamma'}^2}{2} X_\mu X^\mu + \frac{\kappa}{12} R X_\mu X^\mu + \mathcal{L}_I \right),$$

where $\mathcal{L}_I$ represents the interactions with the Standard Model particles, R the Ricci scalar, and we have included a non-minimal coupling to gravity $(\kappa/12) R X_\mu X^\mu$. The equation of motion is obtained by varying the action with respect to X_μ as

$$\frac{1}{\sqrt{-g}} \frac{\partial}{\partial x^\mu} \left(\sqrt{-g} X^{\mu\nu} \right) + \left(m_{\gamma'}^2 + \frac{\kappa R}{6} \right) X^\nu = 0.$$

Supposing the spatially flat Friedmann universe

$$\mathrm{d}s^2 = \mathrm{d}t^2 - a^2(t)\delta_{ik}\mathrm{d}x^i\mathrm{d}x^k,$$

the equation of motion is written as

$$-\frac{1}{a^2}\partial_i\partial_i X_0 + \left(m_{\gamma'}^2 + \frac{\kappa R}{6}\right)X_0 + \frac{1}{a^2}\partial_i\dot{X}_i = 0,$$

$$\ddot{X}_i + \frac{\dot{a}}{a}\dot{X}_i - \frac{1}{a^2}\Delta X_i + \left(m_{\gamma'}^2 + \frac{\kappa R}{6}\right)X_i - \partial_i\dot{A}_0 - \frac{\dot{a}}{a}\partial_i A_0 + \frac{1}{a^2}\partial_i\left(\partial_k A_k\right) = 0.$$

The strength of the vector field is characterized by a quantity

$$I = X^\mu X_\mu = X_0^2 - \frac{1}{a^2}X_i X_i,$$

and thus it is convenient to use

$$\bar{X}_i = \frac{X_i}{a},$$

instead of X_i.

For simplicity, let us consider the quasi-homogeneous vector field ($\partial_i X_\mu = 0$). Under this assumption, the equation of motion is

$$X_0 = 0,$$

$$\ddot{X}_i + \frac{\dot{a}}{a}\dot{X}_i + \left(m_{\gamma'}^2 + \frac{\kappa R}{6}\right)X_i = 0.$$

Substituting $X_i \equiv a\bar{X}_i$ and

$$R = -6\left[\frac{\ddot{a}}{a} + \left(\frac{\dot{a}}{a}\right)^2\right],$$

we obtain

$$\ddot{\bar{X}}_i + 3H\dot{\bar{X}}_i + \left(m_{\gamma'}^2 + (1-\kappa)\left(\dot{H} + 2H^2\right)\right)\bar{X}_i = 0. \tag{3.6}$$

We thus find that for $H \ll m_{\gamma'}$ and $\dot{H} \ll m_{\gamma'}^2$, the above equation reduces to the same form as (2.6) for any κ value. As a result, the same approximate formulae Eqs. (2.7) and (2.8) hold for the field $\bar{X}_i$, and, in particular, the energy density dilutes as non-relativistic matter $\rho \sim a^{-3}$ for $m_{\gamma'} = \mathrm{cosnt}$. For $\kappa = 1$, (3.6) coincides with (2.6) and the arguments for $H \gg m_{\gamma'}$ still hold, i.e. both $\bar{X}_i$ and the energy density are constant and frozen to their initial values.

3.3.2 Evaporation of the condensate in the primordial plasma

The population of the hidden-photon field produced via the misalignment would not simply be preserved because of its interaction with Standard Model particles via its kinetic mixing with photons $(-\chi/2)F_{\mu\nu}X^{\mu\nu}$. The field strength and the energy density of the field would evaporate into ordinary photons and degrade along the history of the universe. Although we can suppose high enough initial value for the field X^μ to explain the energy density of dark matter today $\Omega_{\mathrm{M}} \simeq 0.3$, the evaporation results in injection

of photons to thermal bath, which might induce contradiction to observations such as the CMB radiation spectrum. The injection might occur resonantly in the primordial plasma [25], where the medium effects play an important role as the Mikheev-Smirnov-Wolfenstein (MSW) effect.

The interaction between hidden photons and ordinary photons is described by the Lagrangian

$$\mathcal{L} = -\frac{1}{4}F_{\mu\nu}F^{\mu\nu} - \frac{1}{4}X_{\mu\nu}X^{\mu\nu} + \frac{m_{\gamma'}^2}{2}X_\mu X^\mu - \frac{\chi}{2}F_{\mu\nu}X^{\mu\nu} + J^\mu A_\mu,$$

where J^μ is the current of standard model particles with ordinary electric charge. By the change of basis

$$\{A,\, X\} \longrightarrow \left\{\tilde{A} = A + \chi X,\, \tilde{X} = X\right\},$$

the Lagrangian is written as

$$\mathcal{L} = -\frac{1}{4}\tilde{F}_{\mu\nu}\tilde{F}^{\mu\nu} - \frac{1}{4}\tilde{X}_{\mu\nu}\tilde{X}^{\mu\nu} + \frac{m_{\gamma'}^2}{2}\tilde{X}_\mu\tilde{X}^\mu + J^\mu\left(\tilde{A}_\mu - \chi\tilde{X}_\mu\right),$$

from which we can identify the basis $\{\tilde{A},\, \tilde{X}\}$ as the propagation basis in vacuum. In addition, the change of basis

$$\{A,\, X\} \longrightarrow \{A,\, S = X + \chi A\}$$

yields

$$\mathcal{L} = -\frac{1}{4}F_{\mu\nu}F^{\mu\nu} - \frac{1}{4}S_{\mu\nu}S^{\mu\nu} + \frac{m_{\gamma'}^2}{2}\left(S_\mu - \chi A_\mu\right)\left(S^\mu - \chi A^\mu\right) + J^\mu A_\mu. \tag{3.7}$$

We thus find that $\{A,\, S\}$ is the interaction eigenstate.

In the primordial plasma, photons acquire an effective mass

$$M^2 \equiv m_\gamma^2 + i\omega\Gamma,$$

where m_γ is the plasma mass and Γ the interaction rate, and the effect appends a term $M^2 A_\mu A^\mu/2$ to the Lagrangian described above, which modifies the propagation eigenstates from $\{\tilde{A},\, \tilde{X}\}$.

At the early stage of the history of the universe, M^2 acquires extremely large value because it is proportional to the charge density η_Q. Therefore, $A = \tilde{A} - \chi\tilde{X}$ can be approximately assumed as the propagation eigenstate, and the orthogonal combination $\tilde{X} + \chi\tilde{A} (= S)$ would be its counterpart, forming a condensate described in the previous section.

Expansion of the universe cools the plasma and M^2 tends to 0 today, so $\tilde{A}$ and $\tilde{X}$ are the propagation eigenstate. We thus conclude that the condensate is deformed from $\tilde{X} + \chi\tilde{A}$ to $\tilde{X}$ in the evolution of the universe. The trajectory is characterized by an effective mixing angle (cf. Eq. 3.5)

$$\chi_{\rm eff}^2 \simeq \frac{\chi^2 m_{\gamma'}^4}{\left(m_\gamma^2 - m_{\gamma'}^2\right)^2 + \mu^4}, \tag{3.8}$$

where $\mu^2 = \max\{\chi m_{\gamma'}^2, m_{\gamma'}\Gamma\}$, which measures the angle between the sterile state $S = \tilde{X} + \chi\tilde{A}$ and the condensate. The eigenstates decay with rates[2]

$$\begin{aligned}\Gamma_1 &= \left(1 - \chi_{\rm eff}^2\right)\Gamma, \\ \Gamma_2 &= \chi_{\rm eff}^2\Gamma.\end{aligned}$$

From (3.8), we can roughly observe the behavior of the condensate:

- $m_\gamma \gg m_{\gamma'}$: At high temperature
  The mixing is strongly suppressed $\chi_{\rm eff} \simeq 0$. The condensate is $\tilde{X} + \chi\tilde{A}$.

- $m_\gamma \sim m_{\gamma'}$: At resonance
  The mixing is significantly enhanced $\chi \sim \chi(m_{\gamma'}^2/\mu^2)$ and overshoots χ.

- $m_\gamma \ll m_{\gamma'}$: At low temperature
  The effective mixing angle $\chi_{\rm eff}$ approaches to χ as the charge density decreases, and the condensate moves to $\tilde{X}$.

The behaviour of the condensate is complicated due to the existence of the resonance at $m_\gamma \sim m_{\gamma'}$. The condensate overshoots $\tilde{X}$ during the resonance, then returns to $\tilde{X}$, rather than moving smoothly from $\tilde{X} + \chi\tilde{A}$ toward $\tilde{X}$. At the resonance, the decay $\Gamma_2 = \chi_{\rm eff}^2\Gamma$ is maximized.

The amplitude of the condensate decreases as

$$\begin{aligned}\frac{X_{2,\,\rm today}}{X_{2,\,\rm initial}} &= \left(\frac{a_{\rm initial}}{a_{\rm today}}\right)^{3/2} \exp\left(-\frac{1}{2}\int_{t_{\rm initial}}^{t_{\rm today}} dt\Gamma_2\right) \\ &= \left(\frac{a_{\rm initial}}{a_{\rm today}}\right)^{3/2} \exp\left(-\frac{1}{2}\int_{T_{\rm today}}^{T_{\rm initial}} d\log T\frac{\Gamma_2}{H}\right),\end{aligned} \tag{3.9}$$

where the approximation $T/T_0 = a_0/a$ has been used in the second line. Figure 3.14 plots the function $\Gamma_2/H\chi^2 = \Gamma\chi_{\rm eff}^2/H\chi^2$ for several HP masses $m_{\gamma'} = 10^{-5}$ to 10^{-1} eV assuming over-damped oscillations during the resonance, i.e. $m_{\gamma'}\Gamma \gg \chi m_{\gamma'}^2$. The plot shows that the decay rate Γ_2 is greatly enhanced at the resonance, and it is legitimate to approximate the integral by the contribution near the resonance.

Using the expansion

$$m_\gamma^2 = m_{\gamma'}^2 + \left|\frac{dm_\gamma^2}{dT}\right|_{\rm res}(T - T_{\rm res})$$

where we suppose the resonance occurs at $T = T_{\rm res}(m_{\gamma'})$, the integral inside the expo-

[2]From now we label the eigenstates as $\{\gamma_1, \gamma_2\}$ where 1 is for the photon-like state and 2 for the HP-like state.

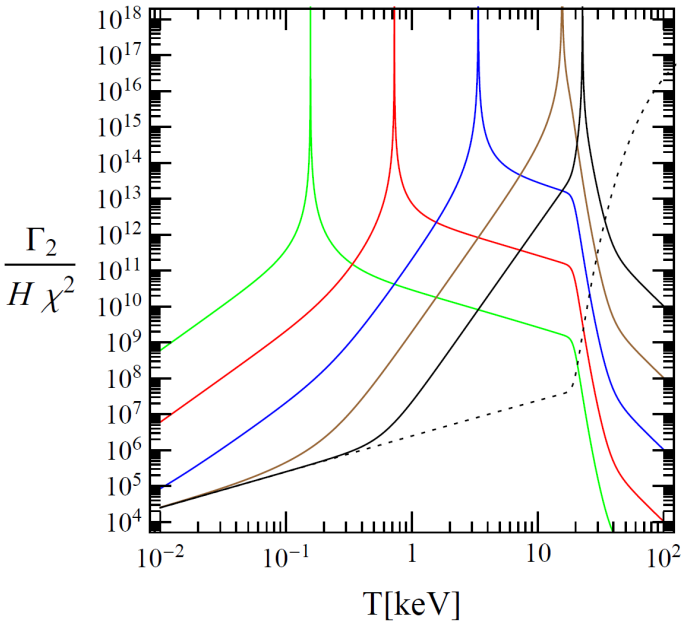

Figure 3.14: Plot of $\Gamma_2/H\chi^2 = \Gamma\chi^2_{\rm eff}/H\chi^2$ as a function of temperature for several HP masses. The curves shows the function for $m_{\gamma'} = 10^{-5}\,\mathrm{eV}$ (green), $m_{\gamma'} = 10^{-4}\,\mathrm{eV}$ (red), $m_{\gamma'} = 10^{-3}\,\mathrm{eV}$ (blue), $m_{\gamma'} = 10^{-2}\,\mathrm{eV}$ (red), $m_{\gamma'} = 10^{-1}\,\mathrm{eV}$ (black). The dashed line shows the assumption used in Ref. [24], where the effect of medium is not properly taken into account. Taken from Ref. [25].

nential of (3.9) is approximated as[3]

$$\begin{aligned}
\int_{T_{\rm today}}^{T_{\rm initial}} \frac{dT}{T}\frac{\Gamma_2}{H} &\simeq \frac{\chi^2 m_{\gamma'}^4 \Gamma_{\rm res}}{T_{\rm res} H_{\rm res}} \int_{T_{\rm today}}^{T_{\rm initial}} \frac{dT}{\left|dm_\gamma^2/dT\right|^2_{\rm res}\left(T-T_{\rm res}\right)^2 + \left(m_{\gamma'}\Gamma\right)^2} \\
&\simeq \frac{\chi^2 m_{\gamma'}^4 \Gamma_{\rm res}}{T_{\rm res} H_{\rm res}} \frac{1}{\left|dm_\gamma^2/dT\right|^2_{\rm res}} \int_{-\infty}^{+\infty} \frac{dT}{\left(T-T_{\rm res}\right)^2 + \left(m_{\gamma'}\Gamma/\left|dm_\gamma^2/dT\right|_{\rm res}\right)^2} \\
&= \frac{\chi^2 m_{\gamma'}^4 \Gamma_{\rm res}}{T_{\rm res} H_{\rm res}} \frac{1}{\left|dm_\gamma^2/dT\right|^2_{\rm res}} \times \pi \times \frac{\left|dm_\gamma^2/dT\right|_{\rm res}}{m_{\gamma'}\Gamma_{\rm res}} \\
&= \chi^2 \pi \frac{m_{\gamma'}}{r H_{\rm res}} \equiv \tau_2,
\end{aligned} \tag{3.10}$$

where $r = d\log m_\gamma^2/d\log T$ is an $\mathcal{O}(1)$ factor (plotted in Fig. 3.15).

Combining Eqs. (3.9) and (3.10), we find the amplitude decreases as $e^{-\tau_2/2}$ and the total energy density $e^{-\tau_2}$. Therefore, the energy dumped into the photon bath is described as

$$\Delta\rho = \rho_{\rm CDM}\left(e^{\tau_2} - 1\right).$$

As a result, several limitations from observational facts can be deduced.

[3]We supposed $m_{\gamma'}\Gamma \gg \chi m_{\gamma'}^2$ here. If $m_{\gamma'}\Gamma < \chi m_{\gamma'}^2$, the probability for the HP survival can be obtained using Landau-Zener expression [39]

$$p \simeq \exp\left(-2\pi \frac{\chi^2}{\left|d\log m_\gamma^2/dt\right|}\frac{m_{\gamma'}}{2}\right) = \exp\left(-\frac{1}{2}\cdot 2\tau_2\right),$$

resulting in an extra factor of 2.

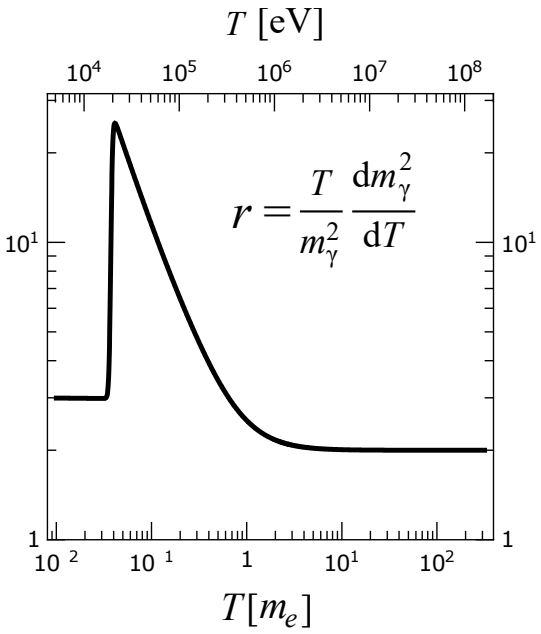

Figure 3.15: Plot of the function $r = d\log m_\gamma^2/d\log T$ as a function of temperature (see the upper horizontal axis). Adapted from Fig. 2 of Ref. [26].

Effective number of relativistic neutrino species $N_\nu^{\rm eff}$

The photon injection increases the abundance of photons relative to neutrinos at CMB decoupling. The ratio can be constrained by the effective number of relativistic neutrino species $N_\nu^{\rm eff}$. The photon injection enhances the photon temperature to

$$T' = \left(T_{\rm res} + \frac{15}{\pi^2}\Delta\rho\right)^{1/4} \sim T_{\rm res}\left(1 + 1.85\frac{m_p}{T_{\rm res}}\eta_B\left(e^{\tau_2} - 1\right)\right),$$

where $\rho_{\rm CDM} \sim 5 m_p \eta_B n_\gamma$ was used, with m_p the proton mass and the n_γ the photon number density. T' is constrained by $N_\nu^{\rm eff} < 2.39$ (at 95% CL) [120] to $T'/T < 1.06$, and combining this restriction with the above equation yields the constraint to the photon-HP mixing parameter χ labelled "$N_\nu^{\rm eff}$" in Fig. 3.13.

Distortion in the CMB spectrum

The photon injection below a low enough temperature might cause a distortion in the spectrum of the cosmic microwave background radiation because interactions of photons injected at very low energy with the relic electron and ions would not be sufficient to fully recover a blackbody spectrum. The constraint labelled "CMB" in Fig. 3.13 comes from the non-existence of this distortion, considering μ and y distortion of the CMB spectrum from the FIRAS analysis [121], and the analytic studies in Ref. [122].

CMB anisotropy

As explained in Sec. 2.1.3, the density of dark matter in the universe is estimated from the anisotropy of the CMB radiation, which agrees with estimations from other

sources. We thus conclude that the decrease of the density of the condensate is restricted after late recombination. Requiring $\tau_2 \lesssim 1$ for a mass range where $T_{\rm res}$ is after recombination, we can set a constraint labeled "$\tau_2 > 1$" in Fig. 3.13.

Hidden photon decay in X-rays

The decay rate of hidden photons via an electron loop into three photons is given by [26]

$$\Gamma_{3\gamma} \propto \alpha^4 \frac{m_{\gamma'}^9}{m_e^8},$$

which would be significant for massive hidden photons. Assuming that expected increase in the number of observed X-rays does not surpass the diffuse X-ray backgrounds, the constraint labeled "X-ray" in the rightmost of Fig. 3.13 is obtained.

Chapter 4

Experimental methods to search for hidden photon CDM

In Chapter 2, we described a lot of evidence for the existence of dark matter, and experimental efforts to directly detect DM particles were reviewed, where WIMPs or axions are assumed for the main component of dark matter. On the other hand, hidden photons are another candidate for dark matter as explained in the previous chapter.

In Chapter 3, we reviewed several experimental methods to search for hidden photons, including the LSW method, where hidden photons are produced in a laboratory with a high-intensity light source, and helioscope searches to detect hidden photons created in the Sun. In addition, if we suppose that hidden photons are the main component of dark matter, we can use dark matter with the local density $\rho_{\rm CDM} \simeq 0.4\,{\rm GeV/cm^3}$ (cf. Eq. 2.1) as a source of hidden photons.

The kinetic mixing of hidden photons with ordinary photons

$$-\frac{\chi}{2}F_{\mu\nu}X^{\mu\nu}$$

induces electromagnetic fields, via which experimental searches for hidden photon CDM can be performed. However, the photon-HP mixing parameter χ is assumed to be very small, and a method for an amplification of the signal is required to attain practical sensitivity.

One of those methods to amplify the signal is the 'dish' method introduced by Horns et al. in Ref. [123], where DM hidden photon induces emission of ordinary photons perpendicular to the surface of a spherical dish, resulting in concentration of the signal toward the curvature center. We utilized this method with an optical concave mirror to search for hidden photons in the eV mass range. We describe the method in detail in Sec. 4.1.

Other methods are reviewed in Sec. 4.2. Use of a cavity like the ADMX experiment (cf. Sec. 2.3.2) is also effective for hidden photon CDM search, and the results of past cavity experiments can be used to constrain the parameter space of hidden photon. Another method is to construct a 'radio' [30] for hidden photon in analogy to an ordinary radio which receives RF electromagnetic waves. In addition, WIMP detectors are sensitive for most massive hidden photons $m_{\gamma'} = 10 - 10^5\,{\rm eV}$ [111].

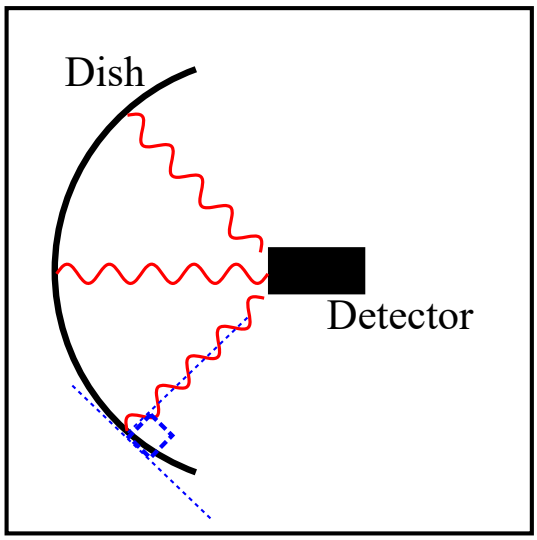

Figure 4.1: Schematic of the dish method for the experimental search of hidden photon CDM.

4.1 Dish method

Figure 4.1 depicts a schematic diagram of the dish method for the experimental search of hidden photon CDM. The set-up consists of a spherical dish with good reflectivity in the energy range of interest, and a detector which is placed at the curvature center of the dish sphere. Hidden photon fields induce emission of photons perpendicular to the surface of the dish with a frequency ω corresponding to the mass of hidden photon $\omega \simeq m_{\gamma'}$. Because of the shape of the dish, these emissions concentrate to the center of the sphere, where the detector receives them. This mechanism works as an amplification of the signal in proportion to the area of the dish.

The rest of this section is devoted for detailed descriptions of the 'dish' method, including the reason for a perpendicular emission and arguments for the directional sensitivity, and a review on a past experiment employing the method performed by Horie et al. [27, 28, 29].

4.1.1 Principle

Using the interaction eigenstates $\{A^\mu, S^\mu\}$, the Lagrangian of photons and hidden photons is (cf. Eq. 3.7)

$$\mathcal{L} = -\frac{1}{4}F_{\mu\nu}F^{\mu\nu} - \frac{1}{4}S_{\mu\nu}S^{\mu\nu} + \frac{m_{\gamma'}^2}{2}\left(S_\mu S^\mu - 2\chi A_\mu S^\mu + \chi^2 A_\mu A^\mu\right) + J^\mu A_\mu.$$

The equation of motion is then

$$\left[\left(\omega^2 - \mathbf{k}^2\right)\begin{pmatrix}1 & 0\\ 0 & 1\end{pmatrix} - m_{\gamma'}^2\begin{pmatrix}\chi^2 & -\chi\\ -\chi & 1\end{pmatrix}\right]\begin{pmatrix}\mathbf{A}\\ \mathbf{S}\end{pmatrix} = \begin{pmatrix}0\\ 0\end{pmatrix},$$

where $X^0 = A^0 = 0$ is assumed by a suitable gauge choice. To have a non-trivial solution, the determinant of the matrix must vanish:

$$\begin{aligned}\Delta &\simeq \left(\omega^2 - \mathbf{k}^2\right)\left(\omega^2 - \mathbf{k}^2 - m_{\gamma'}^2\right) = 0\\ \Longleftrightarrow \omega^2 - \mathbf{k}^2 &= 0,\, m_{\gamma'}^2,\end{aligned}$$

where the first solution corresponds to ordinary photons:

$$\begin{pmatrix}\mathbf{A}\\ \mathbf{S}\end{pmatrix} = \mathbf{E}\exp\left(-i\left(\omega t - \mathbf{k}\cdot\mathbf{x}\right)\right)\begin{pmatrix}1\\ \chi\end{pmatrix}, \tag{4.1}$$

and the second expresses massive states:

$$\begin{pmatrix}\mathbf{A}\\ \mathbf{S}\end{pmatrix} = \mathbf{E}\exp\left(-i\left(\omega t - \mathbf{k}\cdot\mathbf{x}\right)\right)\begin{pmatrix}-\chi\\ 1\end{pmatrix}. \tag{4.2}$$

For a while, we neglect the tiny velocity of local dark matter $v \sim 10^{-3}c$ and consider a spatially constant $\mathbf{k} = 0$ hidden photon field:

$$\left.\begin{pmatrix}\mathbf{A}\\ \mathbf{S}\end{pmatrix}\right|_{\rm DM} = \mathbf{X}_{\rm DM}\exp\left(-i\omega t\right)\begin{pmatrix}-\chi\\ 1\end{pmatrix}, \tag{4.3}$$

where $\omega = m_{\gamma'}$. If hidden photons dominate the population of dark matter, the DM field of hidden photons corresponds to the energy density of dark matter:

$$\rho_{\rm HP} = \frac{m_{\gamma'}^2}{2}\langle|\mathbf{X}_{\rm DM}|^2\rangle = \rho_{\rm CDM,\,halo} \sim 0.4\,{\rm GeV/cm^3}, \tag{4.4}$$

where we take an average $\langle|\mathbf{X}_{\rm DM}|^2\rangle$ assuming that DM is composed of a mixture of hidden photons with random directions[1].

Eq. 4.3 suggests that a small fraction of the energy density is in the form of an ordinary electric field as a consequence of the existence of the kinetic mixing:

$$\mathbf{E}_{\rm DM} = -\partial_0\mathbf{A} = \chi m_{\gamma'}\mathbf{X}_{\rm DM}. \tag{4.5}$$

Combining (4.4) and (4.5), we acquire the amplitude of the electric field[2]

$$\sqrt{\langle|\mathbf{E}_{\rm DM}|^2\rangle} = \chi\sqrt{2\rho_{\rm CDM,\,halo}} \sim 3.3\times10^{-9}\frac{\rm V}{\rm m}\left(\frac{\chi}{10^{-12}}\right)\left(\frac{\rho_{\rm CDM,\,halo}}{0.3\,{\rm GeV/cm^3}}\right)^{1/2},$$

with a frequency

$$f = \frac{m_{\gamma'}}{2\pi} = 0.24\,{\rm GHz}\left(\frac{m_{\gamma'}}{\mu{\rm eV}}\right).$$

We introduce hidden electric fields as $\mathbf{E}_{\rm hid} = -\partial_0\mathbf{S}$ so that we can write the propagation of the fields as

$$\left.\begin{pmatrix}\mathbf{E}\\ \mathbf{E}_{\rm hid}\end{pmatrix}\right|_{\rm DM} = -m_{\gamma'}\mathbf{X}_{\rm DM}\exp\left(-i\omega t\right)\begin{pmatrix}-\chi\\ 1\end{pmatrix} = -\frac{1}{\chi}\mathbf{E}_{\rm DM}\exp\left(-i\omega t\right)\begin{pmatrix}-\chi\\ 1\end{pmatrix}.$$

Suppose that a plane reflector with perfect reflectivity is placed in the ambient DM field. At the surface of the reflector, the component of the electric field parallel to the

[1] On the other hand, the direction of $\mathbf{X}_{\rm DM}$ might be preserved in the structure formation, and pointing the same direction everywhere. In this case, the intensity of the emission of photons induced by hidden photons varies on a daily basis because of the rotation of the earth, which might be used as a strong evidence of the signal of hidden photon CDM.

[2] We use $0.3\,{\rm GeV/cm^3}$ rather than $0.4\,{\rm GeV/cm^3}$ for the normalization of $\rho_{\rm CDM}$ in order to preserve original values appearing in Ref. [25, 123].

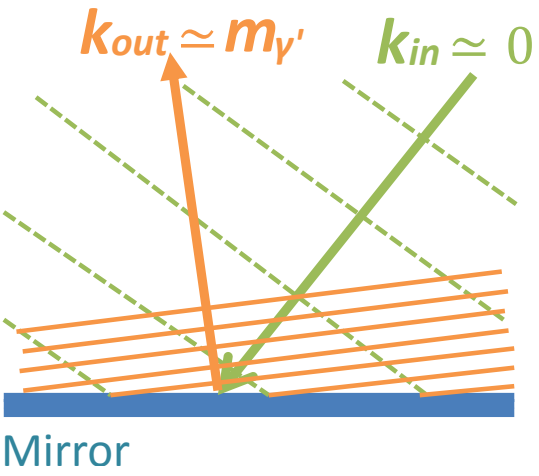

Figure 4.2: Schematic of the mechanism of perpendicular emission. The vectors and wavefronts of the incoming hidden photon field (light green) and the induced emission (orange) are depicted.

reflector $\mathbf{E}_{||}$ must vanish to meet the boundary condition. We thus find that it induces the emission of electromagnetic waves as in the following equation:

$$\begin{aligned}\begin{pmatrix}\mathbf{E}\\ \mathbf{E}_{\rm hid}\end{pmatrix}\Big|_{\rm total,\,||} &= \mathbf{E}_{\rm DM,\,||}\left[\begin{pmatrix}1\\ \chi\end{pmatrix}\exp\left(-i\left(\omega t-\mathbf{k}\cdot\mathbf{x}\right)\right)+\frac{1}{\chi}\begin{pmatrix}-\chi\\ 1\end{pmatrix}\exp\left(-i\omega t\right)\right]\\ &\xrightarrow{x=0} \mathbf{E}_{\rm DM,\,||}\frac{1}{\chi}\begin{pmatrix}0\\ 1\end{pmatrix},\end{aligned}$$

where we assumed that the reflector is placed on the $x = 0$ plane. To fulfill the boundary condition everywhere on the $x = 0$ plane, the wave vector $\mathbf{k}$ is required to be

$$\mathbf{k} = \omega\left(1,\,0,\,0\right)^{\rm T},$$

from which we conclude that the induced emission is perpendicular to the surface of the reflector. The (almost) perpendicular emission is also understood from Fig. 4.2, where the vectors and wavefronts of the incoming hidden photon field (light green) and the induced emission (orange) are depicted. Because the wave vector $\mathbf{k}$ for the DM field is tiny ($k_{\rm in} \sim 10^{-3}\omega$), the wave length is far longer than that of the induced emission ($k_{\rm out} = \omega$). In order to fulfill the boundary condition on the reflector, the photon should be emitted almost perpendicularly to the surface. This is in analogy to the Snell's law for the propagation of light between two different media with different refractive indices.

Therefore, a spherical dish with its radius larger than the wave length of the emission can focus the emission to the curvature center as depicted in Fig. 4.1. The power concentrated in the curvature center is

$$P_{\rm center} \approx A_{\rm dish}\langle|\mathbf{E}_{\rm DM,\,||}|^2\rangle = \langle\alpha^2\rangle_{\rm dish}\chi^2\rho_{\rm CDM}A_{\rm dish},$$

where $A_{\rm dish}$ is the area of the dish and $\alpha = \cos\theta$ for θ the angle between the plane and the $\mathbf{E}_{\rm DM}$, and the average is taken over the surface of the mirror. For random vector direction, α is irrelevant to the arrangement of the dish or the sidereal time and

$$\langle\alpha^2\rangle = \frac{1}{4\pi}\int_{-1}^{1} d\cos\vartheta\int_0^{2\pi} d\varphi\sin^2\vartheta = \frac{2}{3}.$$

Solving the equation for χ yields

$$\chi_{\rm sens} = 4.5 \times 10^{-14} \left(\frac{P_{\rm det}}{10^{-23}{\rm W}}\right)^{1/2} \left(\frac{0.3\,{\rm GeV/cm^3}}{\rho_{\rm CDM,\,halo}}\right)^{1/2} \left(\frac{1\,{\rm m^2}}{A_{\rm dish}}\right)^{1/2} \left(\frac{\sqrt{2/3}}{\alpha}\right),$$

and in detectable photon rate $R_{\gamma,\,\rm det}$,

$$\chi_{\rm sens} = 5.6 \times 10^{-12} \left(\frac{R_{\gamma,\,\rm det}}{1\,{\rm Hz}}\right)^{1/2} \left(\frac{m_{\gamma'}}{\rm eV}\right)^{1/2} \left(\frac{0.3\,{\rm GeV/cm^3}}{\rho_{\rm CDM,\,halo}}\right)^{1/2} \left(\frac{1\,{\rm m^2}}{A_{\rm dish}}\right)^{1/2} \left(\frac{\sqrt{2/3}}{\alpha}\right). \tag{4.6}$$

4.1.2 Further remarks

Effects of refraction

For the search of hidden photons from the sun with a helioscope, the chamber where the $\gamma' \to \gamma$ conversion occurs should be evacuated to high vacuum because the transition probability depends on the refractive index n as

$$P\left(\gamma' \to \gamma\right) = \frac{4\chi^2}{\left(1 + \frac{2\omega^2(n-1)}{m_{\gamma'}^2}\right)^2} \sin^2\left(\frac{m_{\gamma'}^2 L \sqrt{\left(1 + \frac{2\omega^2(n-1)}{m_{\gamma'}^2}\right)^2}}{4\omega}\right),$$

where ω is the energy of incoming hidden photons. Hidden photons from the Sun are assumed to be highly relativistic for the most part of the interest mass range, and tiny deviation of the refractive index n from 1 would cause severe degradation in the sensitivity.

On the other hand, hidden photons of CDM source are non-relativistic $k \ll \omega$, and normal atmosphere $(n-1) \sim 10^{-4}$ does not reduce the sensitivity at all.

Direction of the induced emission

The effect of tiny velocity of dark matter particles has already been shown in Fig. 4.2. The boundary condition imposes

$$\mathbf{k}_{\rm in} \cdot \mathbf{x}|_{\mathbf{x}=(x=0,y,z)} = \mathbf{k}_{\rm out} \cdot \mathbf{x}|_{\mathbf{x}=(x=0,y,z)},$$

resulting in the condition

$$\mathbf{k}_{\rm in,||} = \mathbf{k}_{\rm out,||}.$$

In addition, from the energy conservation, we obtain

$$\omega = |\mathbf{k}_{\rm out}| = \sqrt{m_{\gamma'}^2 + |\mathbf{k}_{\rm in}|^2}.$$

Combining above equations, we have an explicit formula for the outgoing wave vector $\mathbf{k}_{\rm out}$:

$$\mathbf{k}_{\rm out} = \sqrt{m_{\gamma'}^2 + |\mathbf{k}_{\rm in,\perp}|^2}\mathbf{n} + \mathbf{k}_{\rm in,||}.$$

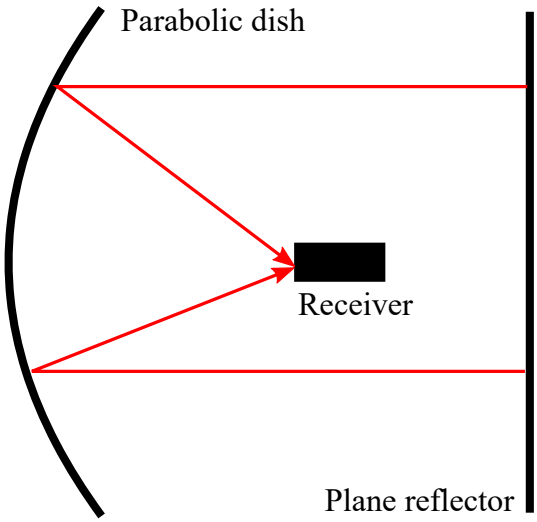

Figure 4.3: Schematic view of a new method using an additional plane reflector to make use of parabolic dishes.

We thus find that the induced electromagnetic waves are emitted with a small angle

$$\psi_{\rm out} \simeq \frac{|\mathbf{k}_{{\rm in},||}|}{m_{\gamma'}} \sim 10^{-3} \sin\left(\psi_{\rm in}\right) \times \left(\frac{v}{10^{-3}c}\right), \tag{4.7}$$

where $\psi_{\rm in}$ is the incident angle of incoming DM particles. The effects of the direction of the induced emission are discussed in detail in Ref. [124, 125].

4.1.3 Experiment employing the dish method

An experimental search using the dish method described above were performed by Horie et al. [27, 28, 29], where a large parabolic antenna for CS broadcast reception was employed to search for hidden photons with the mass $m_{\gamma'} \sim 50\,\mu$eV.

Experimental set-up

Dish antennas for BS or CS broadcast reception are commercially available, and relatively large aperture dishes ($\sim$ m) can be obtained at low cost. However those dishes have parabolic shapes instead of a spherical shape required to focus photons induced by non-relativistic hidden photons, and most of them have long diameter in comparison with the focal length, which spoils the approximation of a parabolic shape to a spherical shape.

In order to overcome this problem, a new method using an additional plane reflector was invented [29, 125]. Figure 4.3 shows a schematic view of the method. Hidden photons induce emission of an electromagnetic wave perpendicular to the surface of a plane reflector, producing a plane wave normal to the reflector. A parabolic surface concentrates plane waves to the focal point, then the emission is detected by a receiver placed at the standard position of parabolic dish antennas.

Figure 4.4 shows photographs of the experimental set-up, including a parabolic dish (upper left), a plane reflector (upper right), and a framework to fix relation between the dish and the plane reflector (bottom). The parabolic dish (SXT-220, Anstellar,

Figure 4.4: Photographs of the set-up of the experiment described in Ref. [27, 28, 29]. (upper left) Parabolic dish of 2.2 m diameter and 77 cm focal length. (upper right) Plane reflector made out of four aluminum plates of 1.2 m (height) × 1.2 m (width) × 2 mm (thickness). (bottom) Combination of the dish and the plane reflector.

China) is 2.2 m diameter and 77 cm focal length, and designed for CS and BS broadcast reception. The gain of the dish was estimated by measuring intensity of signals from broadcast satellites, and agrees with the value provided by the manufacturer. The plane reflector was constructed out of four pieces of aluminum plates with 2 mm thickness. Five spring mounts are installed for each plate to align the mirror, and a theodolite was used to confirm the flatness. The frame to hold the relation between the dish and the plane reflector was constructed using an extruded aluminum construction system offered by MISUMI Corporation.

A low noise block down-converter with a feedhorn (4506B, Norsat, Canada) was used for a receiver. The local oscillation frequency of the converter is 11.3 GHz, with which the input signal would be down-converted to $\mathcal{O}$(GHz) then transferred to a signal analyzer described below using a coaxial cable. The receiver accepts emissions with frequency in the range from 12.25 GHz to 12.75 GHz, corresponding to $950-1450$ MHz after the down conversion. A calibration of the gain of the receiver was performed

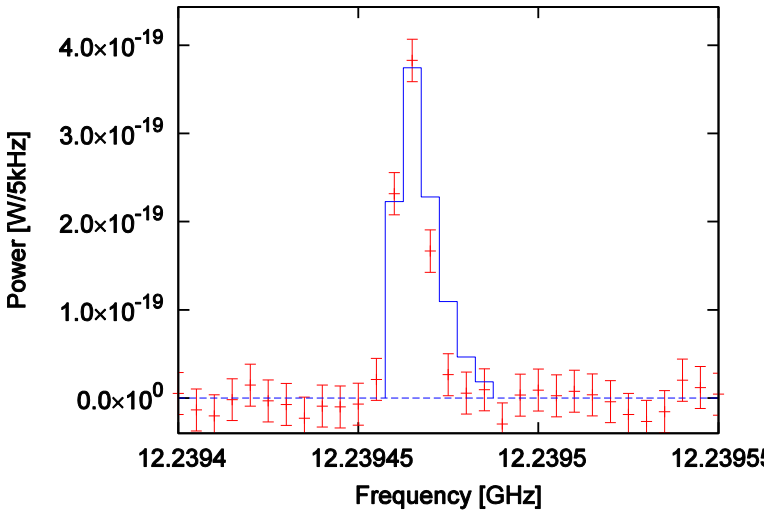

Figure 4.5: Expected peak of DM signal in the spectrum. The emission induced by non-relativistic hidden photons would be detected as a sharp peak with width $\Delta f/f \sim 10^{-6}$. We can thus enhance the signal-to-noise ratio by making use of spectral information.

using an Eccosorb (AN-73, E&C Engineering, Japan), which can be regarded as a black body emitter in the frequency range of interest. The Eccosorb at liquid nitrogen temperature and at room temperature were measured by the receiver and the output signals were compared to yield the gain of the receiver.

Output of the converter was connected to a signal analyzer (FSU-4, Rohde&Schwarz, Germany), which handles signals in the frequency range of 10 Hz − 4GHz. Signal analyzers combine superheterodyne down-conversion, digital sampling with fast ADCs, and digital processing (fast Fourier transformations), enabling to lower statistical limitations in comparison with a primitive spectrum analyzer under the same period of measurements.

Measurement

Emissions induced by non-relativistic hidden photons have a frequency corresponding to the mass $\omega \sim m_{\gamma'}$, and thus the signal forms a sharp peak in the spectrum. The broadening of the peak is characterized by the dispersion of DM velocity. Assuming the isothermal halo, the width of the peak will be[3] $\Delta f/f \sim 10^{-6}$, and the shape of the peak is expected to be as in Fig. 4.5. The resolution of the spectrum acquisition was configured so that the peak would be observed effectively.

The experimental run was performed from November 25th, 2014 to November 28th, 2014, where they found no extra peaks other than from spurious emissions. In order to confirm those spurious peaks are not of HPDM origin, measurements with the receiver at the focus and apart from the focus was compared to find out those peaks appear in both spectra. The experimental bound for the photon-HP mixing parameter χ obtained in the run is shown in Fig. 4.6. The sensitive mass range is limited by the narrow frequency range accepted by the receiver.

[3]Because the emission has an energy $\omega \simeq m_{\gamma'} + \mathbf{p}^2/2m_{\gamma'}$ and the velocity dispersion is $\Delta v \sim v \sim 10^{-3}$ for an isothermal halo, we roughly estimate the width as $\Delta f/f \sim (10^{-3})^2 = 10^{-6}$.

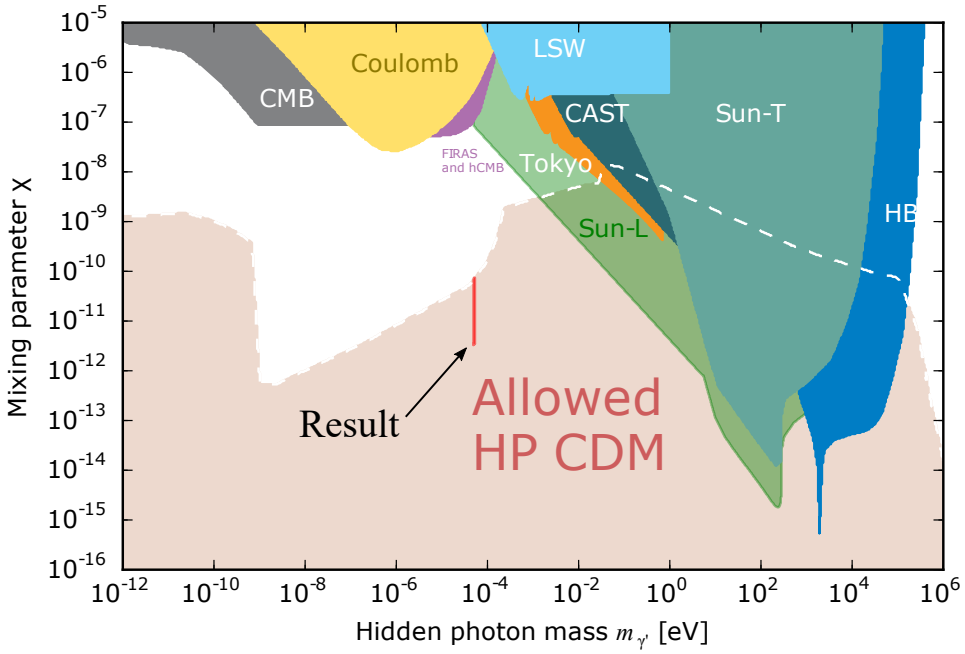

Figure 4.6: Experimental bound for the photon-HP mixing parameter χ obtained in the search by Horie et al. [27, 28, 29] assuming that DM density $\rho_{\rm CDM} = 0.3\,{\rm GeV/cm^3}$ totally consists of non-relativistic hidden photons.

4.2 Other methods

In the previous section, we examined the dish method and reviewed a manifestation of the method in RF region. In the method, the kinetic mixing $-(\chi/2)F_{\mu\nu}X^{\mu\nu}$ induces emission from a surface of a reflector, which is received in the center of a sphere with amplification proportional to the area of the dish.

Other amplification methods are also available and, in fact, have been used in experimental searches for axion DM. In this section, we review other methods to search for hidden photon CDM.

4.2.1 Cavity search

As described in Sec. 2.3.2, experimental searches for axion DM using microwave cavities have been done by some groups. Use of a resonant cavity is also effective to search for hidden photon CDM, and the results for axion DM obtained in the past experiments can be translated to bounds for the photon-HP mixing parameter χ [25]. In hidden photon DM searches, an application of a magnetic field is not required.

Photon fields inside a cavity can be expanded as

$$\mathbf{A}(\mathbf{x}) = \sum_i \alpha_i \mathbf{A}_i^{\rm cav}(\mathbf{x}),$$

where $\mathbf{A}_i^{\rm cav}$s represent cavity modes. The equation of motion is written in terms of the expansion coefficients α_i as

$$\left(\frac{d^2}{dt} + \frac{\omega_0}{Q}\frac{d}{dt} + \omega_0^2\right)\alpha_i(t) = b_i \exp(-i\omega t),$$

with ω_0 the frequency of the cavity and Q the quality factor, and the driving force b_i takes the following form using the hidden photon field $\mathbf{X}$:

$$b_i = \chi m_{\gamma'}^2 \frac{\int dV \mathbf{A}_i^{\rm cav*}(\mathbf{x}) \cdot \mathbf{X}}{\int dV \mathbf{A}_i^{\rm cav*}(\mathbf{x}) \cdot \mathbf{A}_i^{\rm cav}(\mathbf{x})}.$$

The asymptotic solution for the equation is

$$\alpha_i(t) \equiv \alpha_{i,0} \exp(-i\omega t) = \frac{b_i}{\omega_0^2 - \omega^2 - i\frac{\omega\omega_0}{Q}} \exp(-i\omega t).$$

The energy stored in the cavity U is then given by

$$\begin{aligned} U &= \frac{|\alpha_{i,0}|^2 \omega^2}{2} \int dV \mathbf{A}_i^{\rm cav*}(\mathbf{x}) \cdot \mathbf{A}_i^{\rm cav}(\mathbf{x}) \\ &\xrightarrow[\omega=\omega_0\sim m_{\gamma'}]{\text{at resonance}} \chi^2 Q^2 m_{\gamma'}^2 \frac{\left|\int dV \mathbf{A}_i^{\rm cav*}(\mathbf{x}) \cdot \mathbf{X}\right|^2}{\int dV \mathbf{A}_i^{\rm cav*}(\mathbf{x}) \cdot \mathbf{A}_i^{\rm cav}(\mathbf{x})} \\ &= 2\chi^2 Q^2 \rho_{\rm CDM} \frac{\left|\int dV \mathbf{A}_i^{\rm cav*}(\mathbf{x}) \cdot \hat{\mathbf{n}}\right|^2}{\int dV \mathbf{A}_i^{\rm cav*}(\mathbf{x}) \cdot \mathbf{A}_i^{\rm cav}(\mathbf{x})} \equiv 2\chi^2 Q^2 \rho_{\rm CDM} V \mathcal{G}, \end{aligned}$$

where we have used $\mathbf{X} = \hat{\mathbf{n}}(\sqrt{2\rho_{\rm CDM}}/m_{\gamma'})$ with $\hat{\mathbf{n}}$ the direction of hidden photons. The output power is then,

$$\mathcal{P}_{\rm out} = \kappa \frac{U}{Q} \omega_0 = \kappa \chi^2 m_{\gamma'} \rho_{\rm CDM} Q V \mathcal{G},$$

where κ is the coupling to the detector.

Translation of the results of past cavity experiments is carried out in Ref. [25], and the bounds are shown in Fig. 4.7. The pink colored region around $m_{\gamma'} \sim 10^{-5}\,\mathrm{eV}$ assumes the direction of hidden photons pointing random directions, while the purple colored area supposes a fixed direction.

4.2.2 Hidden photon 'radio'

Another novel method using a tunable resonant LC circuit was recently proposed by several authors [126, 30]. Although the method using a cavity has a high sensitivity for hidden photon CDM, sensitive mass is limited to $m_{\gamma'} \gtrsim \mu$eV by a practical size of a cavity. In the low mass region, we can search for hidden photons by constructing a 'radio' in analogy to ordinary radio receivers which catches ordinary electromagnetic waves.

Because of the existence of the kinetic mixing, standard radios might also detect the signal from hidden photon CDM, though its intensity is extremely feeble and the signal would be buried in noise from ambient electromagnetic waves. We thus need electromagnetic shields inside which the radio is placed, analogous to placing a wall in the LSW method described in Sec. 3.2.1.

However, the existence of a shield would affect the interior field because a conducting wall responds to tiny electromagnetic fields of HP origin. From (3.7) we read off an effective current $j^\mu_{\rm eff} = -\chi m_{\gamma'}^2 S^\mu$ induced by the hidden photon field S^μ. Suppose a cylinder of radius R as a shield, and the effective current to be

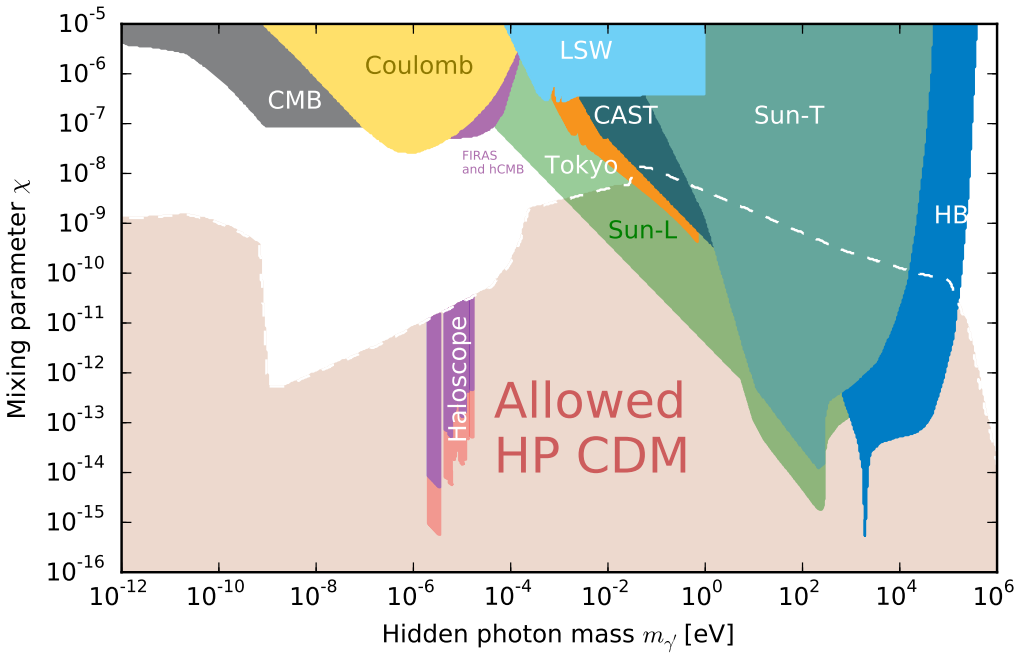

Figure 4.7: Experimental bounds for the photon-HP mixing parameter χ obtained by the translation [25] of the results of past cavity experiments. The pink colored region around $m_{\gamma'} \sim 10^{-5}$ eV assumes the direction of hidden photons pointing random directions, while the purple colored area supposes a fixed direction.

$$\begin{aligned} \mathbf{j}_{\text{eff}}(\mathbf{x}, t) &= -\chi m_{\gamma'}^2 S e^{i m_{\gamma'} t} \hat{\mathbf{z}} \\ \rho_{\text{eff}} &= 0, \end{aligned}$$

where S is assumed to be a constant. From Maxwell's equations, the electric field $\mathbf{E}$ and the magnetic field $\mathbf{B}$ satisfy

$$\begin{aligned} \left(\nabla^2 - \partial_t^2\right) \mathbf{E} &= \partial_t \mathbf{j}_{\text{eff}} + \nabla \rho_{\text{eff}} \\ \Rightarrow \left(\nabla^2 + m_{\gamma'}^2\right) \mathbf{E} &= -i\chi m_{\gamma'}^3 S e^{i m_{\gamma'} t} \hat{\mathbf{z}} \end{aligned}$$

$$\begin{aligned} \nabla \times \mathbf{E} &= -\partial_t \mathbf{B} \\ \Rightarrow \mathbf{B} &= \frac{i}{m_{\gamma'}} \nabla \times \mathbf{E} \end{aligned}$$

with a boundary condition

$$\hat{\mathbf{z}} \cdot \mathbf{E} = 0 \qquad \text{at} \qquad r = R.$$

The solution is obtained using the Bessel function J_α as

$$\begin{aligned} \mathbf{E} &= -i\chi m_{\gamma'} S e^{i m_{\gamma'} t} \left(1 - \frac{J_0(m_{\gamma'} r)}{J_0(m_{\gamma'} R)}\right) \hat{\mathbf{z}} \\ &\approx i\chi \sqrt{\rho_{\text{CDM}}} e^{i m_{\gamma'} t} \hat{\mathbf{z}} \times m_{\gamma'}^2 (R^2 - r^2) \end{aligned}$$

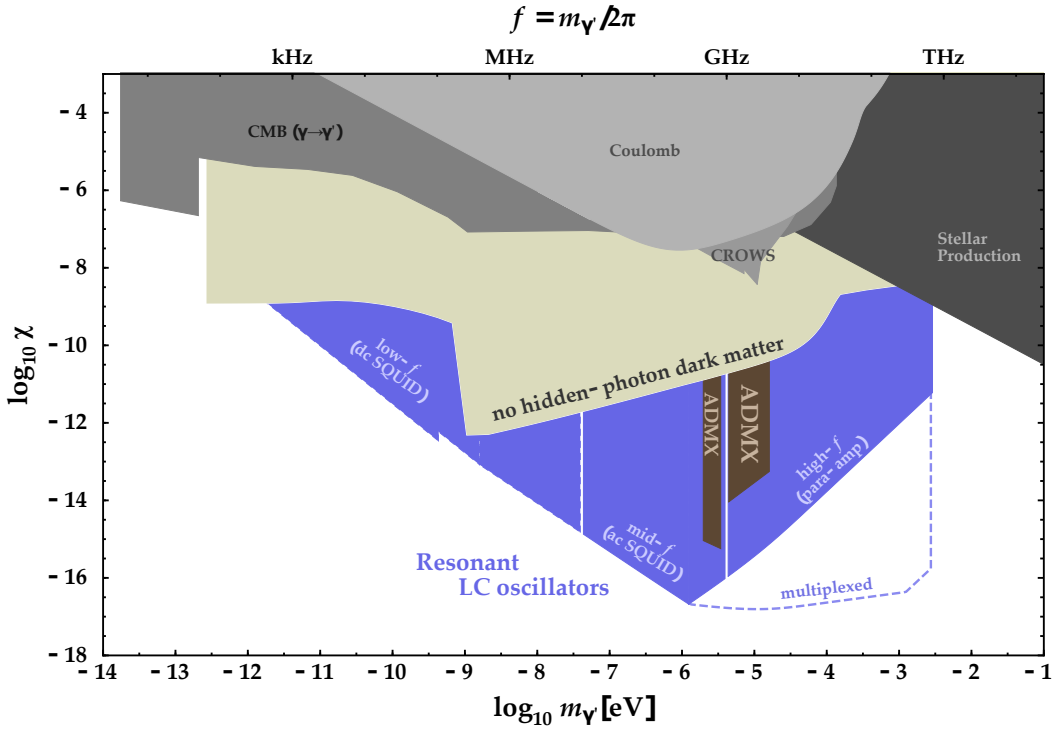

Figure 4.8: Expected sensitivity achieved by the use of a LC-resonator (colored blue). Taken from Ref. [30].

$$\begin{aligned} \mathbf{B} &= -\chi m_{\gamma'} S e^{i m_{\gamma'} t} \frac{J_1(m_{\gamma'} r)}{J_0(m_{\gamma'} R)} \hat{\boldsymbol{\phi}} \\ &\approx -\chi \sqrt{\rho_{\rm CDM}} e^{i m_{\gamma'} t} \hat{\boldsymbol{\phi}} \times m_{\gamma'} r. \end{aligned}$$

We thus conclude that the contribution of the circumferential magnetic field rather than the electric field is dominant for $m_{\gamma'} R \ll 1$.

Circumferential magnetic fields can be picked up by toroidal solenoids in the same way as a clamp meter. In order to acquire high sensitivity, a tunable capacitor is attached to the solenoid to form an LC resonator. The intensity of the signal magnetic field is given by

$$\begin{aligned} B_{\rm sig} &\approx Q \chi \sqrt{\rho_{\rm CDM}} \times \nu V_{\rm ind}^{1/3} \\ &\approx 3 \times 10^{-14}\,{\rm T} \times \left(\frac{Q}{10^6}\right) \left(\frac{\chi}{10^{-12}}\right) \left(\frac{\nu}{\rm MHz}\right) \left(\frac{V_{\rm ind}}{\rm m^3}\right)^{1/3} \left(\frac{\rho_{\rm CDM}}{0.3\,{\rm GeV/cm^3}}\right)^{1/2}, \end{aligned}$$

where $\nu = m_{\gamma'}/2\pi$ is the frequency, $V_{\rm ind}$ the volume of the inductor, and Q the quality factor of the resonator.

Manifestations of the method are studied in Ref. [30], and the sensitivity for the photon-HP mixing parameter χ is estimated as shown in Fig. 4.8.

Chapter 5

Experimental set-up

The method using a dish antenna described in the previous chapter seems to be relatively easy to implement and has an excellent experimental reach if we use huge dishes. However, operating it in real situations might cause unexpected systematics.

We therefore decided to construct a relatively small apparatus by combining instruments which we have used in the experiment for the solar HP search. Although the experimental reach is somewhat limited by its size, we successfully carried out the experiment and have accumulated a lot of knowledge about the method in optical region, without which future experiments would end up in failure.

In this chapter, we describe in detail the apparatus we constructed for the experimental search for hidden photon CDM. First we introduce the concept of the detector. We describe the constituents of the apparatus in the following section. We then explain the data acquisition system used in this experiment in Section 5.3.

5.1 Concept

As we described in the previous chapter, the 'dish' method for hidden photon CDM search requires following instruments in general:

- Dish
- Photodetector
- Shield from ambient emission

Needless to say, a dish plays a central role in this method. Hidden photon CDM around the surface of the dish stimulates the emission of photons perpendicular to the surface, and we use these photons as a signal of HP. The surface of the dish must possess sufficient reflectivity in the wavelength of interest, and have a spherical shape to collect the emission. A photodetector is placed at the center of the sphere to convert those photons into electric signals. Finally, we need a shield to protect the whole system from interference by the ambient emission.

In addition to these constituents, we need methods for background measurements to attain higher sensitivity. If the detector response is perfectly stable, we only have to know the response under quiet circumstances with enough accuracy. It is in general not the case in the real situation. For the frequency range in which we can measure the spectrum with a sufficient resolution, we can use the spectrum. Another method is simply to measure the signal and the background repeatedly.

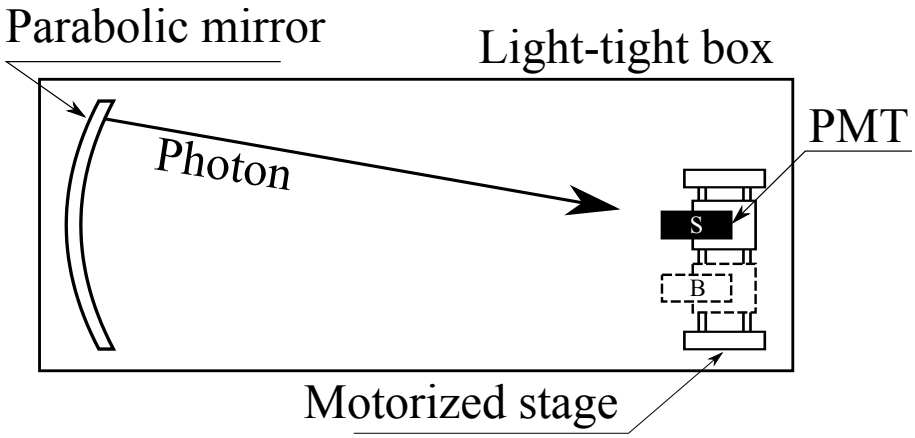

Figure 5.1: Schematic of the apparatus. Photons are emitted from the surface of the mirror and converge to a small region at about twice the focal length of the mirror. A photon-counting photomultiplier tube (PMT) is placed at the point of convergence and detects emitted photons. The PMT is mounted on a motorized stage, which shifts the position of the detector to enable background noise measurements. Devices described above are installed in a light-tight box for ambient light shielding.

We fortunately have optical instruments, including a metallic mirror and a photomultiplier, and experiences for their operation in the experimental search for solar hidden photons [21]. We thus decided to focus on the search in the optical region.

Figure 5.1 shows a schematic diagram of the apparatus. Photons are emitted from the surface of the concave mirror and converge to a small region at about twice the focal length of the mirror. A photon-counting photomultiplier tube (PMT) is placed at the curvature center of the mirror and detects emitted photons. The PMT is mounted on a motorized stage, which shifts the position of the detector to enable background noise measurements. From now on, we call the signal-taking position as 'position S' and background-taking position as 'position B'.

Our mirror does not have a spherical shape but a parabolic surface. It is, however, substitutable because the mirror has a long focal length compared to its diameter, and the surface can be approximated as a spherical surface with enough accuracy. We study the feasibility in detail in the next section.

The mirror and the detector should be rigidly held by a frame to maintain their relative positions. Figure 5.2 depicts the conceptual design of the apparatus. The black ring at the right-hand side represents the mirror used as a 'dish'. The long focal length of the mirror enforces the long distance between the photodetector and the mirror. Some braces are required to reinforce the structure.

Instruments described above should be shielded from the ambient light. The light-tightness is of great importance because a small light leak can spoil the whole result.

5.2 Instruments

In this section, we describe in detail the instruments which are combined to make the whole apparatus.

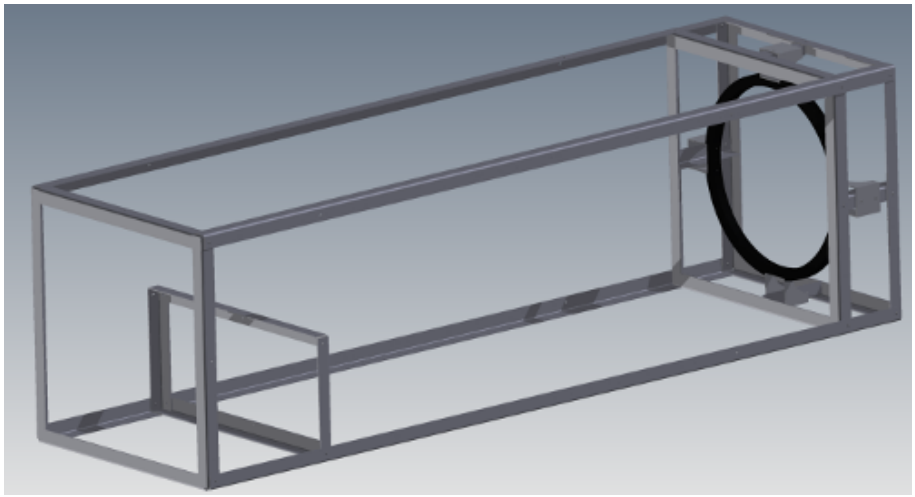

Figure 5.2: The framework of the apparatus. The black ring at the right-hand side represents the mirror used as the 'dish'.

	Characteristics
Manufacturer	Yamada kogaku kogyo Co., Ltd.
Outside diameter	499.5 mmϕ
Focal length	1,007 mm
Focal diameter	1.5 mmϕ
Material	Soda glass
Thickness	19 mm
Weight	$\sim$ 9 kg
Surface finishing	Al + SiO
Accessories	A mirror holder which consists of two aluminum rings (black coatings on anodized aluminum)

Table 5.1: Characteristics of the parabolic mirror. The mirror had been used in the experimental search for solar hidden photons [21, 22].

5.2.1 Mirror

Table 5.1 shows the characteristics of the mirror, and Fig. 5.3 is a photograph of the mirror. The mirror had been used in the experimental search for solar hidden photons [21, 22]. We also show the reflectance of the mirror measured by the manufacturer in Fig. 5.4. The vertical axis shows the reflectance and the horizontal axis shows the wavelength. We see that the reflectance exceeds 80% for the wavelength region $300 - 650$ nm, where the photomultiplier described below is sensitive.

The difference in the usages of the mirror between the previous experient and the dish method is schematically drawn in Fig. 5.5. The upper panel shows a schematic of the solar hidden photon search, while the bottom depicts the hidden photon CDM search. The difference comes from the velocity of hidden photons: photons are assumed to be relativistic in the solar hidden photon search, which validates $\gamma - \gamma'$ oscillation picture, and photons are accumulated to the focal point of the parabolic mirror. On the other hand, because CDM hidden photons are nonrelativistic $v \sim 10^{-3}c$, the directions of emission from the mirror are less sensitive to the direction of incoming hidden photon.

Figure 5.3: The parabolic mirror equipped with the holder.

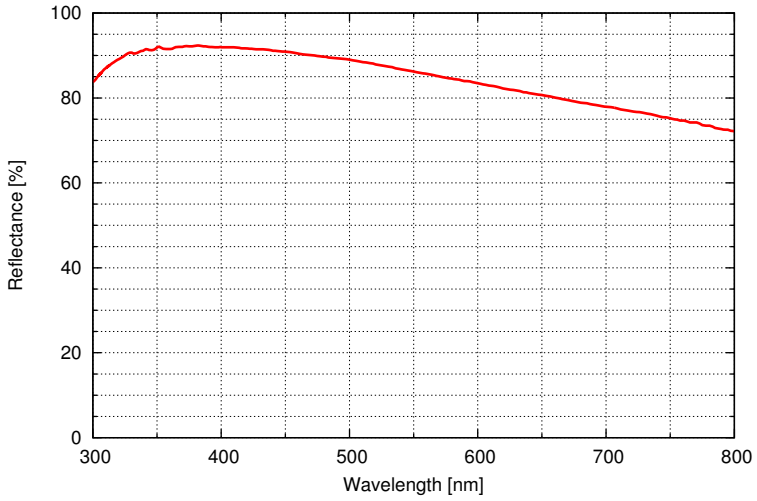

Figure 5.4: Reflectance of the mirror measured by the manufacturer. The vertical axis shows the reflectance and the horizontal axis shows the wavelength.

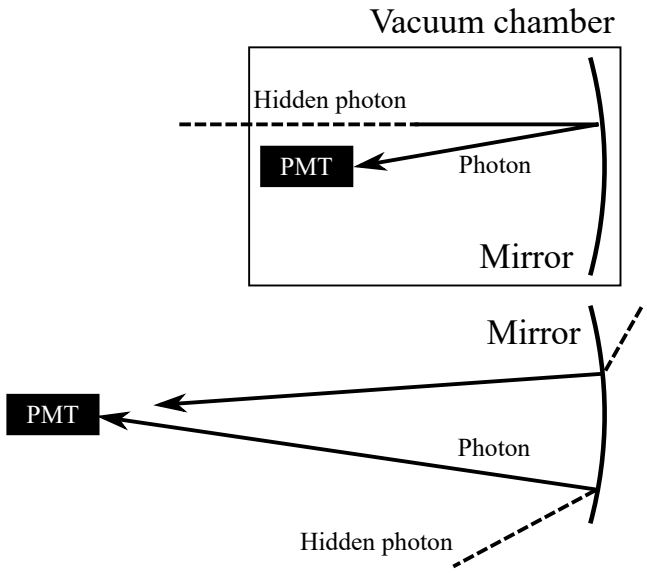

Figure 5.5: Difference in the usages of the mirror. The upper panel shows a schematic of the solar hidden photon search, while the bottom depicts the hidden photon CDM search.

Our mirror has a parabolic shape instead of a spherical shape. This substitution is acceptable because the mirror has a long focal length compared to the diameter, and is well approximated to a spherical surface. In the following, we show its feasibility and estimate the broadening of the light spot.

A parabola can be described by

$$y = \frac{1}{4f}x^2,$$

where x, y are Cartesian coordinates and f the focal length. For simplicity, we put $f = 1\,\mathrm{m}$ and use a normalization where $1\mathrm{m} = 1/4$ so that the above formula is simplified to $y = x^2$. A line which passes through $(t,\, t^2)$ and is normal to the parabola is then written as

$$\begin{aligned} y - t^2 &= -\frac{1}{2t}(x - t) \\ \Leftrightarrow x &= 2t^3 - 2t\left(y - \frac{1}{2}\right). \end{aligned}$$

We find that at the plane $y = 2 \times f = 2\,\mathrm{m}(= 1/2)$, x simply obeys $x = 2t^3$. Using the diameter of the mirror $250\,\mathrm{mm} = 1/16$, we estimate the broadening of the spot at $y = 2f$ as

$$r = 2 \times \left(\frac{1}{16}\right)^3 \times \frac{4\,\mathrm{m}}{1} = 2\,\mathrm{mm}.$$

The photomultiplier described below has an effective area of 11 mm radius, from which we conclude that the parabolic mirror is feasible.

Figure 5.6 depicts light rays emitted from the parabolic surface. The left panel shows the entire picture of the light rays and the parabola at the bottom. The right panel is an enlarged view around the point of convergence. For the figure we used the actual value $f = 1007\,\mathrm{mm}$ for the focal length, and the values are expressed in mm.

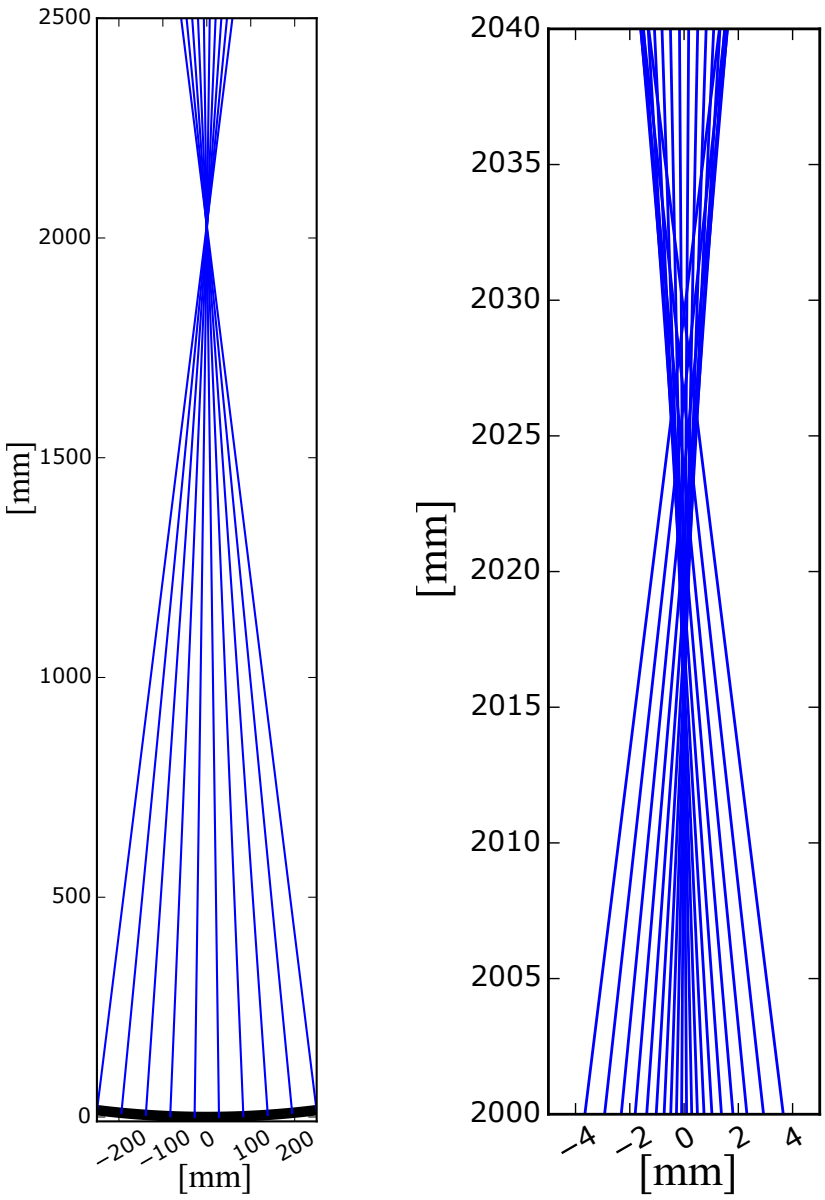

Figure 5.6: Light rays emitted perpendicularly to the surface of the parabora.

We can see from the right panel that the position of concentration locates slightly farther than the point where $y = 2f$. Additionally, this figure tells that the position accuracy in the direction parallel to the optical axis is not quite severe compared to the accuracy required for the adjustment in a plane vertical to the optical axis.

5.2.2 Framework

We have to ensure that the relative position between the photodetector and the mirror is fixed during the whole period of operation. For that purpose, a framework which mounts the photodetector and the mirror was constructed.

We decided to use slotted angle bars (Fig. 5.7) to construct the frame because of the robustness, the convenience, and the cheapness of the system. Slotted angle bars are combined together by bolts and nuts, and can be easily cut by a dedicated cutter.

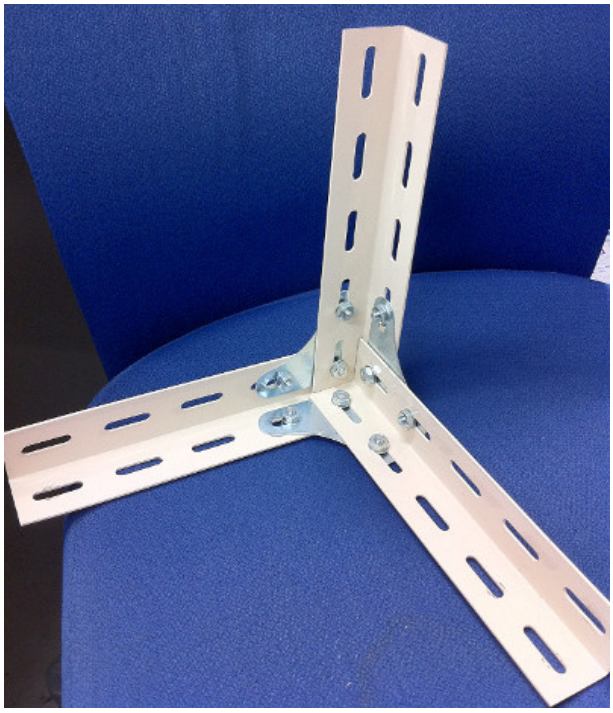

Figure 5.7: Slotted angle bars combined together to form a right angle.

Its handiness and flexibility enable quick construction of the apparatus.

The dimension of the framework is determined by the characteristics of the mirror. As described in the previous section, it is $\sim 500\,\mathrm{mm}$ in diameter, and the point of convergence is $\sim 2025\,\mathrm{mm}$ from the mirror. The frame should span the entire region without disturbing light rays.

The mirror was mounted to the frame via brackets made of aluminum (Fig. 5.8 a). The mirror holder has two tapped holes for each mounting position, and they are used to connect the brackets. The brackets have a long slot, which are used to mount the mirror system to a frame constructed by slotted angle bars (Fig. 5.8 b, c).

We then constructed the outer frame of the apparatus. Figure 5.9 is a photograph of the outer frame connected to the mirror mount. The frame has dimensions of about $70\mathrm{cm} \times 70\,\mathrm{cm} \times 250\,\mathrm{cm}$, which is long enough to mount a photodetector in the appropriate position. This simple structure is fragile and should be reinforced for long-term operation.

The reinforcement was achieved by bridging bars between the pillars, forming a truss. Figure 5.10 shows the reinforced framework. It also has the platform to mount optical instruments. The stability of the apparatus was confirmed by checking the alignment before and after a long test run.

5.2.3 Photodetector

The sensitivity to χ depends on the dark count rate and the quantum efficiency of a detector. For the optical region, there are two options for a detector, a photomultiplier tube and a CCD camera. We summarize general features of these detectors:

- Photomultiplier tube

(a)

(b)

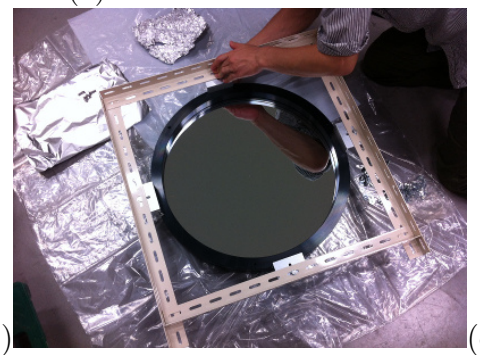

(c)

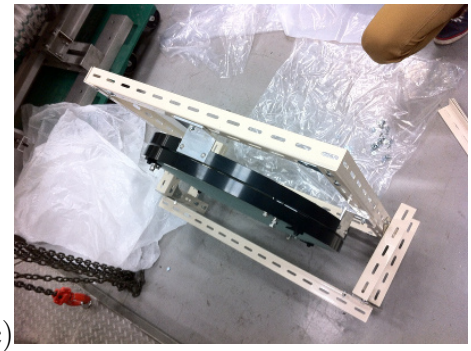

Figure 5.8: Connection of the mirror to a frame made out of slotted angle.

Figure 5.9: The outer frame of the apparatus, which has dimensions of about 70cm × 70 cm × 250 cm.

Figure 5.10: Photograph of the reinforced version of the framework. It also has a platform to mount optical instruments.

  - Relatively low dark count rate for a huge effective area without cooling (for a photon counting model)
  - Low quantum efficiency $\eta \lesssim 30\%$
  - Relatively cheap and easy to operate

- CCD camera

  - Needs LN_2 cooling to achieve low dark count, and binning to reduce readout noise
  - High quantum efficiency $\eta \gtrsim 90\%$ for back-illuminated CCDs
  - Expensive and our poor experience for the operation

For prototyping, we chose a photomultiplier tube for the photodetector. In addition to the features described above, the capability of imaging may provide concrete evidence for the signal of dark matter because of the daily modulation of the signal spot. We may use CCD cameras to confirm whether the signal is dark matter origin or not after the detection of excess in the count rate by photomultiplier tubes.

We selected a photomultiplier tube, R3550P (Hamamatsu photonics, Japan), which is a photocounting model of R3550A [31]. The characteristics of the R3550P are summarized in Tab. 5.2 and its quantum efficiency is shown in Fig. 5.11. We also show a photograph of the photmultiplier tube in Fig. 5.12. A D-type socket assembly E2924-05 (Hamamatsu Photonics, Japan) was used to divide high voltage to supply to the photomultiplier tube. Pulse-height spectra obtained by supplying pulsed light to the photodetector R3550P are shown in Fig. 5.13. A variable resistance was used to modify light intensity, and we can see peaks of single- and double-photon origin in the spectrum colored black.

The CANBERRA Model 3102D High Voltage Power Supply was used to supply high voltage to the photomultiplier tube. The 3102D is a single-width NIM module

Parameter		Description
Spectral response		$300 - 650\,\mathrm{nm}$
Peak Wavelength		$375\,\mathrm{nm}$
Photo cathode	Material	Low noise bialkali
	Minimum effective area	$22\,\mathrm{mm}\phi$
Window material		Borosilicate glass
Dynode	Structure	Circular and linear-focused
	Number of stages	10
Base		14 pin glass base
Operating ambient temperature		$-30 - +70\,^{\circ}\mathrm{C}$
Storage temperature		$-80 - +70\,^{\circ}\mathrm{C}$
[Max] Supply voltage	Anode - cathode	$1250\,\mathrm{V}$
	Anode - last dynode	$250\,\mathrm{V}$
[Max] Average anode current		$0.1\,\mathrm{mA}$

Parameter		Min.	Typ.	Max.
Cathode sensitivity	Luminous (2856 K)	$30\,\mu\mathrm{A/lm}$	$50\,\mu\mathrm{A/lm}$	-
	Q. E. @ 375 nm	-	18 %	-
Anode sensitivity	Luminous (2856 K)	$45\,\mathrm{A/lm}$	$100\,\mathrm{A/lm}$	-
Gain		-	2.0×10^6	-
Time response	Anode pulse rise time	-	$1.5\,\mathrm{ns}$	-
	Electron transit time	-	$17\,\mathrm{ns}$	-

Table 5.2: Characteristics of a photomultiplier, R3550P (Hamamatsu photonics, Japan)[31].

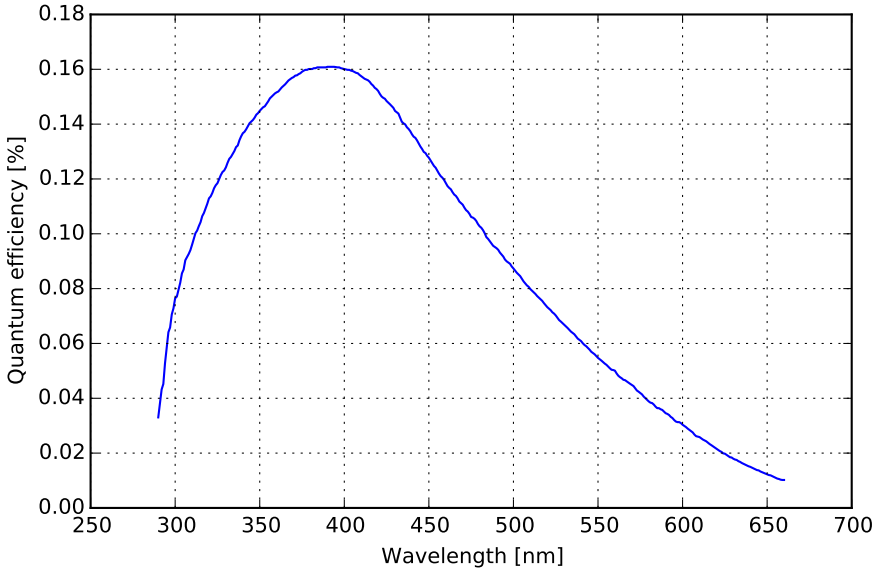

Figure 5.11: Quantum efficiency of R3550P[31].

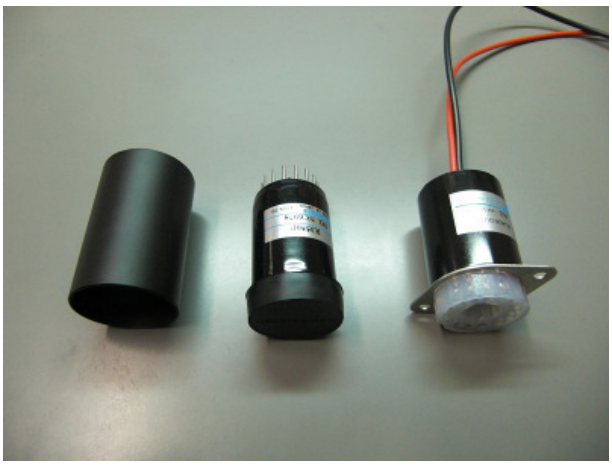

Figure 5.12: Photomultiplier tube, R3550P (Hamamatsu photonics, Japan), together with a magnetic shield case (left) and a socket assembly (right).

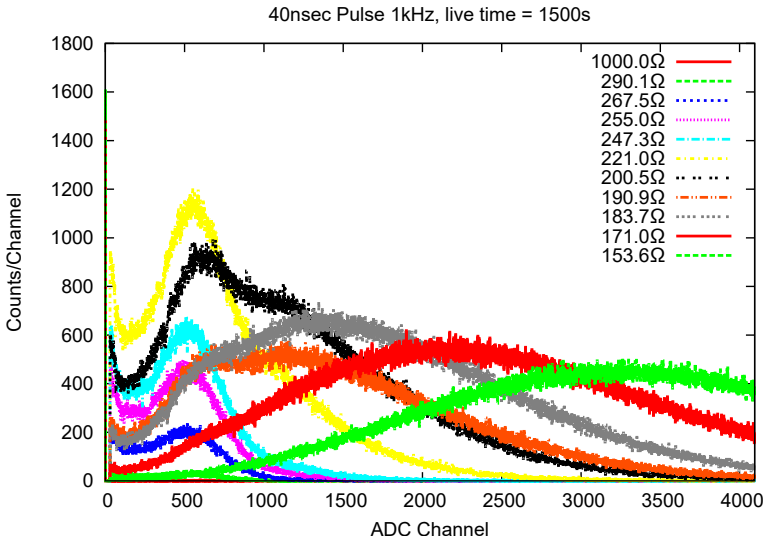

Figure 5.13: Pulse height spectra obtained by supplying pulsed light to the photodetector R3550P.

Parameter	Description
Output stability	Long term drift $\leq 0.01\%$/hr and $\leq 0.02\%$/8hr
Temperature coefficient	$\leq \pm 50$ ppm/°C
Current limit	1.3 mA maximum
Dial accuracy	$\pm 1\%$ of full scale
Meter accuracy	$\pm 0.6\%$ of full scale plus 10 volts
Operating temperature	$0 - 50$ °C
Operating humidity	$0 - 80$ %
Connectors	Rear panel SHV

Table 5.3: Performance of the CANBERRA Model 3102D High Voltage Power Supply.

and can supply ± 15 to ± 2000 V dc with continuous adjustability. Its performance is shown in Tab. 5.3.

The dark-count rate of the R3550P is about ~ 5 counts/sec, which is very quiet compared to normal photomultiplier tubes. It is widely known that the dark-count rates of PMTs are not stable. The dark-count rate mainly depends on:

- Duration from the time to begin supplying high voltage to the PMT
  In general, the dark-count rate is high at the beginning, and then decreases to a stable value.

- Exposure to intense light
  Even if HV is not supplied, exposing PMTs to intense light, such as room light, would affect the dark-count rate in the operation after the exposure. Its behavior is similar to the duration effect described above, and becomes negligible after $\sim$ day of operation.

- Ambient temperature
  The dark-count rate strongly depends on the temperature around the photocathode.

Among the effects listed above, the temperature dependence is the most problematic. In the experiment searching for solar hidden photons [21, 22], where they used the same PMT, the temperature dependence dominated the systematic error. To overcome this problem, we have to (i) stabilize the temperature around the PMT, or (ii) switch signal acquisition and background measurement frequently so that the effect would be canceled. We chose the latter solution in this experiment, and used a motorized stage described below to move the photodetector.

The dependence of the dark-count on temperature was measured before the experiment, and the result is shown in Fig. 5.14. The vertical axis shows the count rate of R3550P, while the horizontal axis shows the temperature. The temperature measurement was carried out using Pt100 platinum resistance thermometer read by HIOKI LR8401 data logger with interval of 100 ms. From the result, we derive the coefficient 0.21 Hz/°C by fitting a linear function.

5.2.4 LED

A blue light-emitting diode is placed near the photomultiplier tube to study the response of the photodetector to light after closing the light-tight box. A schematic of

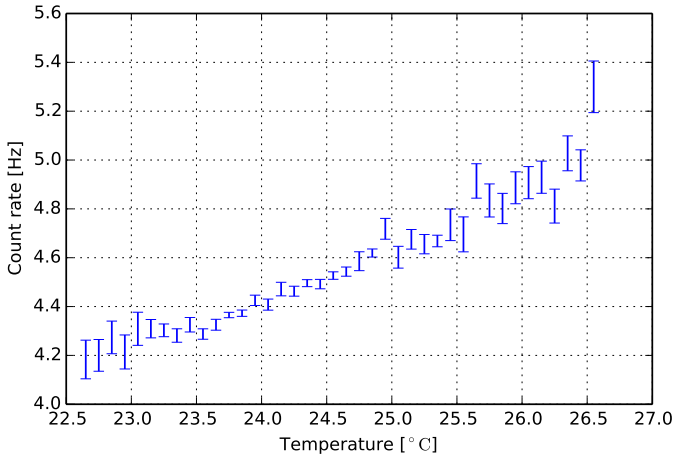

Figure 5.14: Dependence of the dark-count on temperature. The vertical axis shows the count rate of R3550P, while the horizontal axis shows the temperature.

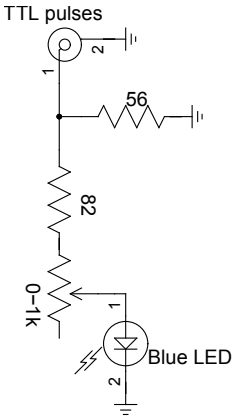

Figure 5.15: Schematic of the circuit to adjust intensity of the blue LED.

the circuit to drive the blue LED is shown in Fig. 5.15. A variable resistance is used to obtain an appropriate light emission.

5.2.5 Motorized stage

Because of the reason described in the previous section, we utilized a motorized stage to move the photodetector away from position S (and restore the position after background measurements). A photograph of the motorized stage is shown in Fig. 5.16. The ball-screw mechanism converts the rotation of a motor to the parallel movement of the stage. The motor is a stepper motor PH265M-31 (VEXTA, the United States), which operates at DC 6V power supply. The system is also equipped with two mechanical switches.

The driver circuit for the motorized stage is depicted in Fig. 5.17. It consists of a FT245RL Serial to Parallel Converter and a MP4401 Power MOS FET module. The D0-D3 pins of the FT245RL are used to control the motor via the MP4401 module, while D6-D7 are employed for the readout of the states of the switches. The FT245RL enables the control of the motor from a PC via USB connection, and we wrote a dedicated program to drive the motorized stage using C++ with the aid of the li-

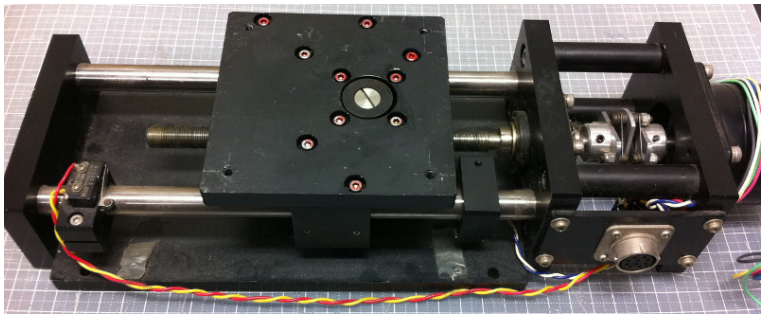

Figure 5.16: Photograph of the motorized stage. The ball-screw mechanism converts the rotation of a motor into the parallel movement of the stage.

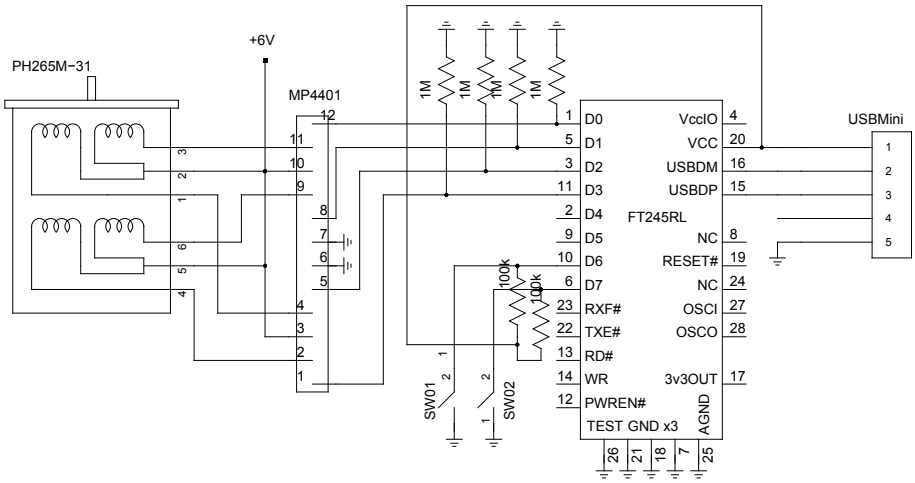

Figure 5.17: Driver circuit for the motorized stage.

brary provided by the Future Technology Devices Instruments, the manufacturer of the FT245.

5.2.6 Alignment

As described in Section 5.2.1, the alignment in the direction parallel to the optical axis ('z-axis') is not so severe, and we used a tape measure to acquire the distance from the center of the mirror.

On the other hand, the alignment in the plane perpendicular to the optical axis ('xy plane') requires an accuracy of $\sim$ mm because the effective area of the PMT was limited to 5.5 mm-radius to prevent the effect from the Cherenkov emission as described in Appendix A.

We utilized an acrylic glass with a cross scratch to obtain the right position in the xy plane with high enough accuracy. A photograph which demonstrates the usage of the acrylic glass is shown in Fig. 5.18. Because the correct position locates near $z \sim 2f$ where f is the focal length of the parabolic mirror, we would see the image of the scratch together with the scratch itself around the right position. We can then find the correct position in the xy plane by slightly moving the glass and matching the image of the cross with the cross itself. After obtaining the right position, we translate it to the position of the photodetector.

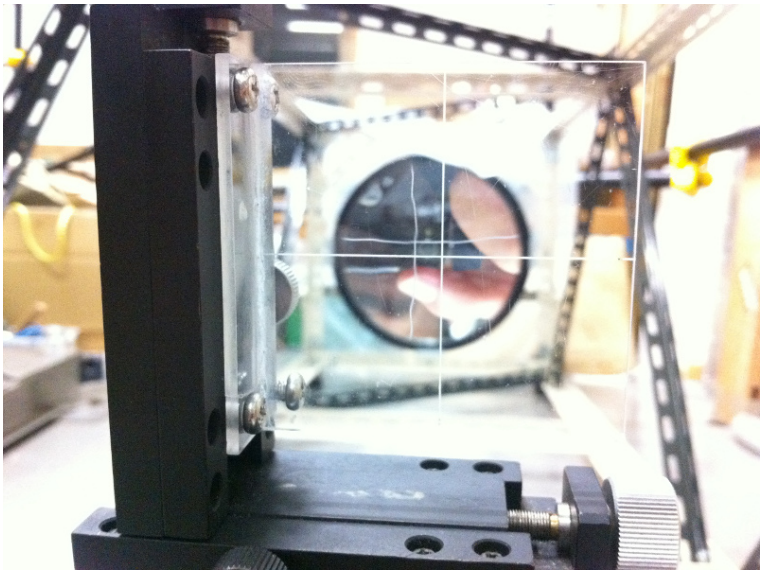

Figure 5.18: Demonstration of the usage of the acrylic glass. Because the correct position locates near $z \sim 2f$ where f is the focal length of the parabolic mirror, we would see the image of the scratch together with the scratch itself around the right position.

5.2.7 Light-tight box

We have to achieve light-tightness for the whole system described above. The light leak would cause degradation in the sensitivity, and, furthermore, may lead to wrong conclusions. In addition to the difficulty to achieve the light-tightness with high quality, our apparatus is large in dimension: $\sim 70\,\mathrm{cm} \times 70\,\mathrm{cm} \times 250\,\mathrm{cm}$. Maintaining the light-tightness for such a huge system is very challenging, and a lot of effort was paid to overcome this problem.

We decided to make a twofold light-tight box to ensure the light-tightness by turning the framework shown in Fig. 5.10 into a light-tight box, and additionally, making a larger box to cover the entire apparatus.

First we developed a scalable method to shield ambient light. A black polyethylene sheet was used for the main material because it is cheap and light, which enables scaling to a large system. Figure 5.19 shows a photograph of a table-top light-tight box to check the feasibility of the method. The box consists of a framework made out of slotted angle bars, 150 μm thick black polyethylene sheets, and bolts and nuts to stick the sheets to the frame. Gaps between the sheets are covered by black tapes for electric insulation, which is well known to have enough light-tightness. We confirmed that the light-tight box constructed with this method effectively shield the light by introducing a photodetector inside the box. Additionally, we tested whether the movement of the stage causes unexpected effects on a photodetector mounted on the stage.

After the confirmation of the feasibility of the method, we wrapped the apparatus depicted in Fig. 5.10 with black polyethylene sheets in the same way. Figure 5.20 shows photographs of the apparatus wrapped with black sheets. The left panel displays the apparatus half covered by black sheets, and the right panel shows the completed version.

We then constructed a larger light-tight box. The frame of the outer box is constructed out of slotted angle bars. It has dimensions of $1\,\mathrm{m} \times 1\,\mathrm{m} \times 3\,\mathrm{m}$, which is

Figure 5.19: Small light-tight box to check the feasibility of the method.

Figure 5.20: Photographs of the apparatus wrapped with black sheets.

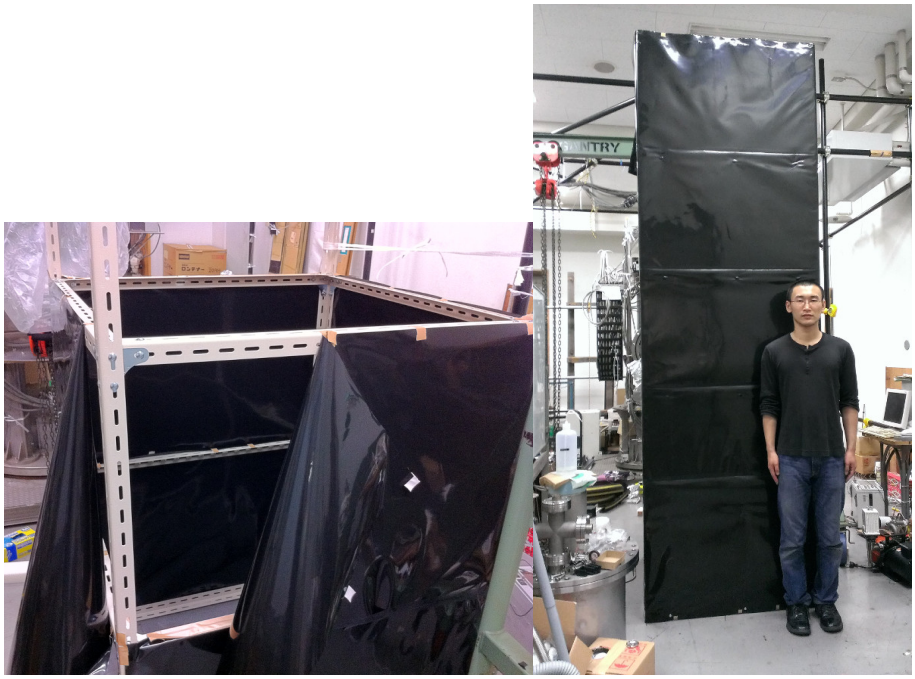

Figure 5.21: The outer light-tight box. (Left) The framework and black sheets. (Right) Comparison with the height of the author.

large enough to decouple light leakage between this box and the apparatus described above. The right panel of Fig. 5.21 shows a photograph of the outer light-tight box. After wrapping black sheets around the frame, the apparatus was introduced in the box (Fig. 5.22).

For further confirmation of light-tightness, we installed another photomultiplier tube between the apparatus and the outer light-tight box. A schematic of the cross-section of the setup is depicted in Fig. 5.23. We checked that there were no large light leakage using this photomultiplier by measuring the counts of the PMT under ON/OFF of the room lighting.

In addition to these cares for the light-tight box, we made two other efforts to make the experiment valid:

- Limiting the angle of sight of the PMT with a hood
  The hood limits the sight from the PMT so that it would not see substances near the detector. The movement of the PMT by 25mm thus does not dramatically change the sight of the PMT. Even if a light-leak occurs at a place far from the PMT, it would yield almost the same count-rate for both at position S and at position B.

- Confirming no difference in count rate at two different background-taking positions
  To confirm that our treatments were cautious enough, we carried out a test run which measured count rates at two different background-taking positions (displaced from the signal-taking position by 25 mm to the left (B1) and the right (B2)) for 5×10^5 sec, each. We found no difference in count rates at B1 and B2. This is a crucial evidence that our treatments worked well (cf. the 10th run described in A.3 in Appendix A).

Figure 5.22: The outer light-tight box and the apparatus. After the installation of instruments, both ends of the outer box were closed.

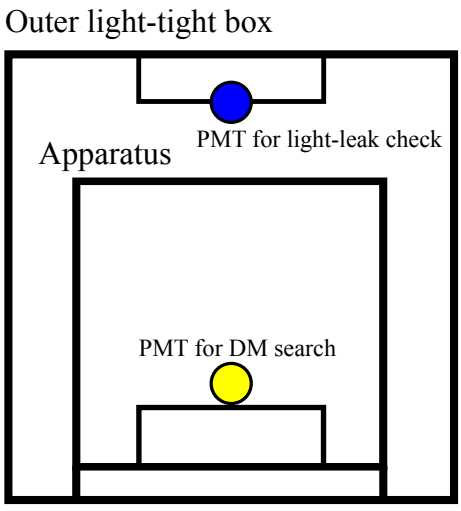

Figure 5.23: Schematic of the crosssection of the setup.

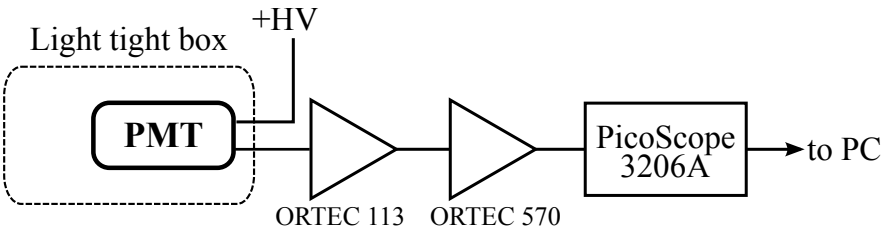

Figure 5.24: Schematic diagram of the data acquisition system.

5.3 DAQ

We need a data acquisition system which function in cooperation with the motorized stage. There are two choices for the procedure of the experimental search:

- Intermittent acquisition
  Changing storage locations according to the state of the stage.

- Continuous acquisition
  Acquiring data independent of the state of the stage. Event-by-event time stamping enables assignment of the stage state to events by an off-line analysis.

The latter choice is selected for this experiment because it can avoid complexity and time stamping can be performed with high enough accuracy.

Figure 5.24 shows a schematic diagram of the data acquisition system. The PMT output is connected to a charge-sensitive preamplifier (MODEL113, ORTEC, The United States) followed by a shaper (MODEL570, ORTEC, The United States). The signal is then sent to a digital oscilloscope (PicoScope 3206A, Pico Technology, The United Kingdom), which samples the signal at 10M samples/sec and streams the data to a computer through a USB 2.0 connection. Event triggering and pulse-height analysis are performed by a software, which records pulse heights together with arrival times.

We show a pulse shape of the photomultiplier tube and output waveforms of the charge-sensitive amplifier and the shaper in Fig. 5.25, 5.26, and 5.27, respectively.

In order to figure out whether the data acquisition system properly works, we performed a test run with a cap on the window of the photodetector. The result is shown in Fig. 5.28, where we find that any peculiar behavior does not exist and confirm that the DAQ properly works. Detailed description on the test run appears in Section A.2.

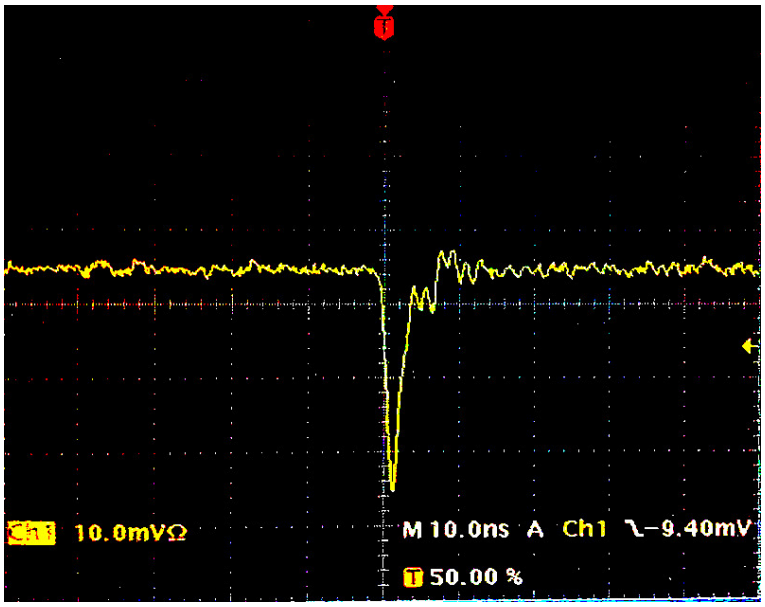

Figure 5.25: Pulse shape of the photomultiplier tube, R3550P.

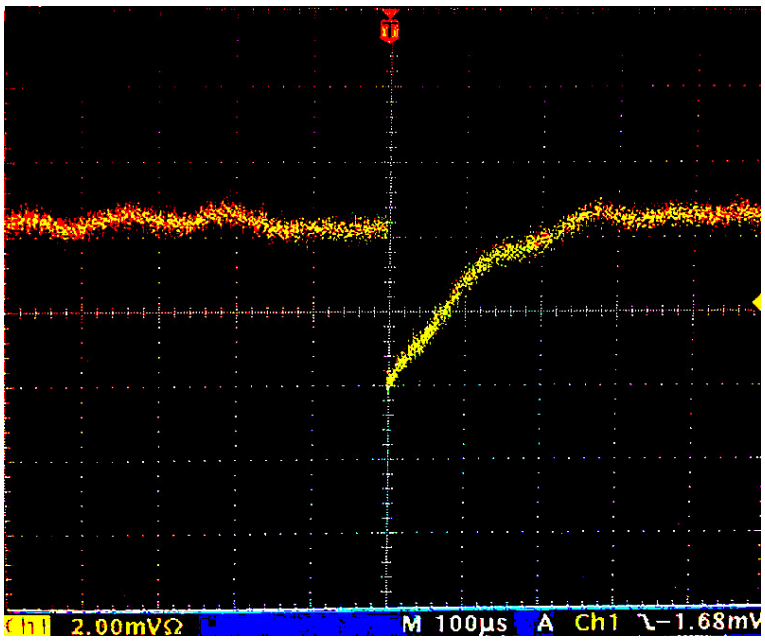

Figure 5.26: Output of the charge-sensitive amplifier, ORTEC113.

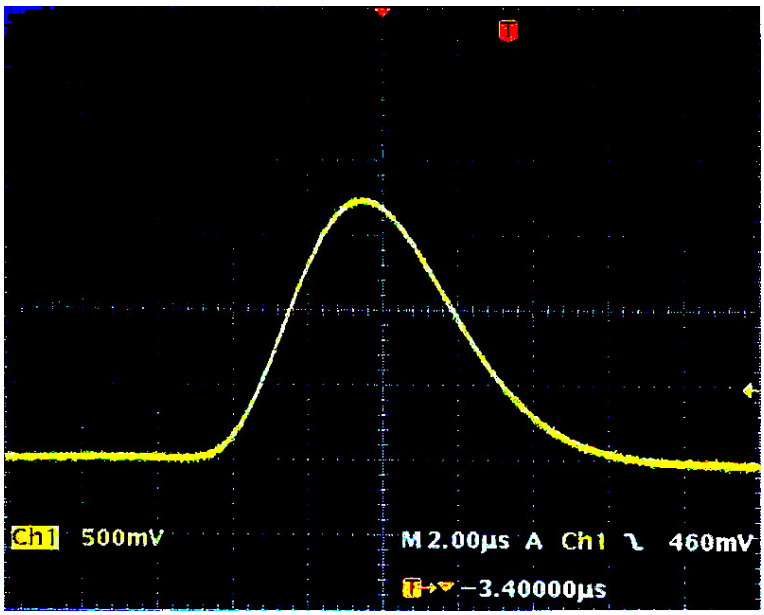

Figure 5.27: Output of the shaper, ORTEC 570.

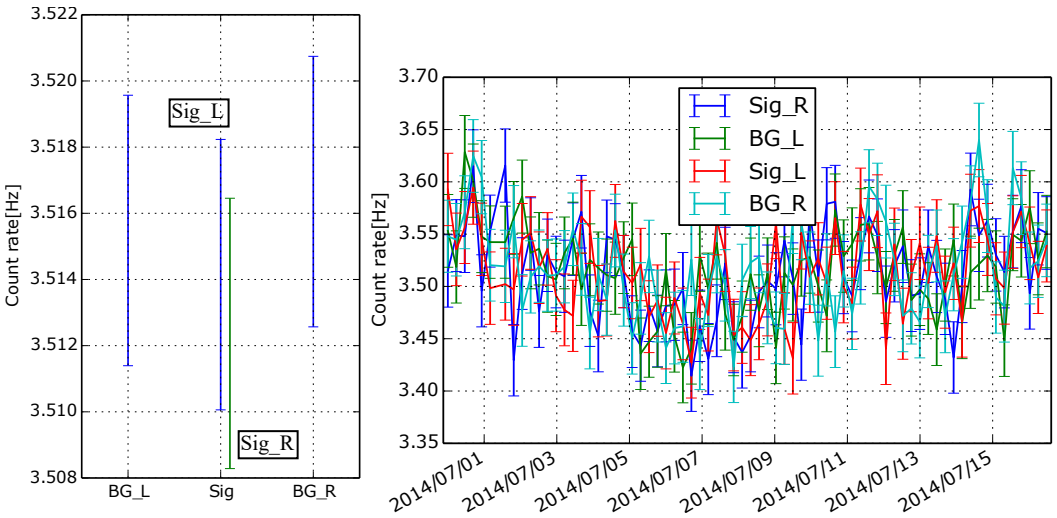

Figure 5.28: Result of a test run where the window of the photodetector was capped to make it blind to visible light. (Left) Accumulated count rates at each position. (Right) Count rates shown in time series.

Chapter 6

Measurement and analysis

Using the apparatus described in the previous chapter, we carried out the first experimental search for hidden photon CDM with the 'dish' method.

As is often the case with pioneering experiments, this experiment suffered from a lot of unexpected difficulties. Trials and errors to overcome these difficulties are described in Appendix A. In this chapter, we instead describe a straight forward way to the final result.

This chapter is organized as follows. In the first section, we describe the preparation before the measurement, including a study of the response of the photomultiplier for a single photon using the blue LED. The next chapter explains the experimental procedure and shows monitored quantities. We then analyze the data to obtain the result for hidden photon CDM in the following section.

6.1 Preparation

We settled the apparatus described in the previous chapter in the laboratory of the University of Tokyo at East longitude 139°45'47", North latitude 35°42'50". and the mirror is directed to the West because of space limitation.

Before starting the measurement, we estimated the effect of the velocity of dark matter using the geographical information described above, and studied the response of the photodetector to a single photon.

6.1.1 Movement and dispersion of the light spot

As we described in Chapter 4, the emission angle of photons due to hidden photon CDM slightly deviates from perpendicular direction. The effect of this deviation should be estimated to evaluate the efficiency of detection.

We adopted a Maxwell-Boltzmann distribution with the velocity dispersion $v_0 \sim 10^{-3}c$

$$f(\mathbf{v}) = \frac{1}{(\pi v_0^2)^{3/2}} e^{-(\mathbf{v}+\mathbf{v}_\mathrm{E})^2/v_0}, \tag{6.1}$$

which is widely used for a working hypothesis in the field of the direct detection of dark matter. The movement of the Earth $\mathbf{v}_\mathrm{E}$ in the halo deviates the center of the distribution from $\mathbf{v} = 0$ along the direction opposite to $\mathbf{v}_\mathrm{E}$. The velocity of the Earth in the galactic halo is dominated by the motion of the solar system toward the Cygnus,

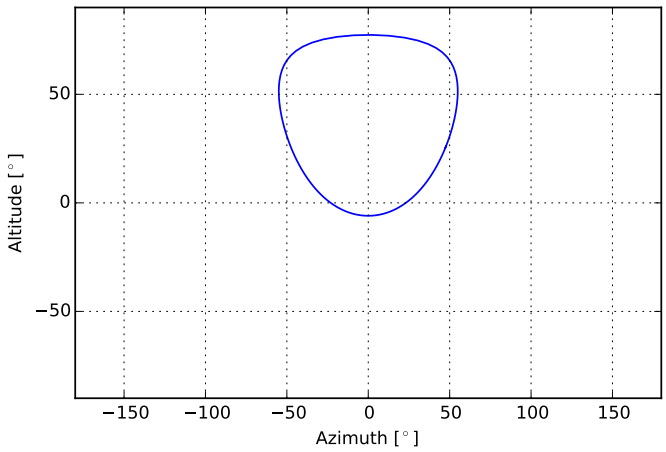

Figure 6.1: The daily movement of the point ($b = 0°$, $\ell = 90°$) in the galactic coordinate in the celestial sphere seen from the laboratory (East longitude 139°45'47", North latitude 35°42'50").

i.e. ($b = 0°$, $\ell = 90°$) in the galactic coordinate, where b is the galactic latitude and ℓ the galactic longitude.

Figure 6.1 shows the daily movement of the point ($b = 0°$, $\ell = 90°$) in the galactic coordinate in the celestial sphere seen from the laboratory. Because the mirror is directed to the West, the deviation of the center of the light spot, which comes to a maximum when the direction of DM is parallel to the mirror, is quite large for a whole day.

We can find the magnitude of deviation using Eq. 4.7 as

$$\delta = R \times v \sim 2\,\mathrm{m} \times 10^{-3} = 2\,\mathrm{mm},$$

which is small enough compared to the diameter of the effective area of the photmultiplier 22 mmϕ. Figure 6.2 shows daily movements of the center of the light spot due to the effect of dark matter 'wind'. The left panel is a calculation based on the real situation, where the mirror is directed to the West. We show a calculation for the case if we direct the mirror to the North in the right panel for comparison. Values on the x and y axes are in mm. The blue and red circles are 22 mm and 11 mm in diameter, respectively.

We also carried out a toy Monte Carlo simulation to estimate the effect of dispersion due to the motion of dark matter. For the simulation, we randomize the following three variables:

- Velocity of dark matter
  Cast according to the distribution described in Eq. 6.1.

- Time of occurrence
  Because the center of the light spot moves as described above, we take a time of occurrence of an event at random.

- Position of an emission in the mirror
  Because of the use of the parabolic mirror instead of a spherical surface, an

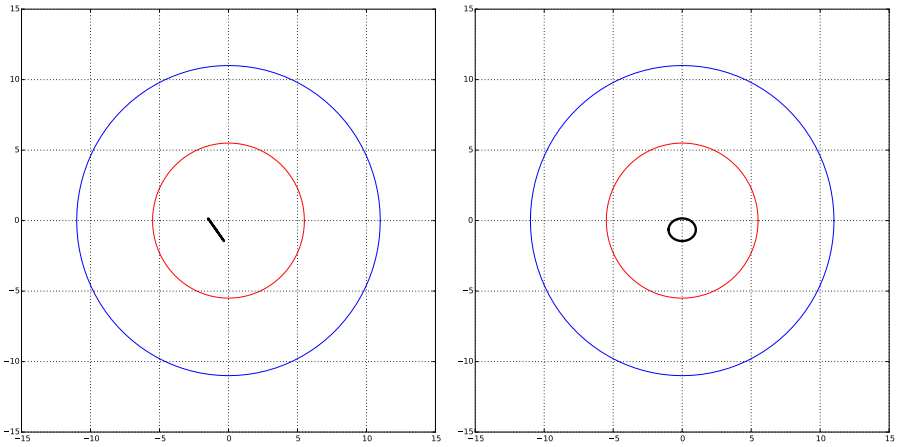

Figure 6.2: Daily movements of the center of the light spot due to the effect of dark matter 'wind'. (Left) Calculation based on the real situation, where the mirror is directed to the West. (Right) Calculation for the case if we direct the mirror to the North. Values on the x and y axes are in mm.

arrival position of the light ray in the photodetector depends on the position of the emission.

Figure 6.3 and 6.4 show the results of the simulation with 10^4 events generated in a manner described above. Figure 6.3 is a density plot of the arrival position of photons in the focal plane, and Fig 6.4 is a scatter plot. In this simulation, the slight deviation of the alignment is also taken into account. We confirmed that $\sim 99\%$ of events are in a circle of 11 mm in diameter, from which we decided to limit the effective area of the photodetector to 11 mmϕ to reduce the effect of Cherenkov emission as described in Appendix A.

6.1.2 Response of the photomultiplier to a single photon

The existence of hidden photon CDM would yield a single photon and be detected by the PMT as a single-photon event.

To study the response of the photomultiplier to a single photon, we used the LED described in Sec. 5.2.4. We supplied pulsed current to the LED so that it would emit faint enough light for the single-photon calibration. The duration of the calibration measurement was 10^3 seconds.

The pulse-height spectrum constructed from the calibration data was fitted by a model function

$$f(x) = A \times \left(\exp\left(-\frac{(x-\mu)^2}{2\sigma^2} \right) + B \times \exp\left(-\frac{x}{\ell} \right) \right) \tag{6.2}$$

with A, B, μ, σ, and ℓ as free parameters. Figure 6.5 plots the pulse-height spectrum together with a model function which fits the data. The x-axis indicates the pulse height and y-axis the number of counts in each bin. The best-fit values for the parameters are shown in Tab. 6.1.

We will use this function with the best fit values as the template in the analysis of HP CDM search.

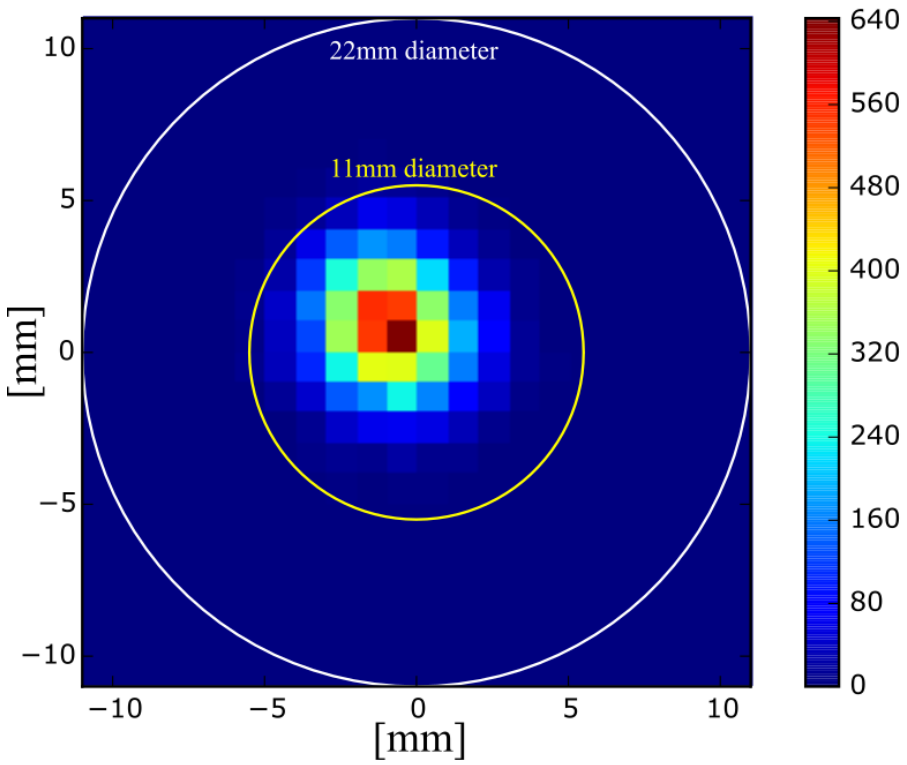

Figure 6.3: Density plot of the arrival position of photons in the focal plane.

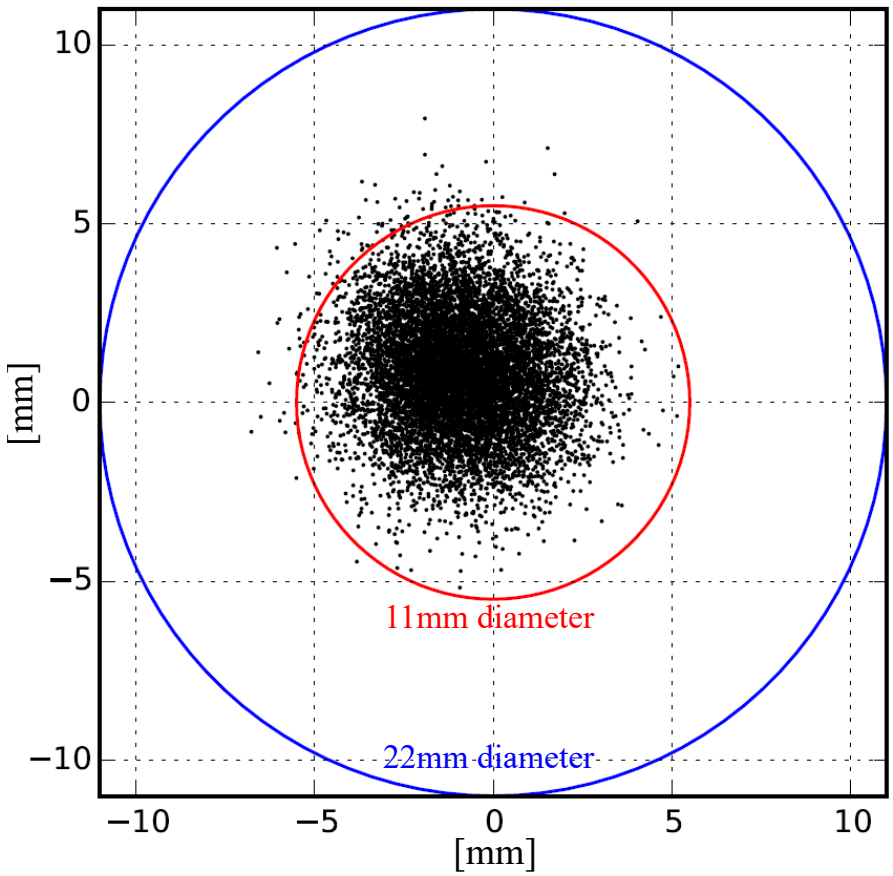

Figure 6.4: Scatter plot of the arrival position of photons in the focal plane.

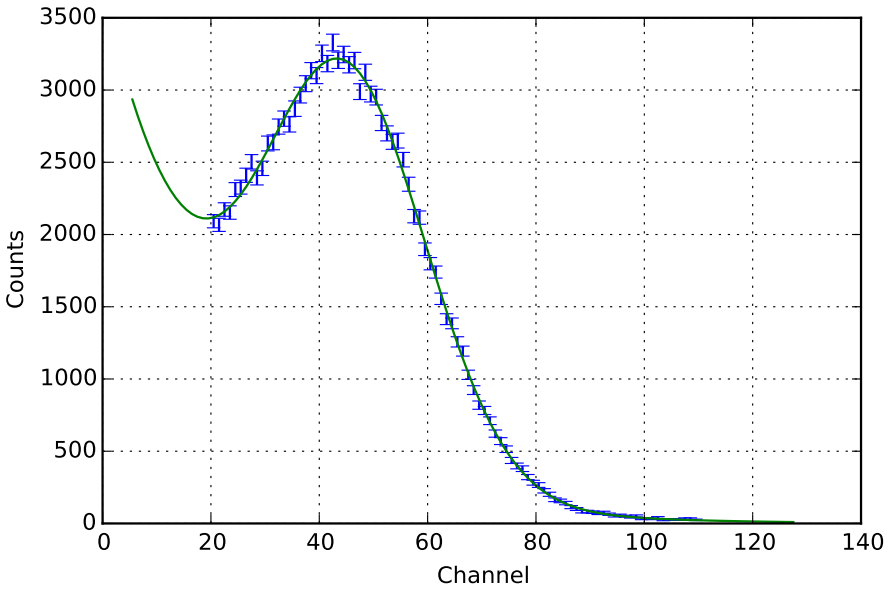

Figure 6.5: Pulse-height spectrum of the calibration data with the light source, and a model function which fits the data.

Parameters	Best-fit values
A	$(2.75 \pm 0.02) \times 10^3$
B	1.34 ± 0.06
μ	45.1 ± 0.2
σ	14.9 ± 0.1
ℓ	21.4 ± 0.3

Table 6.1: The best-fit values for the parameters of the pulse-height spectrum.

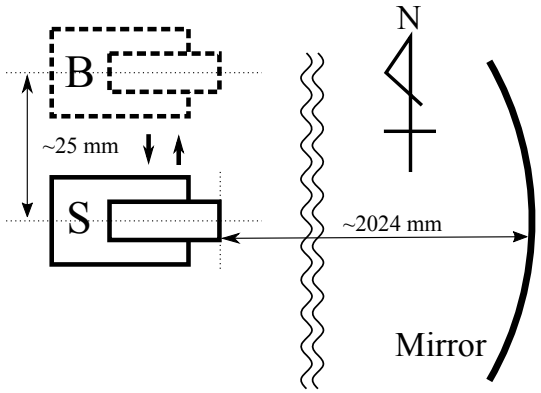

Figure 6.6: Schematic of the top view of the set-up.

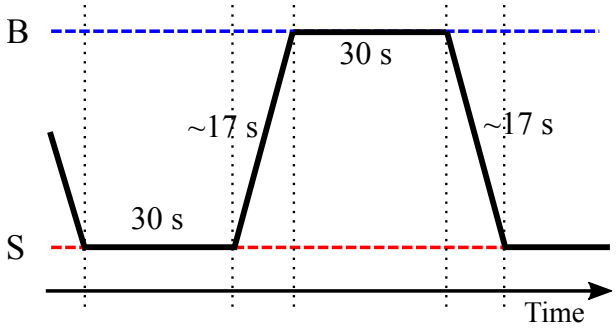

Figure 6.7: Diagram of the operation of the motorized stage.

6.2 Measurement

As described in the previous chapter, we used a motorized stage to switch between the measurement of HP signal and the measurement of background. The position of the background measurement (position B) was displaced from the position of the signal acquisition (position S) by 25 mm, which is large enough to let the light spot out of the effective area of the photomultiplier tube. The top view of the set-up is schematically drawn in Fig. 6.6.

The procedure of the operation of the motorized stage is depicted in Fig. 6.7: (i) halt the stage at position S for 30 seconds, (ii) shift the position of the PMT from S to B in $\sim$ 17 seconds, (iii) halt the stage at position B for 30 seconds, (iv) restore the position from B to S. Therefore, the duration of a cycle was $\sim$ 100 seconds.

The arrival of the stage to the positions S or B are detected by mechanical switches. The time when the stage started to move and stopped was recorded, and the log was later used to assign the single-photon events to each stage, as well as to derive the total duration of the measurement for each stage.

The data acquisition by the digital oscilloscope was conducted independent of the movement of the stage. A data file records the heights and the arrival times of pulses for 10^3 seconds, together with the time when the file start and end recording. A script file controls the acquisition loop and a series of numbered files were created.

After a long period of commissioning run reported in Appendix A, we finally carried out the experimental search for hidden photon CDM with the apparatus described so far. The data was recorded from February 2015 to March 2015. The overall duration of the measurement was 8×10^5 s for each stage.

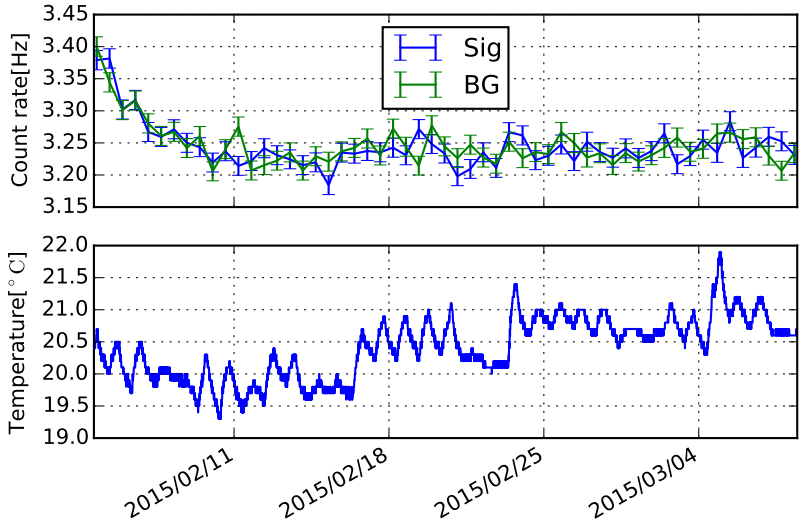

Figure 6.8: The time variation of the count rate of the photomultiplier and the temperature for a whole duration of the measurement.

We monitored the temperature near the photoelectric surface of the photomultiplier tube with a Pt100 platinum resistance thermometer read by a Temperature Data Logger TR-81 (T&D, Japan) with an interval of 1 minutes, which is later used to study the effect of temperature variation.

Figure 6.8 displays the time variation of the count rate of the photomultiplier and the temperature for a whole duration of the measurement. The upper panel shows the count rates[1] taken both at position S (blue solid line) and at position B (green solid line) with error bars. The bottom panel shows the temperature obtained by the resistance thermometer. The temperature variation was not so abrupt as we expected during a whole period of the run. The gradual decrease of the count rates at the beginning of the run was due to the effect described in Sec. 5.2.3.

We also show detailed views of the time variation of the count rate and the temperature in Fig. 6.9 - 6.13.

6.3 Analysis

In this section, we analyze the data obtained from the experimental run described in the previous section. We first treat the statistical aspects of the data, then discuss about possible systematics.

6.3.1 Statistics

Pulse-height spectra for the data taken both at position S and position B are constructed from the data files and the log of the motorized stage. Figure 6.14 is the pulse-height spectra for the data acquired at position S (red solid line) and at position

[1]The count rates here are calculated by summing up the number of events with pulse heights Channel 10 to 70, for a convenient measure.

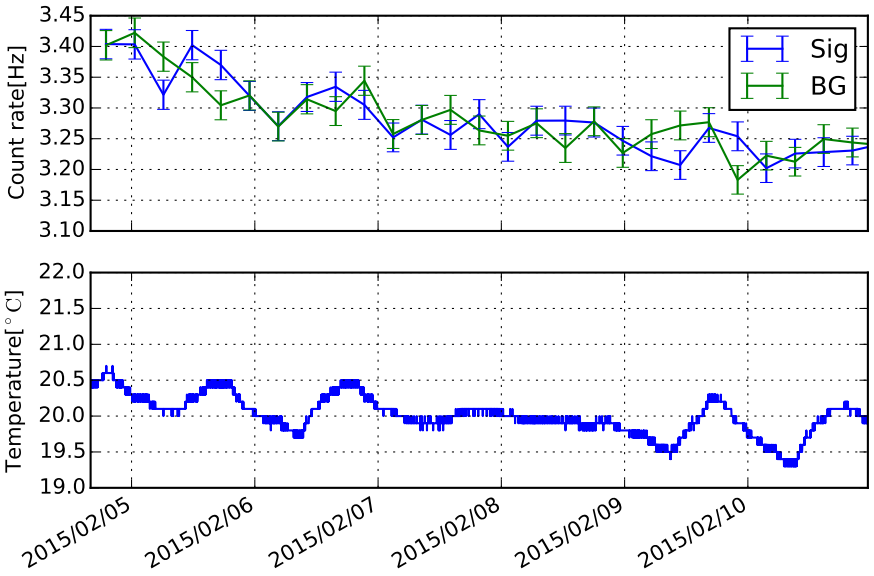

Figure 6.9: The time variation of the count rate of the photomultiplier and the temperature (from 2015/02/05 to 2015/02/11).

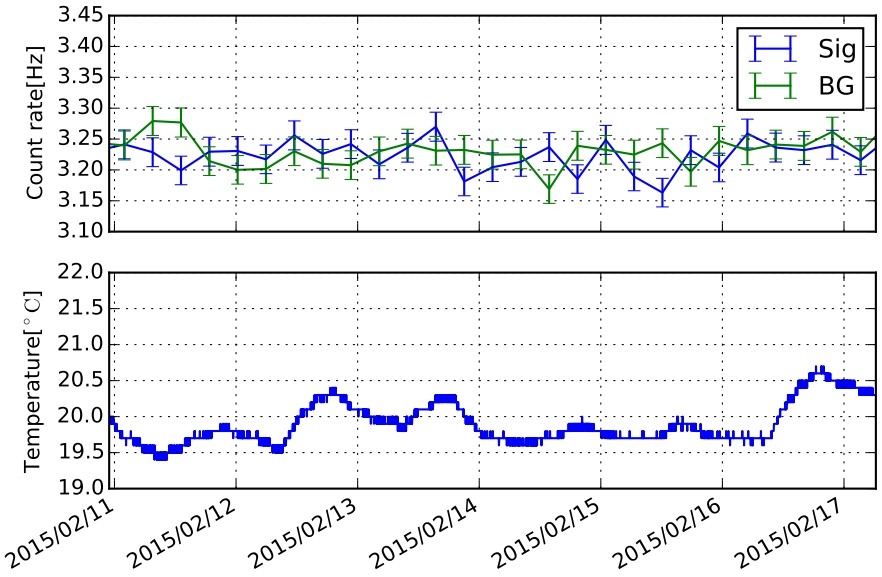

Figure 6.10: The time variation of the count rate of the photomultiplier and the temperature (from 2015/02/11 to 2015/02/17).

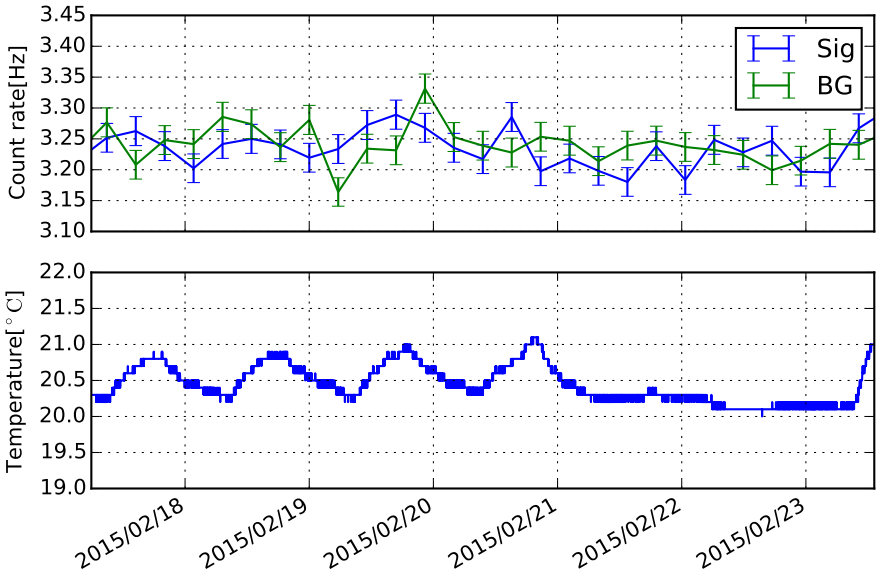

Figure 6.11: The time variation of the count rate of the photomultiplier and the temperature (from 2015/02/17 to 2015/02/24).

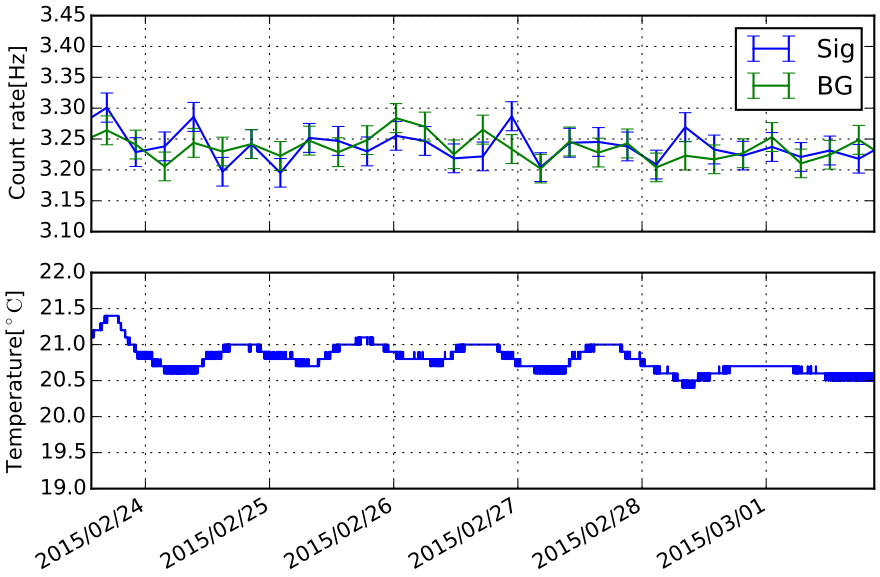

Figure 6.12: The time variation of the count rate of the photomultiplier and the temperature (from 2015/02/24 to 2015/03/02).

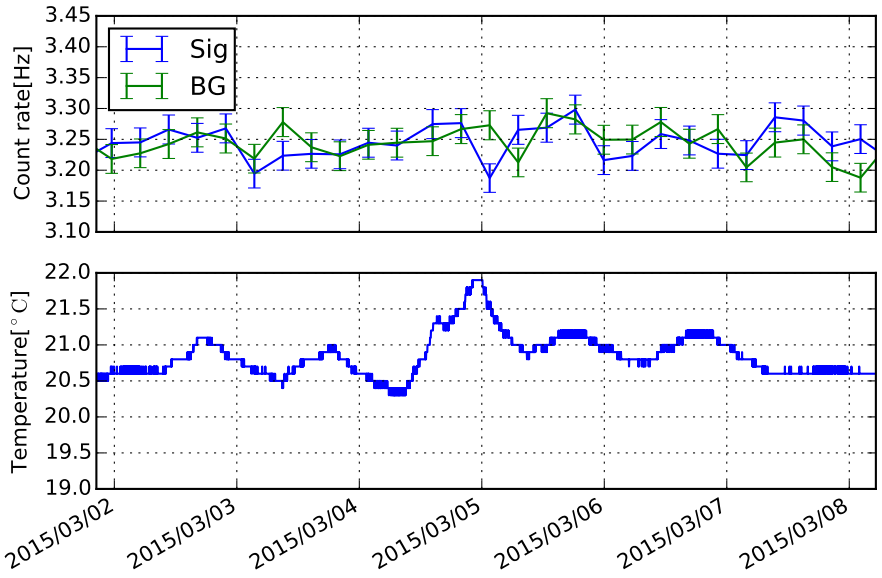

Figure 6.13: The time variation of the count rate of the photomultiplier and the temperature (from 2015/03/02 to 2015/03/08).

B (black solid line). The vertical axis shows the number of counts in a bin divided by the duration of the measurement, and the horizontal axis plots the pulse height.

In order to find out whether there is the excess of counts or not, we subtract the spectrum at position B from the spectrum at position S. Figure 6.15 is the result of the subtraction. We then fit the spectrum after the subtraction with the model function Eq (6.2) with A as a free parameter. As a result, we obtained the best-fit value of A as

$$A_{\rm fit} = (-2.9 \pm 5.8) \times 10^{-5}.$$

The best-fit curve is also shown in Fig. 6.15 as a green solid line. Integration of the model function yields

$$\int_0^\infty \left(\exp\left(-\frac{(x-\mu)^2}{2\sigma^2} \right) + B \times \exp\left(-\frac{x}{\ell} \right) \right) dx \simeq 65.34$$

with B, μ, σ, and ℓ substituted to the best-fit values shown in Tab. 6.1. The difference of the count rate between at S and at B is then estimated to be

$$N_{\rm fit} = A_{\rm fit} \times 65.34 = (-1.9 \pm 3.8) \times 10^{-3}\,{\rm Hz}. \tag{6.3}$$

6.3.2 Systematics

The main sources of systematic errors are

1. Temperature dependence of the dark count rate of the photomultiplier tube

2. Cherenkov emission caused by muons passing through the window of the photomultiplier tube

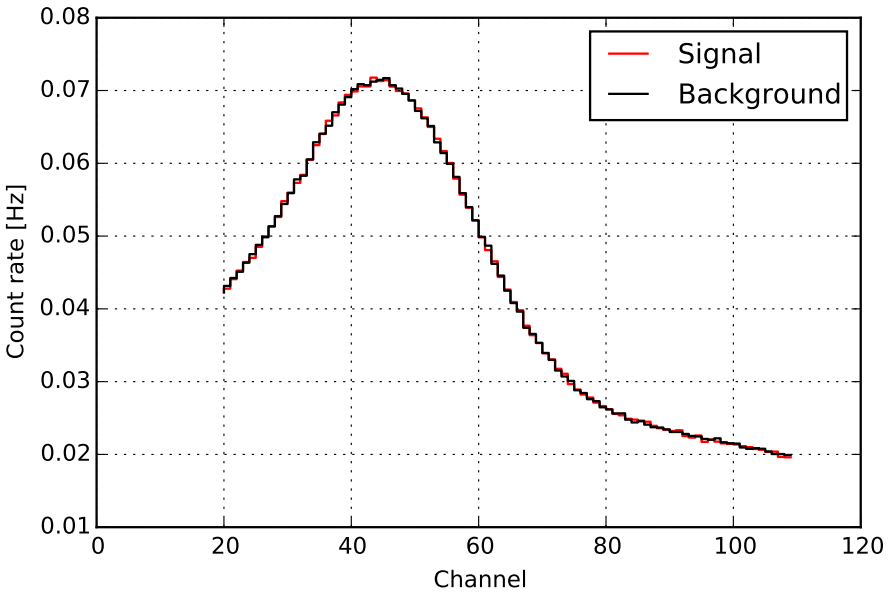

Figure 6.14: Pulse-height spectra for the data acquired at position S (red solid line) and at position B (black solid line). The vertical axis shows the number of counts in a bin divided by the duration of the measurement, and the horizontal axis plots the pulse height.

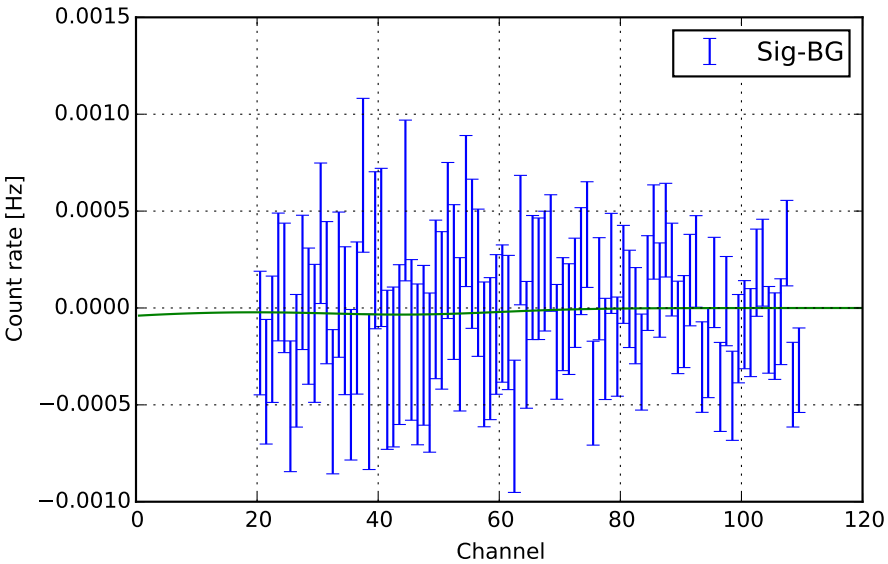

Figure 6.15: The result of the subtraction of the spectra (Sig - BG). The best-fit curve is also shown as a green solid line.

There are other minor sources such as temperature dependence of the high-voltage supply. Those effects are small compared to the temperature dependence of the dark count rate [21, 22], and also involved in the measurement of the temperature dependence of the dark count rate described in Sec. 5.2.3[2].

Temperature

The dark count rate of the photomultiplier tube depends on the temperature as explicitly shown in Fig. 5.14 with the coefficient of 0.21 Hz/°C. It could be a source of the systematic error. For example, if the temperature keeps rising during a whole period of the run with a rate of δ [°C/s], it would yield the difference in count rate between at position S and at position B as

$$\sim \delta \times \frac{100\,\mathrm{s}}{2} \times 0.21\,\mathrm{Hz/^\circ C} = 10.5\,\mathrm{Hz} \times \left(\frac{\delta}{^\circ\mathrm{C/s}}\right) = 2.9 \times 10^{-3}\,\mathrm{Hz} \times \left(\frac{\delta}{^\circ\mathrm{C/hour}}\right),$$

where 100 s is the period of the stage operation.

We monitored the temperature near the photoelectric surface of the photodetector as described in the previous section and as shown in Fig. 6.8 - 6.13. The most abrupt change in the temperature occurs on 2015/03/04 and the rate of the change is $<$ 1°C/3 hour. It thus might yield the systematic error as

$$\pm\frac{1}{2} \times 2.9 \times 10^{-3} \times \left(\frac{1}{3}\right)\,\mathrm{Hz} \sim \pm 0.5 \times 10^{-3}\,\mathrm{Hz},$$

which is found to be less important than the statistical error $\pm 3.8 \times 10^{-3}$ Hz.

Cherenkov emission

Cherenkov emission or other light emission originated from the photodetector might cause serious effects on the result of the search because of the optical arrangement of this experiment: position S locates near the point twice the focal length of the mirror and on the optical axis. Geometrical optics shows that emission towards the mirror from the point returns back to the same point. Emission from a photodetector at position S thus might returns to the photodetector itself then yield a count, while it does not occur for a photodetector at position B (Fig. 6.16).

As estimated in Appendix A, Cherenkov emission caused by atmospheric muons passing through the optical window of the photomultiplier tube might yield $\sim 10^{-2}$ Hz of single photoelectron events without limiting the effective area. This value is greater than statistical uncertainty if we carry out a run over a week.

To overcome this problem, we covered the effective area with a shield made of a sheet of black paper, and limit the area to 11 mm in diameter from 22 mm of the original as described in Appendix A. The validation of this treatment was argued in Sec. 6.1.1, where we concluded that the dispersion and the movement of the light spot caused by the velocity of dark matter is well within a circle of 11 mm diameter.

[2] In Fig. 5.14 in Sec. 5.2.3, fitting with a line goes very well though we considered only statistical errors for the error bars, which strongly supports that the origins of the systematic errors are limited to (i) the temperature dependence of the detector and the DAQ, or (ii) the optical set-up peculiar to this experiment.

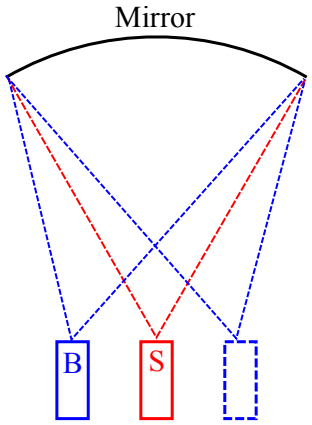

Figure 6.16: Schematic of the optical arrangement of position S and position B. Light emission towards the mirror from position S returns back to itself, while from position B goes to the contrary position.

The effect of the Cherenkov light to the final result is estimated to be less than 2×10^{-3} Hz in count rate after the treatment. This effect shifts count rate towards the positive direction, which might be subtracted from the value obtained in Eq. 6.3 if the estimation of the effect has sufficient accuracy. Instead we can choose not to subtract the effect from $N_{\rm fit}$, which results in conservative estimation of the upper limit to the count rate. Here we employ the latter choice.

Possible sources of acceptance degradation

In order to translate the result to the limit to the photon-HP mixing parameter χ, we have to evaluate the efficiency of signal acceptance. Following is the list of the factor to be considered:

- Quantum efficiency of the photodetector
  A typical value of the quantum efficiency of the R3550P is provided by the manufacturer and depicted in Fig 5.11[3]. Here we chose to use the typical response shown in Fig. 5.11.

- Collection efficiency of the photodetector
  Collection efficiency of the photomultiplier tube is known to be between 70% and 90% for head-on type detectors. Here we conservatively assume that the collection efficiency is 70% to translate the result.

- The efficiency of the mirror reflectance
  The reflectance curve is shown in Fig. 5.4, from which we observe that the reflectance exceeds 80% for the wavelength region of interest $300 - 650$ nm. We conservatively use 80% for the entire wavelength region to translate the result.

- Efficiency of photon accumulation by the mirror
  Photon accumulation efficiency can be degraded by the following factors.

[3]In general, the efficiency varies for each detector, though the absolute minimum is offered by inspections performed by the manufacturer. Scaling of the typical value according to this minimum does not degrade the sensitivity to χ significantly.

  - Accuracy of the shape of the mirror
    In Fig. 5.6, we confirmed that the parabolic surface of the mirror can efficiently accumulate photons emitted perpendicularly to the surface. We assumed an ideal parabolic surface there and discrepancy of the real surface from the ideal one can degrade the efficiency. However, from the focal diameter 1.5 mm from Tab. 5.1[4], we observe that broadening of the light spot from the inaccuracy of the shape is $\sim 1.5\,\mathrm{mm}/2 \sim 0.8\,\mathrm{mm}$, which is not problematic at all.
  - Inaccuracy of the alignment
    The simulation depicted in Fig. 6.3 and 6.4 takes the shift of the photodetector from the ideal position into consideration. Accuracy of the measurement of the shift does not affect the result at all.

- Data treatment
  We fit the data obtained by the subtraction (Sig - BG) with the model function Eq. 6.2, and then integrate the function with the best-fit value in the range $[0, \infty)$ to evaluate (6.3). The fit is carried out with the rage [20, 110] and the ratio $\int_0^{20} / \int_0^{\infty} < 0.3$ and $\int_{110}^{\infty} / \int_0^{\infty} < 0.002$, where $\int_A^B$ means integration of the model function between A and B. Although the integration between 0 and 20 seems to occupy a large portion, the difference between the real response and our assumption is small, which can be observed by comparing Fig 6.5 and Fig. 5.13, and would yield only a slight effect on the final result. In addition, the model function seems to be overestimated rather than be underestimated in the range [0, 20], which leads to a weaker upper limit. Our treatment therefore would be conservative.

6.4 Result

Combining N_{fit} obtained in Eq. (6.3) and the systematic error from the temperature dependence of the photodetector, we obtain

$$N = (-1.9 \pm 3.8\ (\mathrm{stat.}) \pm 0.5\ (\mathrm{sys.})) \times 10^{-3}\,\mathrm{Hz}$$

for the possible count rate of the signal of hidden photon CDM. It shows no significant evidence for the existence of hidden photon CDM, and we derive an upper limit for the count rate as

$$N_{\mathrm{UL95}} = 6.4 \times 10^{-3}\,\mathrm{Hz}$$

at 95 % confidence level. As we mentioned above, we do not subtract the effect of Cherenkov emission to derive the upper limit conservatively.

The sensitivity of the detector $R_{\gamma,\,\mathrm{det}}$ is related to N_{UL95} by

$$R_{\gamma,\,\mathrm{det}} = \frac{N_{\mathrm{UL95}}}{\eta_{\mathrm{PMT}}\eta_{\mathrm{mirror}}},$$

where η_{PMT} and η_{mirror} is the efficiency of the photomultiplier[5] and the reflectivity of the mirror. Figure 6.17 plots $R_{\gamma,\,\mathrm{det}}$ as a function of photon energy.

[4] The focal diameter of the mirror is measured by the manufacturer by supplying pseudo-parallel light.

[5] As described above, η_{PMT} is a multiplication of the quantum efficiency η_{QE} and the collection efficiency η_{CE}.

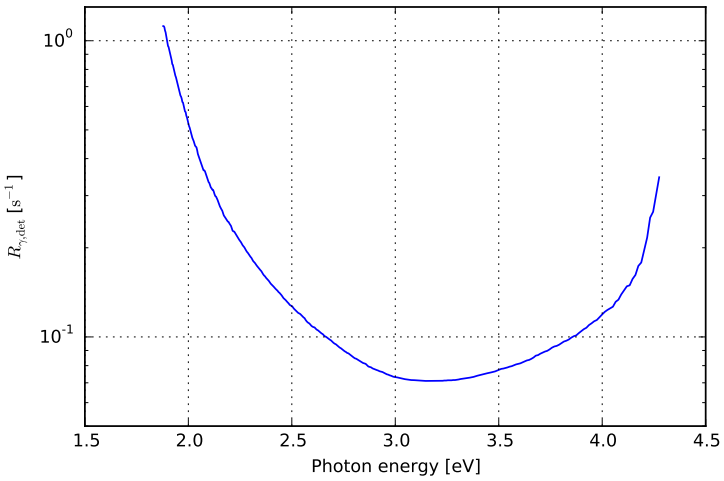

Figure 6.17: $R_{\gamma,\,\mathrm{det}}$ as a function of photon energy.

In order to translate this value to the limit to the photon-HP mixing parameter χ, we plug $R_{\gamma,\,\mathrm{det}}$ given above into Eq. 4.6, together with the area of the dish $A_{\mathrm{dish}} \sim 0.2\,\mathrm{m}^2$, $\alpha = \sqrt{2/3}$ supposing random direction of the HP vector, and $\rho = 0.4\,\mathrm{GeV/cm}^3$ according to the value given in Eq. 2.2.

Figure 6.18 shows the limit to the photon-HP mixing parameter χ obtained in this experiment. We excluded the red filled area around $m_{\gamma'} \sim$ eV. The region allowed for HPDM [25] is colored in light reddish brown, and the limit translated from the previous results for axion DM [25] is marked as "Haloscope" around $m_{\gamma'} \sim 10^{-5}\,\mathrm{eV}$. Other filled areas are excluded by other experiments or theoretical studies on astronomical objects. The regions excluded by experimental tests of Coulomb's law [32, 33], by "Light Shining through Walls" experiments [18, 34, 35, 36], by the CAST experiment [37, 38], by the search for hidden photon from the Sun [21], and by the FIRAS CMB spectrum [39] are marked as "Coulomb", "LWS", "CAST", "Tokyo" and "FIRAS", respectively. A constraint from the solar lifetime which takes only transverse mode into account [37, 38] is marked as "Solar lifetime", and a calculation which properly deals with longitudinal mode of the massive state [40, 41] is colored in light green.

We also show a detailed view of Fig. 6.18 in the region around the result of this experiment in Fig. 6.19.

Although the upper limit for χ obtained in this experiment is nominally weaker than the constraint from the solar lifetime, it is still significant because the calculation of the limit from the solar lifetime strongly depends on the solar modeling and calculation, in which severe discrepancy with the real situation may occur, as there was correction for the improper treatment for longitudinal mode of the massive state [40, 41]. On the other hand, our experimental limit only assumes that DM is mainly composed of hidden-sector photons.

This work also showed an example of detailed experimental method to search for HPDM with a dish antenna in the eV mass range. In spite of a lot of experiences we had accumulated in the search of solar hidden photons [21, 22], we encountered a variety of difficulties along the R&D process of this experiment as described in Appendix A. We will discuss some important points to be noted for future experiments using the 'dish' method in the next chapter.

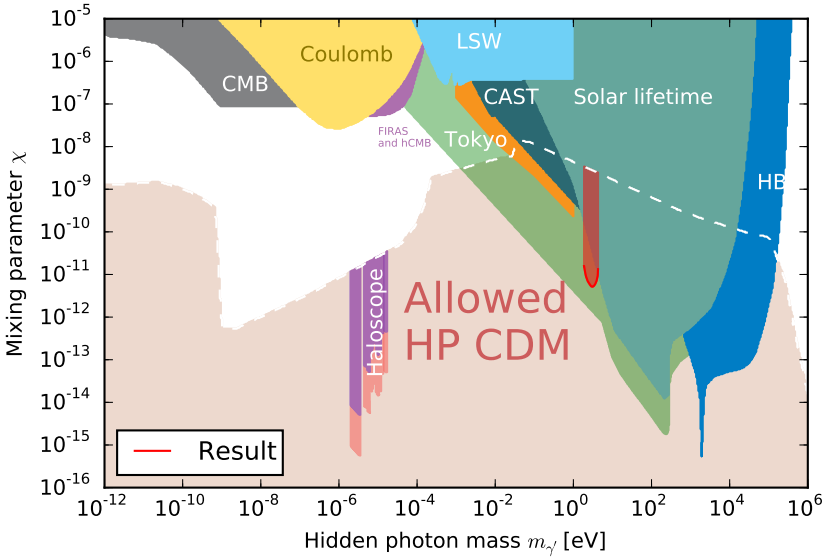

Figure 6.18: Excluded region of $\chi - m_{\gamma'}$ parameter space (red filled area around $m_{\gamma'} \sim$ eV). The region allowed for HPDM [25] is colored in light reddish brown, and the limit translated from the previous results for axion DM [25] is marked as "Haloscope" around $m_{\gamma'} \sim 10^{-5}$ eV. Other filled areas are excluded by other experiments apart from dark matter or theoretical studies on astronomical objects. The regions excluded by experimental tests of Coulomb's law [32, 33], by "Light Shining through Walls" experiments [18, 34, 35, 36], by the CAST experiment [37, 38], by the search for hidden photon from the Sun [21], and by the FIRAS CMB spectrum [39] are marked as "Coulomb", "LWS", "CAST", "Tokyo" and "FIRAS", respectively. A constraint from the solar lifetime which takes only transverse mode into account [37, 38] is marked as "Solar lifetime", and a calculation which properly deal with longitudinal mode of the massive state [40, 41] is colored in light green.

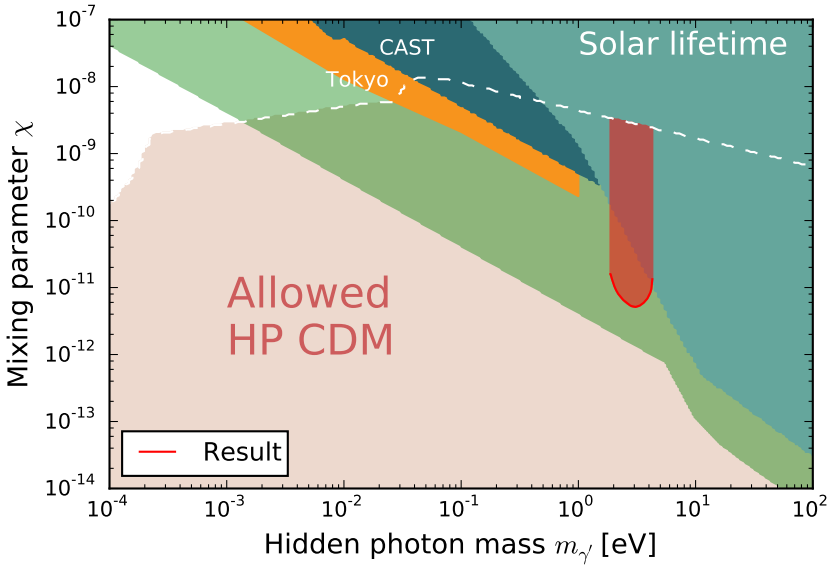

Figure 6.19: Detailed view of Fig. 6.18 in the region around the result of this experiment.

Chapter 7

Future prospects

So far we have described the experimental search for hidden photon CDM carried out for the first time using the 'dish' method. A lot of experiences and knowledge have been accumulated along the construction and the operation of the experimental apparatus, which would be helpful for succeeding experiments.

In this chapter, we shortly discuss requirements to attain higher sensitivity using the 'dish' method, and introduce planned experiments using 'dish'es.

7.1 Discussion for more sensitive searches

The experimental search for hidden photon CDM has just begun, and a vast area of the parameter space in $\chi - m_{\gamma'}$ plane has left to be investigated.

There are two main requirements for the search to be significant:

- Wide range of the hidden-photon mass $m_{\gamma'}$ can be investigated at the same time
- Substantial reach in the photon-HP mixing parameter χ is achieved

One of the benefits of the 'dish' method is its applicability to a wide range of wavelength without modifying the set-up. This is in contrast with searches using cavities, where the instruments should be properly re-arranged to search for other wavelengths out of a narrow temporary scope. In order to make use of this benefit, we have to use a detector which accept wide wavelength range. The photomultipler tube, which accepts over an octave of wavelength, is one of those wide-band detectors. For radio frequency, we might utilize spectrum analyzers which can deal with wavelength up to 30 GHz to search for the mass range of $m_{\gamma'} \sim 50 - 100\,\mu$eV.

As well as the energy range of detection, the sensitivity to the photon-HP mixing parameter χ is also important. The sensitivity to χ as a function of experimental parameters is given by

$$\begin{aligned} \chi_{\rm sens} \;<\; & 5.5\times10^{-13}\left(\frac{0.1}{\eta}\right)^{1/2}\left(\frac{\nu}{\rm Hz}\frac{100\,\rm day}{T}\right)^{1/4}\left(\frac{m_{\gamma'}}{\rm eV}\right)^{1/2} \\ & \times\left(\frac{0.3\,\rm GeV/cm^3}{\rho_{\rm CDM,\,halo}}\right)^{1/2}\left(\frac{1\,\rm m^2}{A_{\rm dish}}\right)^{1/2}\left(\frac{\sqrt{2/3}}{\alpha}\right)\ (95\%\,\rm CL), \end{aligned} \tag{7.1}$$

where η is the efficiency of the detector and the dish, ν the dark count rate, T the duration of the measurement, $A_{\rm dish}$ the area of the dish. We find that the sensitivity

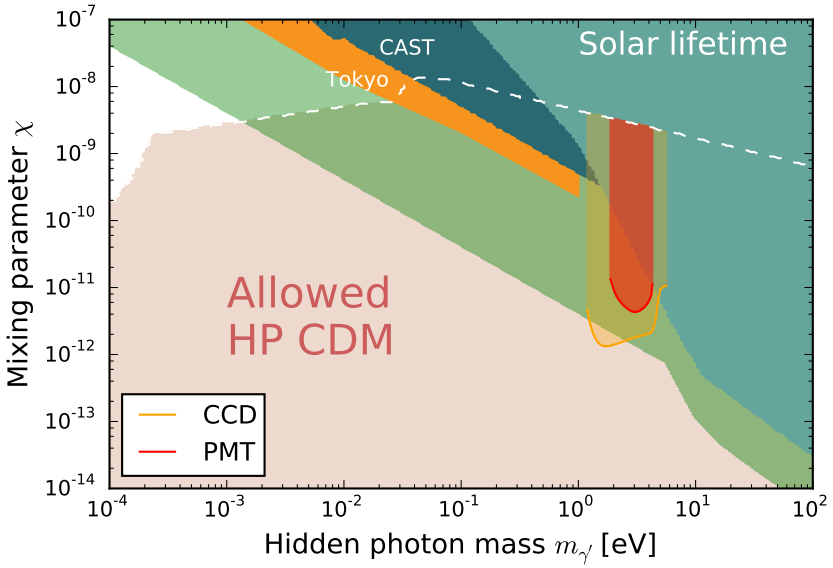

Figure 7.1: Plot of the experimental reach when we use a photomultiplier tube, and that if a CCD camera is in use.

to hidden photon CDM strongly depends on the efficiency η and the area of the mirror $A_{\rm dish}$ from this formula.

In Fig. 7.1, we compare experimental reaches obtained by using a photomultiplier and a CCD camera. We supposed the quantum efficiency of the SPEC-10 CCD camera (Princeton Instruments, the United States) for the CCD sensitivity calculation, while the other parameters are set the same. The quantum efficiency of a back-illuminated CCD reaches $\gtrsim 90\,\%$ and is spread widely over the wavelength range from near IR to near UV.

It must be noted that the assumption for a CCD camera might be a bit impractical, because it sets the dark counts of a CCD camera to the same value to the photomultiplier. CCD cameras cooled down to liquid nitrogen temperature have a low dark count rate comparable to photon-counting PMTs. However, readout of a CCD inevitably causes read-out noise, and it might surpass the dark noise. In order to reduce the read-out noise, some treatments listed below are required:

- Binning
  By combining pixels before reading out, we can reduce the read-out noise. Although this manipulation degrades the spatial resolution, we do not need high resolution because the light spot is broadened by the dispersion of the velocity of dark matter.

- Long exposure
  Exposure for a long time (even over an hour) reduces the effect of the read-out noise in comparison with the dark noise. However, time resolution in an exposure is completely lost, and the result would be degraded by atmospheric muons or other radiations.

In addition to the benefit from high quantum efficiency, the imaging ability of a CCD camera may be used to examine whether the signal is from HPDM or not: the light

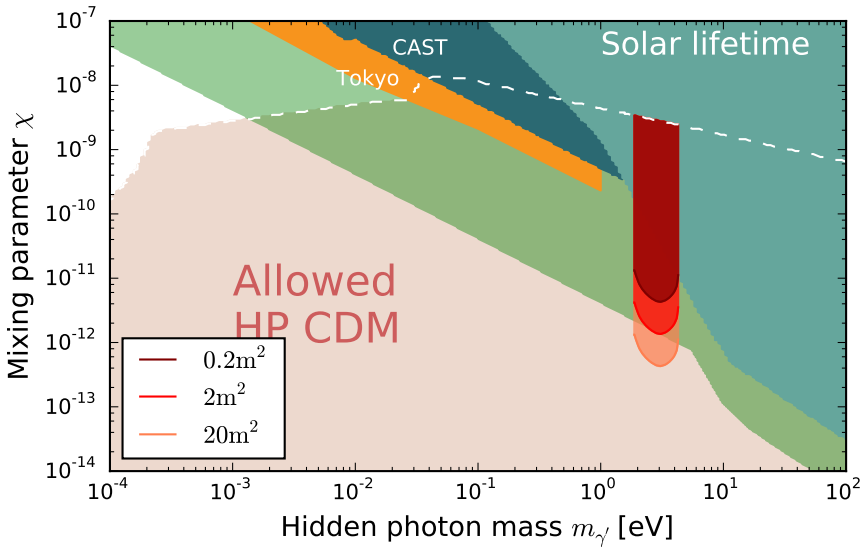

Figure 7.2: Dependency of the sensitivity on $A_{\rm mirror}$.

spot would move according to the rotation of the earth, and it could be used as a concrete evidence for dark matter signal as mentioned in Sec. 6.1.1.

Figure 7.2 shows dependency of the sensitivity on the area of the mirror $A_{\rm mirror}$. We plot three cases in which the mirrors are $0.2\,{\rm m}^2$ (current), $2\,{\rm m}^2$, and $20\,{\rm m}^2$. We will describe below the planned experiment which utilizes a mirror of $17\,{\rm m}^2$.

Scaling of the apparatus does not go well without close attention to things listed below.

First of all, shielding will be more and more difficult according to the size of the apparatus. In the experiment described in this thesis, we used two light-tight boxes both of which have rigid frames made out of slotted angle bars, and composed a two-fold environment. Under a room light, we expect light intensity of $\sim 100\,{\rm lx} \sim 100\,{\rm mW/m}^2$. Supposing the effective area of a photodetector to be $\sim 500\,{\rm mm}^2$, the energy flow would be

$$\begin{aligned} 100\,{\rm mW/m}^2 \times 500\,{\rm mm}^2 &= 5\times10^{-5}\,{\rm J/s} \sim 3\times10^{14}\,{\rm eV/s} \\ &\sim 10^{14}\,{\rm photons/s}\,, \end{aligned}$$

where we omitted factors of $\sim \mathcal{O}(1)$. We need to reduce this value down to $10^{-4}\,{\rm photons/s}$ to avoid its effect to the experimental result. Achieving 10^{-18} level of light shielding with a single shell would be very difficult. On the other hand, if we use a double shell, we need two light-tight boxes which can reduce light to 10^{-10} level, which seems to be a feasible solution. In general, it is very difficult to attain light-tightness of 10^{-18} level for boxes over $\sim$ m, and two-fold method might be inevitable.

The second problem comes from the velocity dispersion of dark matter. Velocity of dark matter v causes slight deviation of the emission angle from perpendicular by

$$vR \sim 1\,{\rm mm}\left(\frac{v}{10^{-3}c}\right)\left(\frac{R}{1\,{\rm m}}\right).$$

If the distance between the dish and the photodetector is $\sim 10\,{\rm m}$, we expect $\sim$ cm broadening for the light spot for an isothermal halo. Generally speaking, the dark

count of a photodetector with a large effective area is greater than that with a small effective area. We can use mirrors with high curvature to attain large A_{mirror} in spite of short distance between the detector and the mirror, but it might make the effect of Cherenkov emission even worse as described below. If we suppose other distribution for the velocity of dark matter with small dispersion, such as a caustic model [127] or a dark disk model [128], the deviation from this effect would be relaxed.

The third problem is about muonic Cherenkov emission. As we discussed in the previous chapter and will describe in Appendix A, muons passing through the window of a photodetector might cause serious effects on the measurement. The calculation shown in Appendix A tells that the counts caused by Cherenkov light is in proportion to the solid angle of the mirror from the photodetector. We thus conclude that using a mirror whose focal length is short compared to its diameter, i.e. with short radius of curvature, might be significantly affected by this effect. We can circumvent this problem by following treatments:

- Accurate estimation of the effect to subtract it from the value obtained in the measurement
  We could subtract the effect of the muonic Cherenkov from N_{fit}, which would result in lower $N_{95\mathrm{UL}}$ and the limit for χ, if we were able to estimate the effect in high enough accuracy. However, the accurate estimation of the effect seems to be very difficult and a lack in consideration for minor objects may cause severe discrepancy with the real situation.

- Construction of the apparatus in an underground site
  Going down to deep underground reduces the number of incoming muons, resulting in relaxation of the effect.

- Active shielding
  By surrounding the photodetector with scintillators, we can detect muons which might cause the counts in the photodetector.

Use of a photodetector without a window, e.g. CCD cameras, also would avoid the above effect.

7.2 Future plans

There are some experimental efforts to search for hidden photon CDM using the 'dish' method in the world.

The FUNK experiment [42] (an acronym for "Finding U(1)s of a Novel Kind") uses a large metallic mirror (Fig. 7.3), which is a heritage from the fluorescence-detector telescopes of the Pierre Auger Observatory [129], to search for hidden photon CDM in the optical region and maybe in radio frequency. Figure 7.4 shows a photograph of the mirror used in the FUNK experiment. The mirror is composed of 6×6 segments, each of which is 65 cm high and is 55 cm $-$ 65 cm width. The total area of the mirror is $14.56\,\mathrm{m}^2$, which is ~ 70 times larger than the mirror used in the experiment reported in this thesis.

They currently uses a CCD camera for the photodetector, and recently reported the result of preliminary measurements [42]. Figure 7.5 shows a comparison between the preliminary result of the FUNK experiment and the result of the experiment described

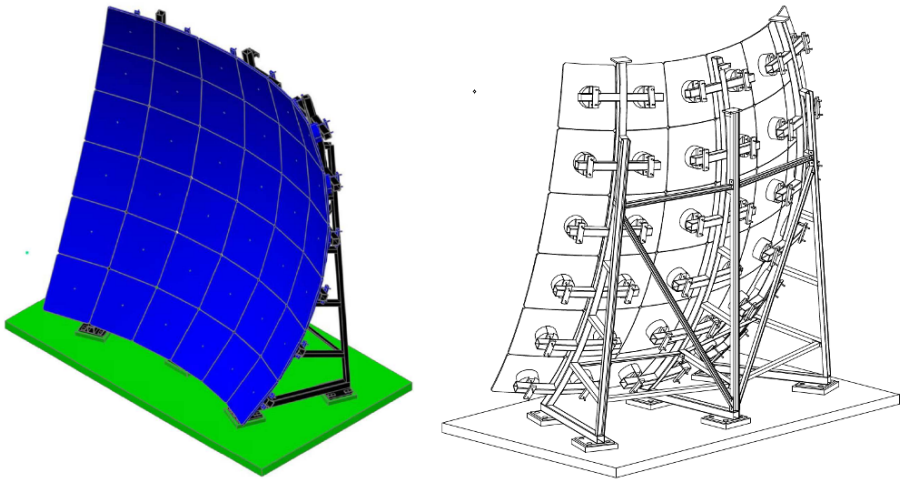

Figure 7.3: A large metallic mirror used in the fluorescence-detector telescopes of the Pierre Auger Observatory. Taken from Ref. [42].

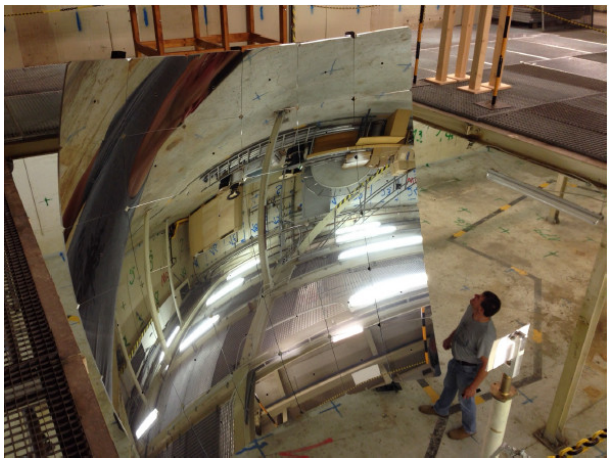

Figure 7.4: Photograph of the mirror used in the FUNK experiment.

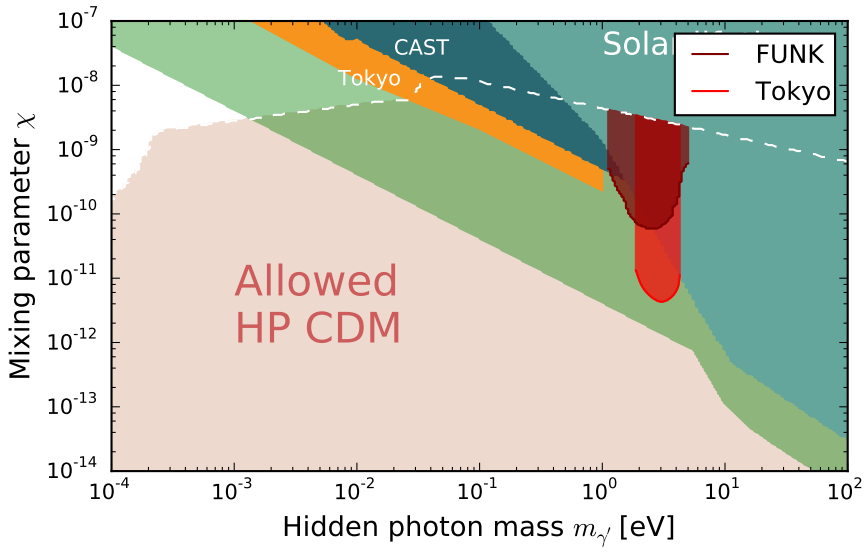

Figure 7.5: Comparison between the preliminary result of the FUNK experiment and the result of the experiment described in this thesis.

in this thesis. Although the mirror of the FUNK is by far larger than ours, the result is about 10 times worse. This limitation to the sensitivity comes from the performance of the detector, and they are planning to substitute it for a photomultiplier.

Translating the preliminary result of the FUNK experiment to the dark count equivalent using Eq. 7.1 yields

$$5\,\mathrm{Hz}\,(\text{our PMT}) \times (10\ (\text{times worse}))^4 \times \left(\frac{14\,\mathrm{m}^2}{0.2\,\mathrm{m}^2}\right)^2 = 2.5 \times 10^8\,\mathrm{Hz},$$

which is far from discussion about the light-tightness in the previous section. They might be suffered from light leaks or other problems along the R&D process to attain higher sensitivity. The experimental set-up and the treatments to achieve light-tightness used in the experiment reported in this thesis would be helpful for the FUNK experiment.

The experimental reach predicted for the FUNK experiment is shown in Fig. 7.6. The vertical axis shows the photon-HP mixing parameter χ in logarithmic scale, while the horizontal axis shows the mass of hidden photon $m_{\gamma'}$ in logarithmic scale. In addition to the search in the eV mass range with optical detectors, they are planning to survey in radio frequency, and the reach of the RF searches are also plotted in the figure.

Another group of Institute for Nuclear Research of Russian Academy of Sciences (INR) [44] is planning to use a multi-cathode counter to search of DM hidden photon with a mass $5\,\mathrm{eV} < m_{\gamma'} < 10\,\mathrm{eV}$. Hidden photon CDM around such a mass range is assumed to cause an effect like the photoelectric effect at the surface of a material, and would induce emission of an electron. A multi-cathode counter (shown in Fig. 7.7) picks up such electrons from a cylindrical cathode made of copper. In this experiment, the amplification of the signal due to a spherical surface is not used, though the signal electron would be emitted from a 'mirror' of the outer cathode.

The INR group is now studying the characteristics of the detector, and working for

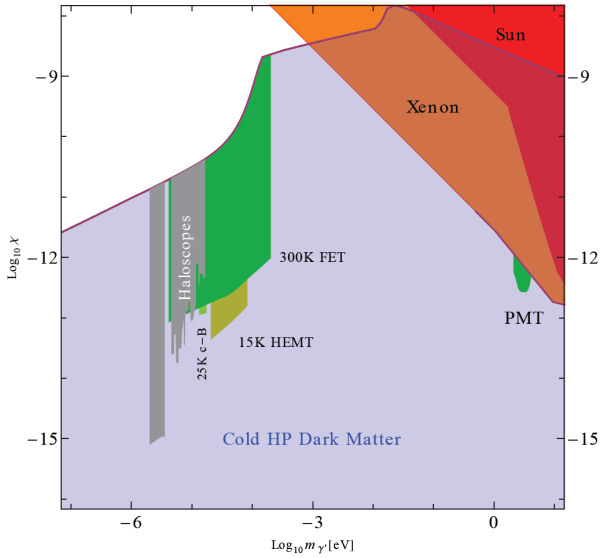

Figure 7.6: Experimental reach of the FUNK experiment. The vertical axis shows the photon-HP mixing parameter χ in logarithmic scale, while the horizontal axis shows the mass of hidden photon $m_{\gamma'}$ in logarithmic scale. The FUNK experiment plans to search in the RF region (labeled "15K HEMT" and "300K FET") in addition to the optical region (labeled "PMT"). Taken from Ref. [43].

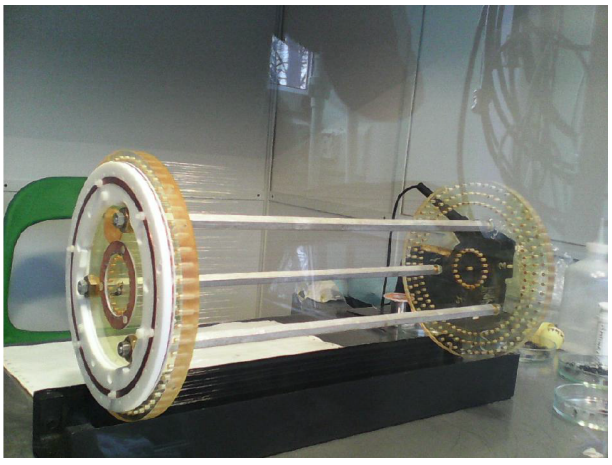

Figure 7.7: Photograph of the multi-cathode counter used by the group of Russian Academy of Sciences. Taken from Ref. [44].

the refinement of the procedure of data treatment. Although its sensitivity to hidden photon CDM is limited for the current status, it might explore the mass region which cannot be reached by optical 'dish' experiments.

Chapter 8

Conclusion

The experimental search for hidden photon CDM in the eV-mass region was performed for the first time using a novel technique with a concave mirror. DM hidden photon stimulates emission of ordinary photons perpendicular to the surface of a reflector. A concave mirror therefore accumulate the emission to its center of curvature. We utilized a mirror (500 mm diameter, radius of curvature ~ 2 m) and a photomultiplier tube (Hamamatsu R3550P) to search for the signal of hidden photon CDM origin.

No excess of count rate was observed, and we set an upper limit on the photon-HP mixing parameter χ of $\chi \sim 7 \times 10^{-12}$ for the hidden photon mass $m_{\gamma'}$ between 1.9 eV and 4.3 eV (Fig. 8.1). Although the upper limit for χ in Fig. 8.1 is nominally weaker than the constraint from the solar lifetime (green-filled area), it is still significant because the calculation of the limit from the solar lifetime strongly depends on the solar modeling and calculation, in which severe discrepancy with the real situation may occur, as there was correction for the improper treatment for longitudinal mode of the massive state [40, 41]. On the other hand, our experimental limit only assumes that DM is mainly composed of hidden-sector photons. In addition, the sensitivity of this experiment surpasses that of the preliminary run of the FUNK experiment with a 70 times larger mirror, which definitely proves the superiority of our methodology. We thus believe that detailed description on the experiment in this thesis will be helpful for the next generation of 'dish' experiments.

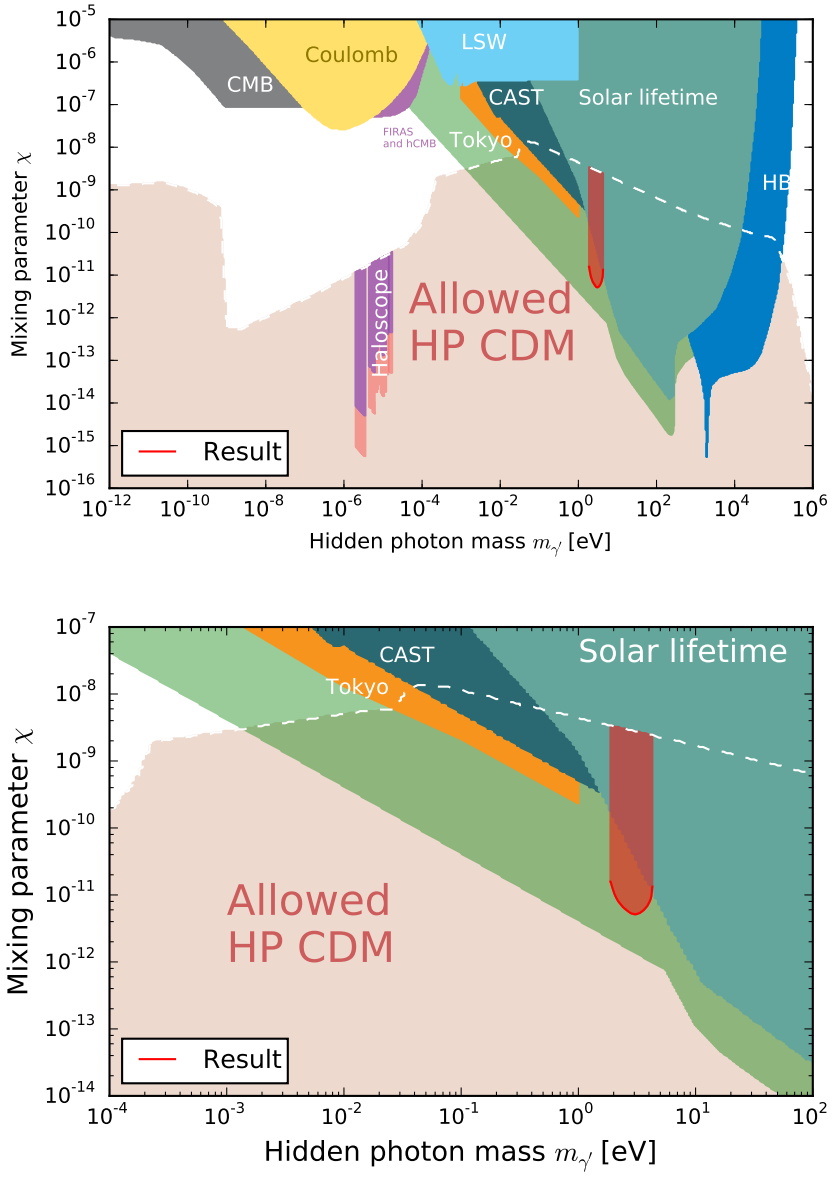

Figure 8.1: Excluded region of $\chi - m_{\gamma'}$ parameter space (red filled area around $m_{\gamma'} \sim$ eV, cf. Fig. 6.19).

Acknowledgment

First, I would like to express my gratitude to Prof. M. Minowa for his advices for the experiment and supports over a wide range of subjects.

I am sincerely grateful to Y. Inoue for his assistance. His broad knowledge and deep insight on physics greatly enhanced the quality of this work.

I would like to thank other members of Minowa group. The construction of the apparatus for this experiment was greatly supported by Dr. T. Horie. I have spent a lot of time with Dr. R. Ohta, Dr. S. Oguri, Dr. Y. Kuroda, Dr. Y. Kato, and N. Tomita in the laboratory, and discussion with them enlighten me in a variety of manner.

Although the axion helioscope Sumico is not directly connected to this work, it supports my work of the master thesis, and opens up a direction towards WISP searches of Minowa group. I appreciate all members concerned to the construction of the Sumico helioscope, including Prof. S. Moriyama, Dr. T. Namba, Y. Takasu and Prof. A. Yamamoto.

This research is partially supported by the Grant-in-Aid for Challenging Exploratory Research by MEXT, Japan, Research Center for the Early Universe, School of Science, the University of Tokyo, and Advanced Leading Graduate Course for Photon Science (ALPS) at the University of Tokyo.

Appendix A

Experimental difficulties and efforts for the improvement

As we can see in Chap. 6, the statistical error if we use a photomultiplier R3550P is expected to be

$$\sim 3 \times 10^{-3}\,\mathrm{Hz}$$

with a duration of the measurement for $\sim$ month. We thus conclude that a single irregular count in 10^3 sec might cause a serious effect on the result. Precision measurements of this sort have little experience, and unexpected systematics might occur in various ways.

In this appendix, we list difficulties with which we were confronted in commissioning runs, and treatments to overcome those problems, which might be helpful for experiments of the next generation.

A.1 DAQ: inaccuracy in the time measurement

In Sec. 3.2.2, we described the experimental search for solar hidden photons using a vacuum chamber mounted on the Sumico axion helioscope. We inherited the photodetector and the data acquisition system used in the search, later modified to overcome a problem described below.

Figure A.1 shows a schematic diagram of the old data aquisition system. The output of the photomultiplier is connected to a charge-sensitive preamplifier (ORTEC 113) followed by a shaper (ORTEC 572), and a Wilkinson-type ADC (2201A, Laboratory Equipment Corp., Japan), which works in coordination with a dedicated multichannel analyzer (MCA/PC98, Laboratory Equipment Corp., Japan).

The multichannel analyzer is controlled by a Windows PC via a dedicated software, from which settings, including the duration of a measurement, are sent to the MCA. The end of a measurement is governed by the MCA, having a programmable interval timer inside it. Measurement was performed as the following procedure: (i) move the stage to position S, (ii) take the data for 30 seconds, (iii) move the stage to position B, (iv) take the data for 30 seconds (v) return to (i). The dedicated program to control the MCA has a simple automation system ("job-control script"), which allows forming a loop and executing external programs in addition to acquiring data for a given period. The above procedure was realized by the job-control script, in which we execute the program to drive the motorized stage described in Sec. 5.2.5.

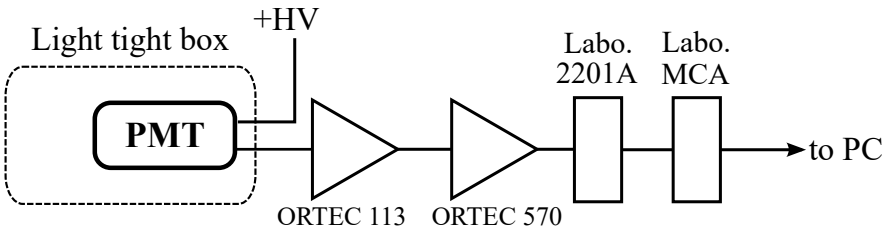

Figure A.1: Schematic diagram of the DAQ originally used in the experiment in Ref. [21].

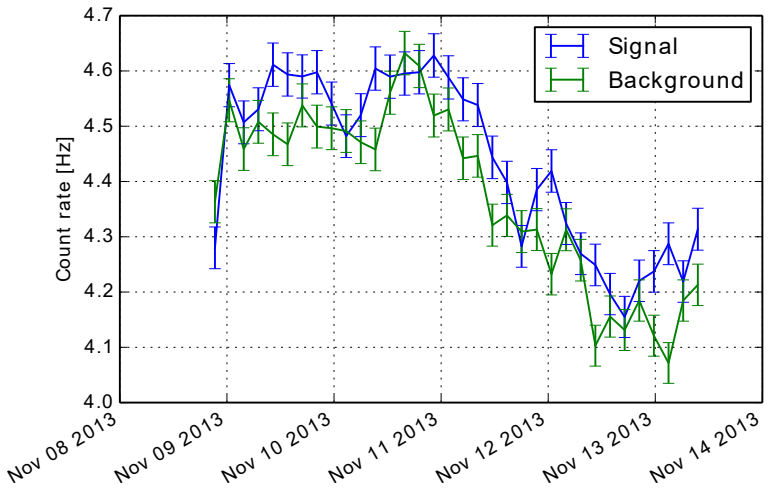

Figure A.2: Count rates taken at the signal taking position ('Signal') and the background taking position ('Background') in time series.

After the construction of the apparatus as described in Chap. 5, we carried out the first test run in November 2013, where we find significant excess in the count rate taken at position S within a day of the data acquisition. Figure A.2 shows the count rates taken at the signal taking position ('Signal') and the background taking position ('Background') in time series. The figure explicitly shows the excess of the 'Signal' rate over the 'Background' rate.

In order to figure out whether it was the actual signal or not, we carried out another run with modification to the procedure as follows. We decided to acquire background data at two different positions and to operate the motorized stage as depicted in Fig. A.3. The positions of background taking are named 'B_A' and 'B_B', and, furthermore, 'B_A' is distinguished according to whether it comes from position S ('B_AR') or from position B_B ('B_AL').

The second run was done in November 2013, and obtained the result shown in Fig. A.4. The accumulated count rates at positions S, B_AR, B_B, and B_AL are compared in the left panel. The count rates in time series are shown in the right panel. We conclude from the result that (i) the positive signal obtained in the previous run would be fake, and (ii) the error is not caused by the difference in the numbers of incoming photons depending on the positions, because the rates of B_AR and B_AL, both acquired at the same position, contradict each other with high confidence.

We doubt the data acquisition system, and performed the third run in which the motorized stage was not moved at all and we instead just halt the measurement for

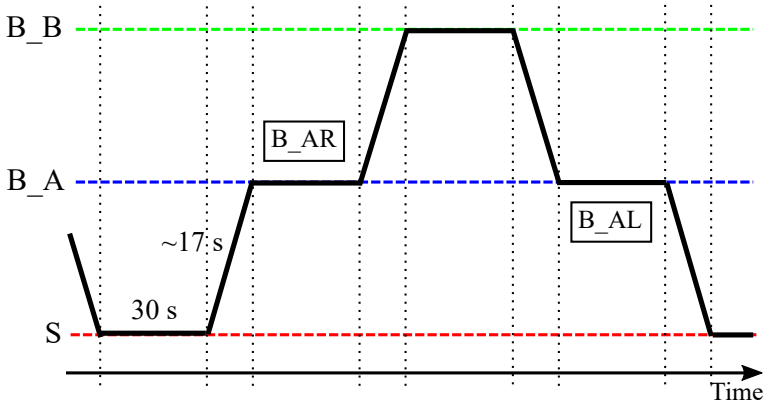

Figure A.3: Diagram of the operation of the motorized stage in the second run.

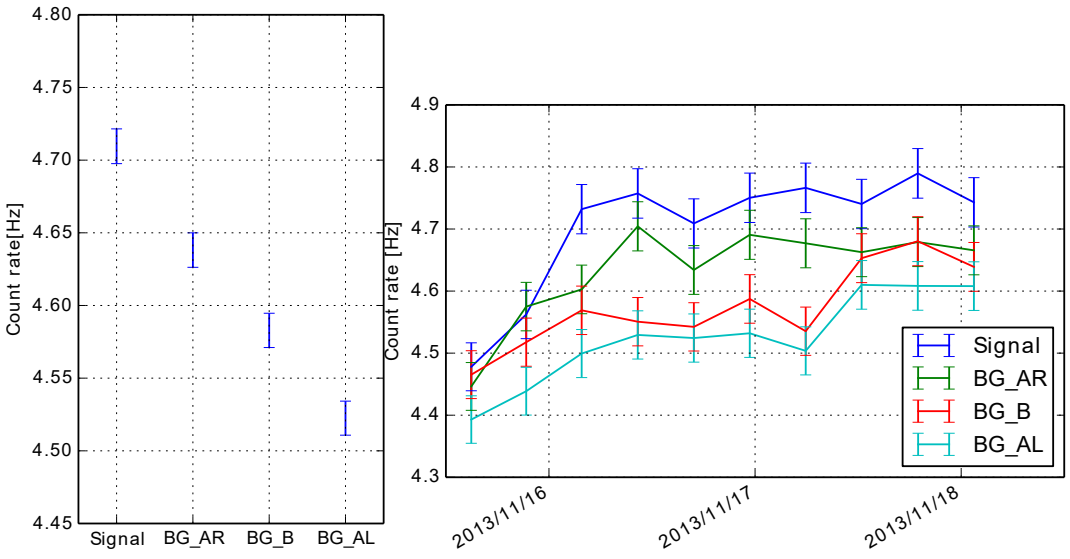

Figure A.4: Result of the second run. (Left) Accumulated count rates acquired at position S, B_AR, B_B, and B_AL. (Right) Count rates in time series.

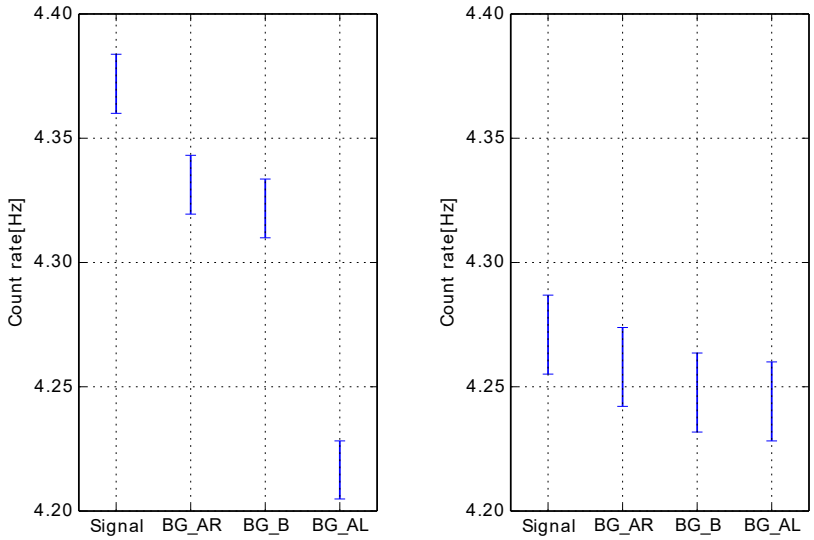

Figure A.5: Results of the third run. (Left) Result of the run in which the data was acquired for 30 seconds for each state, and the program driving the motorized stage was substituted to a just-waiting program in the job-control script. The labels 'Signal' etc. thus do not represent the position of the stage. (Right) result of the run with the same set-up except for the modification of the acquisition period from 30 seconds to 120 seconds.

the same period ~ 17 sec required to move the stage to the next state. We substituted the program driving the motorized stage to a just-waiting program in the job-control script described above.

The result is shown in the left panel of Fig. A.5, which gives a strong evidence for an unexpected error in the DAQ. The right panel of Fig. A.5 is the result of the run with the same set-up except for the change of the period of data acquisition at each state from 30 seconds to 120 seconds, in which we find that the error is moderated. We thus infer that the error was caused by the inaccuracy in the time measurement of the MCA, which would be moderated as we lengthen the period of the measurement.

We circumvented this problem by modifying the data acquisition system. The ADC and the MCA were removed and, instead, a digital oscilloscope was introduced (cf. Sec. 5.3).

A.2 Problem in the motorized stage and peculiar differences in the count rates

After the renewal of the data-acquisition system, we carried out a lot of test runs, all of which were in vain because of a fault in the operation of the motorized stage. The motorized stage was controlled from a PC and migration lengths were encoded in the number of steps to drive the stepper motor. Because the motorized stage was enclosed in the light-tight box and cannot be seen for a whole period of measurements, we installed a mechanical switch to calibrate the position of the stage. The motorized stage was operated as in the left panel of Fig. A.6, which was proved to result in failure. In the operation, the stage moves back and forth between position S and position B for 100 times, then go to the mechanical switch to confirm the position. The right panel

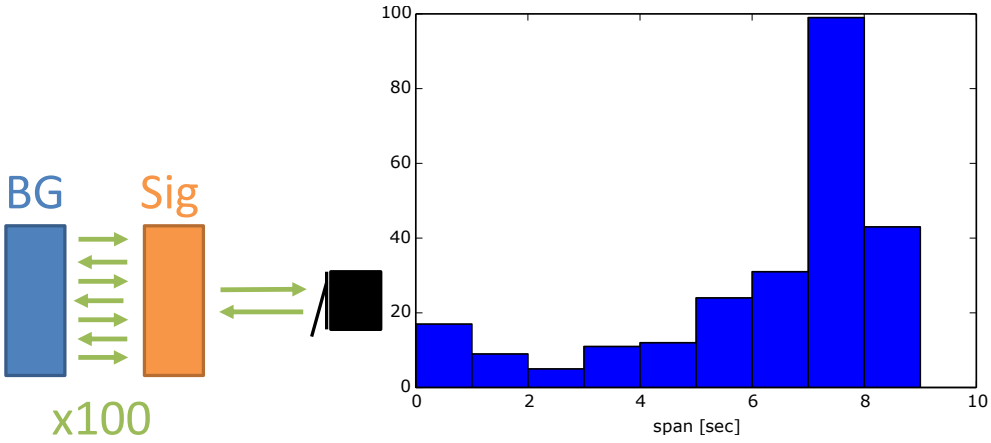

Figure A.6: Fault in the operation of the motorized stage. (Left) Schematic of the operation of the stage which causes the failure. (Right) Histogram of the times required to get to the limit switch from the signal-taking position.

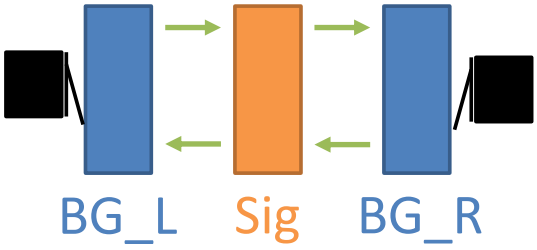

Figure A.7: Operation of the motorized stage after the 5th run. The background measurements are done both right (BG_R) and left (BG_L) of position S, and the limit switches are placed to ring when the stage reached to position BG_L and position BG_R.

of Fig. A.6 shows a histogram of the times required to get to the limit switch from the signal-taking position. The broadening of the histogram suggests that the errors in the position had been accumulated during the repeats (Sig↔BG) of 100 times.

We therefore change the operation not to repeat (BG↔Sig)-transitions for 100 times but to return to the limit switch every time the stage return to position S. After the change of the operation, we carried out a test run ('Run 4'), which yields difference in the rates at position S and at position B of $\sim 10^{-2}$ Hz.

In order to figure out the cause of this difference, we again performed a run which measures background data at two different position, similarly to the second run, but this time the positions of background measurement were placed both left and right of position S (Fig. A.7). The diagram of the operation was similar to that of the second run (cf. Fig. A.3), except that in this case position S can be distinguished by the direction of arrival (We name two cases 'Sig_R' and 'Sig_L' in a similar manner).

The result of the fifth run is shown in Fig. A.8. The left panel is accumulated the count rates at each position, while the right panel shows the count rates in time series. Because the rate at position BG_R surpasses that of at position S, we conclude that the difference in the previous run would not be the actual signal of hidden photons.

In the next run (6th run), we introduced a platform with which the photodetector was kept away from the stepper motor (Fig. A.9). We suspected that the difference is caused by heat flow from the stepper motor, which would be diminished by placing

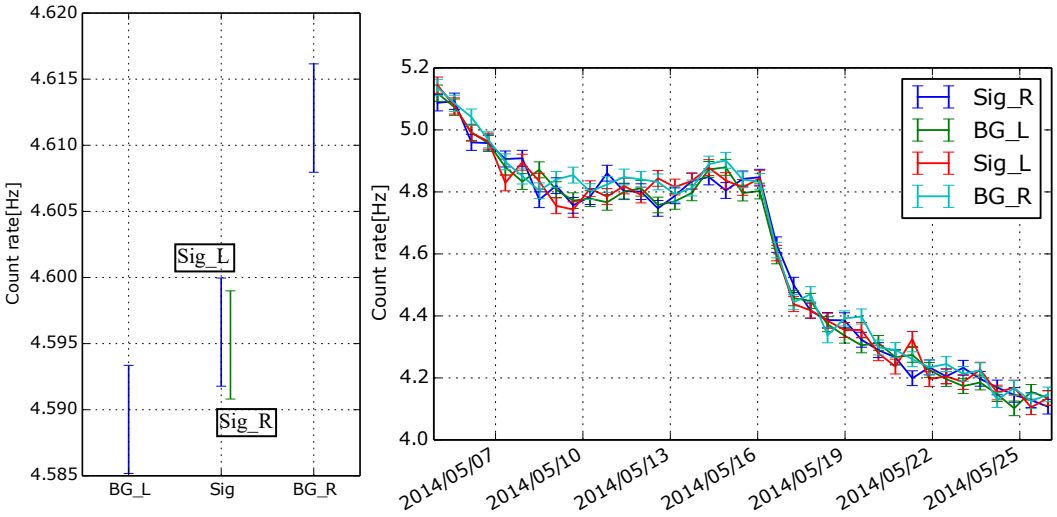

Figure A.8: Result of the fifth run where the stage was operated as in Fig. A.7. (Left) Accumulated count rates at each position. (Right) Count rates shown in time series

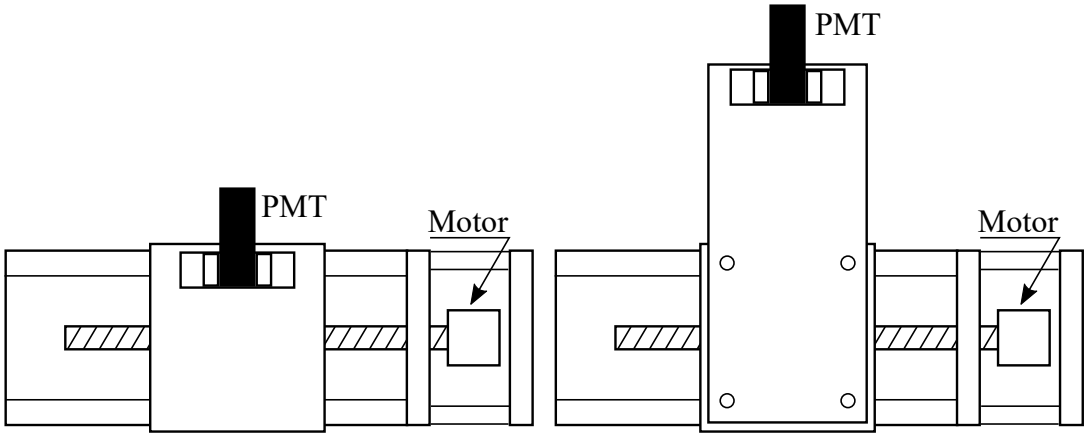

Figure A.9: Schematic of the platform to place the photodetector away from the motor. (Left) The motorized stage and the detector in the original set-up. (Right) The motorized stage with the platform on the end of which the photodetector is placed.

the photomultiplier tube away from the motor. However, the difference did not vanish in the result of the 6th run.

We placed the preamplifier on the stage in the succeeding run (7th run), worrying about the change in stray capacitance of the cable connecting the detector and the preamplifier caused by the movement of the configuration. It also did not reduce the peculiar differences.

In order to isolate the cause of the difference, we capped the window of the photodetector, and performed otherwise same measurement (8th run). The result is shown in Fig. A.10 with no significant difference, from which we conclude that the difference is caused by photons entering to the photodetector.

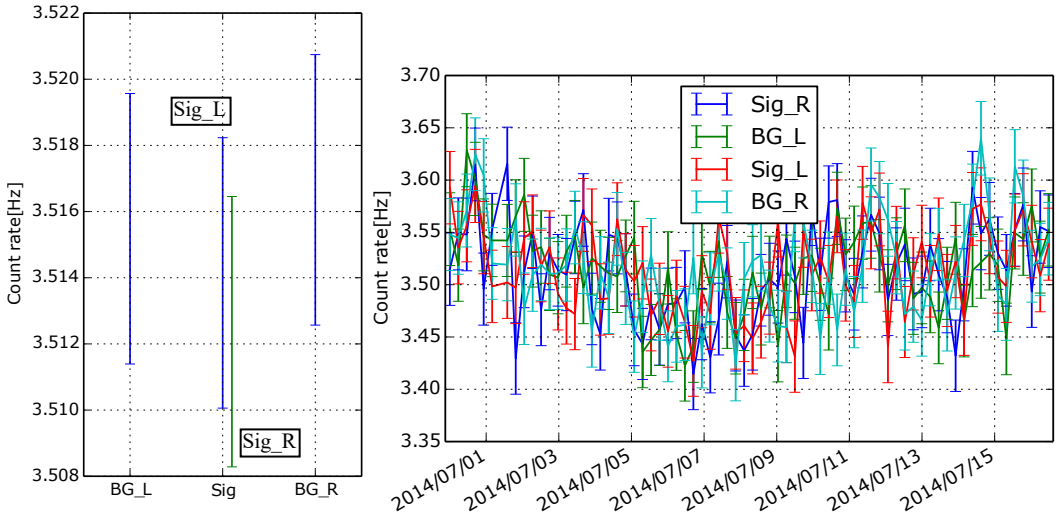

Figure A.10: Result of the 8th run where the window of the photodetector was capped to make it blind to visible light in order to figure out whether the difference is caused by photons or not. (Left) Accumulated count rates at each position. (Right) Count rates shown in time series.

A.3 Reduction of photons from materials around the detector, and self-emission caused by muons

It is empirically known that a lot of materials emit photons. The intensity of the emission is so faint that it would escape from detection without a sensitivity of $\sim 10^{-2}$ counts/s. In fact, we chose to use a motorized stage rather than a shutter to measure the background rate in order to avoid effects from those emissions: landscapes from the detector do not dramatically change with a slight shift of the position. However, sight around the detector might change considerably, which would cause the change in the count rate depending on position.

To reduce the effect from photons emitted by materials around the detector, we introduced a hood to limit the sight from the detector, and performed a measurement as the previous runs. The result is shown in Fig. A.11. Although the significance is not over 2σ, we suspected further sources of the difference.

As already shown in Fig. 6.16, light emission towards the mirror from a photodetector at position S returns back to itself, while from position B goes to the contrary position. The source of self-emission of the photomultiplier tube might be caused by

- Residual gas inside the tube
  It is known that residual gas inside the phototube cause unwanted effects, and might emit photons with high voltage applied.

- Cherenkov emission of muons
  Atmospheric muons passing through the window of the photodetector would induce Cherenkov light

Although the emission from the residual gas cannot be determined easily, we can roughly estimate the effect of the Cherenkov emission by hand as follows.

- Muon flux
  It is known that the flux of muons at the ground level is about ~ 1 coutns/cm^2/min.

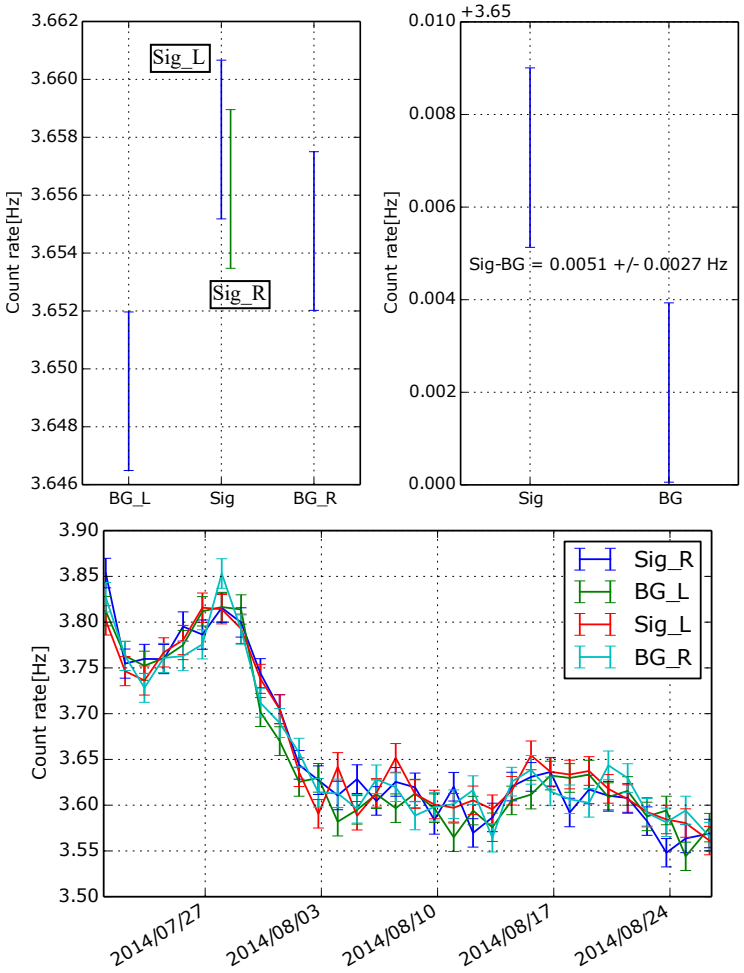

Figure A.11: Result of the 9th run where the hood was installed to limit the sight from the detector. (Upper left) Accumulated count rates at each position. (Upper right) Data acquired at signal(background)-taking position Sig_L and Sig_R (BG_L and BG_R) are put together to yield a rate labelled 'Sig' ('Background'). (Bottom) Count rates shown in time series.

The effective area of the PMT is $S = \pi \times (11\,\mathrm{mm})^2$. Multiplying these values yields ~ 0.1 hits/sec. This value is over estimated because the angle distribution of cosmic muons tells that flux in horizontal direction is fewer than in vertical direction.

- Probability that emitted Cherenkov photons to go into the mirror
  The angular diameter of the mirror (seen from the PMT) is 14°. Thus, the probability that emitted Cherenkov photons go into the mirror would be

$$\frac{\pi \times (7^\circ)^2}{4\pi} \sim 4 \times 10^{-3},$$

- Number of photons produced in the Cherenkov radiation
  Assuming that the thickness of the PMT window is $\sim 2\,\mathrm{mm}$, muons passing thorough the glass yields $\sim 10^2$ photons.

Multiplying those three values with the quantum efficiency of the PMT yields ~ 0.01 counts/sec. We thus find that it might cause a serious effect on the result (although the calculation is rough and the value may be overestimated).

By limiting the effective area of the PMT to 1/4, the increase in count rate (induced by cosmic muons) would be $0.01\,\mathrm{counts/sec} \times (1/4) \sim 2 \times 10^{-3}\,\mathrm{counts/sec}$, which is tolerable for measurements for $\sim$ month (cf. the statistic error in the 9th run).

We then performed the 10th run with limiting the effective area of the photomultiplier tube to 1/4 by a sheet of black paper. The result is shown in Fig. A.12, in which the difference (Sig-BG) seems to be absent. We also see that the count rates measured at position BG_L and position BG_R agree within statistical errors.

After the 10th run, the positions of the limit switches were modified so that they are pushed when the stage reaches position S or position B, and the experimental run described in Chapter 6 was performed.

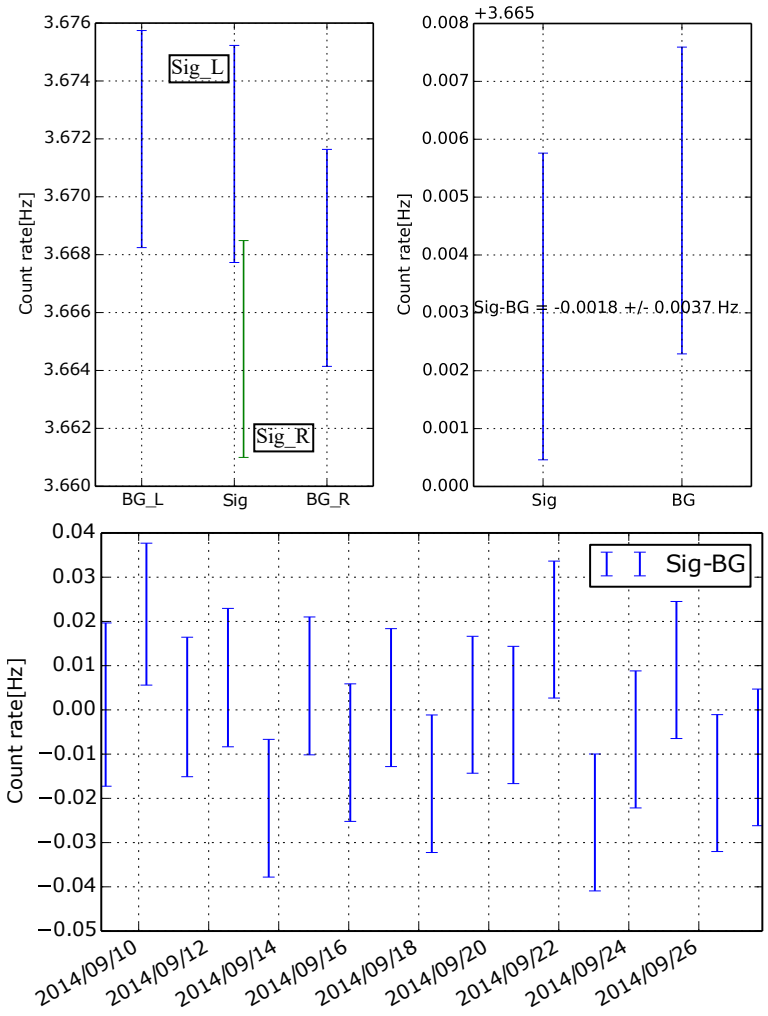

Figure A.12: Result of the 10th run where the effective area of the photomultiplier tube was limited to 1/4 by a sheet of black paper . (Upper left) Accumulated count rates at each position. (Upper right) Data acquired at signal(background)-taking position Sig_L and Sig_R (BG_L and BG_R) are put together to yield a rate labelled 'Sig' ('Background'). (Bottom) Difference in the count rates in time series.

Bibliography

[1] K. G. Begeman, A. H. Broeils, and R. H. Sanders, *Extended rotation curves of spiral galaxies: Dark haloes and modified dynamics*, *Mon. Not. Roy. Astron. Soc.* **249** (1991) 523.

[2] R. Catena and P. Ullio, *A novel determination of the local dark matter density*, *JCAP* **1008** (2010) 004, [arXiv:0907.0018].

[3] D. Clowe, M. Bradac, A. H. Gonzalez, M. Markevitch, S. W. Randall, C. Jones, and D. Zaritsky, *A direct empirical proof of the existence of dark matter*, *Astrophys. J.* **648** (2006) L109–L113, [astro-ph/0608407].

[4] **Planck** Collaboration, R. Adam et al., *Planck 2015 results. I. Overview of products and scientific results*, arXiv:1502.01582.

[5] W. Hu, *CMB temperature and polarization anisotropy fundamentals*, *Annals Phys.* **303** (2003) 203–225, [astro-ph/0210696].

[6] **Planck** Collaboration, P. A. R. Ade et al., *Planck 2015 results. XIII. Cosmological parameters*, arXiv:1502.01589.

[7] F. Wilczek, *Radical conservatism and nucleon decay*, hep-ph/0002045. [AIP Conf. Proc.533,62(2000)].

[8] J. L. Feng, *Dark Matter and Indirect Detection in Cosmic Rays*, *AIP Conf. Proc.* **1516** (2012) 170–176, [arXiv:1211.3116].

[9] **LUX** Collaboration, D. S. Akerib et al., *The Large Underground Xenon (LUX) Experiment*, *Nucl. Instrum. Meth.* **A704** (2013) 111–126, [arXiv:1211.3788].

[10] **LUX** Collaboration. https://www.flickr.com/photos/luxdarkmatter/.

[11] **Majorana** Collaboration, V. E. Guiseppe et al., *The Majorana Neutrinoless Double-Beta Decay Experiment*, *IEEE Nucl. Sci. Symp. Conf. Rec.* **2008** (2008) 1793–1798, [arXiv:0811.2446].

[12] **SuperCDMS** Collaboration, R. Agnese et al., *Search for Low-Mass Weakly Interacting Massive Particles with SuperCDMS*, *Phys. Rev. Lett.* **112** (2014), no. 24 241302, [arXiv:1402.7137].

[13] K. Miuchi et al., *Direction-sensitive dark matter search results in a surface laboratory*, *Phys. Lett.* **B654** (2007) 58–64, [arXiv:0708.2579].

[14] **Particle Data Group** Collaboration, K. A. Olive et al., *Review of Particle Physics*, *Chin. Phys.* **C38** (2014) 090001.

[15] **ADMX** Collaboration, G. Rybka, *Direct Detection Searches for Axion Dark Matter*, *Phys. Dark Univ.* **4** (2014) 14–16.

[16] **ADMX** Collaboration, S. J. Asztalos et al., *SQUID-Based Microwave Cavity Search for Dark-Matter Axions*, *Physical Review Letters* **104** (Jan., 2010) 041301, [arXiv:0910.5914].

[17] J. Jaeckel and A. Ringwald, *The Low-Energy Frontier of Particle Physics*, *Ann. Rev. Nucl. Part. Sci.* **60** (2010) 405–437, [arXiv:1002.0329].

[18] K. Ehret et al., *New ALPS Results on Hidden-Sector Lightweights*, *Phys. Lett.* **B689** (2010) 149–155, [arXiv:1004.1313].

[19] R. Bähre et al., *Any light particle search II -Technical Design Report*, *JINST* **8** (2013) T09001, [arXiv:1302.5647].

[20] J. Redondo, *Atlas of solar hidden photon emission*, *JCAP* **1507** (2015), no. 07 024, [arXiv:1501.07292].

[21] T. Mizumoto, R. Ohta, T. Horie, J. Suzuki, Y. Inoue, and M. Minowa, *Experimental search for solar hidden photons in the eV energy range using kinetic mixing with photons*, *JCAP* **1307** (2013) 013, [arXiv:1302.1000].

[22] T. Mizumoto, *Experimental search for solar hidden sector photons in the ev energy range using kinetic mixing with photon*, *Doctor thesis* (2010).

[23] M. Schwarz, E.-A. Knabbe, A. Lindner, J. Redondo, A. Ringwald, M. Schneide, J. Susol, and G. Wiedemann, *Results from the Solar Hidden Photon Search (SHIPS)*, *JCAP* **1508** (2015), no. 08 011, [arXiv:1502.04490].

[24] A. E. Nelson and J. Scholtz, *Dark Light, Dark Matter and the Misalignment Mechanism*, *Phys. Rev.* **D84** (2011) 103501, [arXiv:1105.2812].

[25] P. Arias, D. Cadamuro, M. Goodsell, J. Jaeckel, J. Redondo, and A. Ringwald, *WISPy Cold Dark Matter*, *JCAP* **1206** (2012) 013, [arXiv:1201.5902].

[26] J. Redondo and M. Postma, *Massive hidden photons as lukewarm dark matter*, *JCAP* **0902** (2009) 005, [arXiv:0811.0326].

[27] T. Horie, J. Suzuki, Y. Inoue, and M. Minowa (in preparation).

[28] T. Horie, *Experimental search for hidden photon dark matter by using dish antenna method*. PhD thesis, Department of Physics, School of Science, The University of Tokyo, 2015.

[29] J. Suzuki, Y. Inoue, T. Horie, and M. Minowa, *Hidden photon CDM search at Tokyo*, in *11th Patras Workshop on Axions, WIMPs and WISPs Zaragoza, Spain, June 22-26, 2015*, 2015. arXiv:1509.00785.

[30] S. Chaudhuri, P. W. Graham, K. Irwin, J. Mardon, S. Rajendran, and Y. Zhao, *Radio for hidden-photon dark matter detection*, *Phys. Rev.* **D92** (2015), no. 7 075012, [arXiv:1411.7382].

[31] http://www.hamamatsu.com/jp/en/R3550A.html.

[32] E. R. Williams, J. E. Faller, and H. A. Hill, *New experimental test of Coulomb's law: A Laboratory upper limit on the photon rest mass*, *Phys. Rev. Lett.* **26** (1971) 721–724.

[33] D. F. Bartlett and S. Loegl, *LIMITS ON AN ELECTROMAGNETIC FIFTH FORCE*, *Phys. Rev. Lett.* **61** (1988) 2285–2287.

[34] M. Fouche et al., *Search for photon oscillations into massive particles*, *Phys. Rev.* **D78** (2008) 032013, [arXiv:0808.2800].

[35] M. Ahlers, H. Gies, J. Jaeckel, J. Redondo, and A. Ringwald, *Laser experiments explore the hidden sector*, *Phys. Rev.* **D77** (2008) 095001, [arXiv:0711.4991].

[36] **GammeV (T-969)** Collaboration, A. S. Chou, W. C. Wester, III, A. Baumbaugh, H. R. Gustafson, Y. Irizarry-Valle, P. O. Mazur, J. H. Steffen, R. Tomlin, X. Yang, and J. Yoo, *Search for axion-like particles using a variable baseline photon regeneration technique*, *Phys. Rev. Lett.* **100** (2008) 080402, [arXiv:0710.3783].

[37] J. Redondo, *Helioscope Bounds on Hidden Sector Photons*, *JCAP* **0807** (2008) 008, [arXiv:0801.1527].

[38] S. N. Gninenko and J. Redondo, *On search for eV hidden sector photons in Super-Kamiokande and CAST experiments*, *Phys. Lett.* **B664** (2008) 180–184, [arXiv:0804.3736].

[39] A. Mirizzi, J. Redondo, and G. Sigl, *Microwave Background Constraints on Mixing of Photons with Hidden Photons*, *JCAP* **0903** (2009) 026, [arXiv:0901.0014].

[40] H. An, M. Pospelov, and J. Pradler, *New stellar constraints on dark photons*, *Phys. Lett.* **B725** (2013) 190–195, [arXiv:1302.3884].

[41] J. Redondo and G. Raffelt, *Solar constraints on hidden photons re-visited*, *JCAP* **1308** (2013) 034, [arXiv:1305.2920].

[42] **FUNK Experiment** Collaboration, D. Veberic et al., *Search for dark matter in the hidden-photon sector with a large spherical mirror*, *PoS* **ICRC2015** (2015) 1191, [arXiv:1509.02386].

[43] B. Döbrich, K. Daumiller, R. Engel, M. Kowalski, A. Lindner, J. Redondo, and M. Roth, *Hidden Photon Dark Matter Search with a Large Metallic Mirror*, in *10th Patras Workshop on Axions, WIMPs and WISPs (AXION-WIMP 2014) Geneva, Switzerland, June 29-July 4, 2014*, 2014. arXiv:1410.0200.

[44] A. V. Kopylov, I. V. Orekhov, and V. V. Petukhov, *Using a Multi-Cathode Counter (MCC) in the Search for Hidden Photon CDM*, arXiv:1509.03033.

[45] J. Edsjo, *Aspects of neutrino detection of neutralino dark matter*. PhD thesis, Uppsala U., 1997. hep-ph/9704384.

[46] G. Bertone, D. Hooper, and J. Silk, *Particle dark matter: Evidence, candidates and constraints*, *Phys. Rept.* **405** (2005) 279–390, [hep-ph/0404175].

[47] L. B. Okun, *LIMITS OF ELECTRODYNAMICS: PARAPHOTONS?*, *Sov. Phys. JETP* **56** (1982) 502. [Zh. Eksp. Teor. Fiz.83,892(1982)].

[48] B. Holdom, *Two U(1)'s and Epsilon Charge Shifts*, *Phys. Lett.* **B166** (1986) 196.

[49] J. Suzuki, T. Horie, Y. Inoue, and M. Minowa, *Experimental Search for Hidden Photon CDM in the eV mass range with a Dish Antenna*, *JCAP* **1509** (2015), no. 09 042, [arXiv:1504.00118].

[50] S. Weinberg, *Cosmology*. 2008.

[51] H. Murayama, *Physics Beyond the Standard Model and Dark Matter*, in *Les Houches Summer School - Session 86: Particle Physics and Cosmology: The Fabric of Spacetime Les Houches, France, July 31-August 25, 2006*, 2007. arXiv:0704.2276.

[52] M. Srednicki, *Quantum field theory*. Cambridge University Press, 2007.

[53] J. Jeans, *The motions of stars in a kapteyn universe*, *Monthly Notices of the Royal Astronomical Society* **82** (1922) 122–132.

[54] M. Pato, O. Agertz, G. Bertone, B. Moore, and R. Teyssier, *Systematic uncertainties in the determination of the local dark matter density*, *Phys. Rev.* **D82** (2010) 023531, [arXiv:1006.1322].

[55] F. Zwicky, *Die Rotverschiebung von extragalaktischen Nebeln*, *Helv. Phys. Acta* **6** (1933) 110–127.

[56] F. Zwicky, *Republication of: The redshift of extragalactic nebulae*, *General Relativity and Gravitation* **41** (2009), no. 1 207–224.

[57] G. W. Pratt and M. Arnaud, *The mass profile of A1413 observed with XMM-Newton: implications for the M-T relation*, *Astron. Astrophys.* **394** (2002) 375–394, [astro-ph/0207315].

[58] M. Bradac, S. W. Allen, T. Treu, H. Ebeling, R. Massey, R. G. Morris, A. von der Linden, and D. Applegate, *Revealing the properties of dark matter in the merging cluster MACSJ0025.4-1222*, *Astrophys. J.* **687** (2008) 959, [arXiv:0806.2320].

[59] A. Mahdavi, H. y. Hoekstra, A. y. Babul, D. y. Balam, and P. Capak, *A Dark Core in Abell 520*, *Astrophys. J.* **668** (2007) 806–814, [arXiv:0706.3048].

[60] H. R. Russell, J. S. Sanders, A. C. Fabian, S. A. Baum, M. Donahue, A. C. Edge, B. R. McNamara, and C. P. O'Dea, *Chandra observation of two shock fronts in the merging galaxy cluster Abell 2146*, *Mon. Not. Roy. Astron. Soc.* **406** (2010) 1721, [arXiv:1004.1559].

[61] S. Giacintucci, T. Venturi, G. Macario, D. Dallacasa, G. Brunetti, M. Markevitch, R. Cassano, S. Bardelli, and R. Athreya, *Shock acceleration as origin of the radio relic in A521?*, *Astron. Astrophys.* **486** (2008) 347, [arXiv:0803.4127].

[62] A. A. Penzias and R. W. Wilson, *A Measurement of excess antenna temperature at 4080-Mc/s*, *Astrophys. J.* **142** (1965) 419–421.

[63] C. L. Bennett, A. Banday, K. M. Gorski, G. Hinshaw, P. Jackson, P. Keegstra, A. Kogut, G. F. Smoot, D. T. Wilkinson, and E. L. Wright, *Four year COBE DMR cosmic microwave background observations: Maps and basic results*, *Astrophys. J.* **464** (1996) L1–L4, [astro-ph/9601067].

[64] **EROS-2** Collaboration, P. Tisserand et al., *Limits on the Macho Content of the Galactic Halo from the EROS-2 Survey of the Magellanic Clouds*, *Astron. Astrophys.* **469** (2007) 387–404, [astro-ph/0607207].

[65] **Troitsk** Collaboration, V. N. Aseev et al., *An upper limit on electron antineutrino mass from Troitsk experiment*, *Phys. Rev.* **D84** (2011) 112003, [arXiv:1108.5034].

[66] S. Profumo, *Astrophysical Probes of Dark Matter*, arXiv:1301.0952.

[67] C. A. Baker et al., *An Improved experimental limit on the electric dipole moment of the neutron*, *Phys. Rev. Lett.* **97** (2006) 131801, [hep-ex/0602020].

[68] R. D. Peccei and H. R. Quinn, *CP Conservation in the Presence of Instantons*, *Phys. Rev. Lett.* **38** (1977) 1440–1443.

[69] S. Weinberg, *A New Light Boson?*, *Phys. Rev. Lett.* **40** (1978) 223–226.

[70] M. S. Turner, *Windows on the Axion*, *Phys. Rept.* **197** (1990) 67–97.

[71] J. E. Kim, *Weak Interaction Singlet and Strong CP Invariance*, *Phys. Rev. Lett.* **43** (1979) 103.

[72] M. A. Shifman, A. I. Vainshtein, and V. I. Zakharov, *Can Confinement Ensure Natural CP Invariance of Strong Interactions?*, *Nucl. Phys.* **B166** (1980) 493.

[73] A. R. Zhitnitsky, *On Possible Suppression of the Axion Hadron Interactions. (In Russian)*, *Sov. J. Nucl. Phys.* **31** (1980) 260. [Yad. Fiz.31,497(1980)].

[74] M. Dine, W. Fischler, and M. Srednicki, *A Simple Solution to the Strong CP Problem with a Harmless Axion*, *Phys. Lett.* **B104** (1981) 199.

[75] J. Conrad, *Indirect Detection of WIMP Dark Matter: a compact review*, in *Interplay between Particle and Astroparticle physics London, United Kingdom, August 18-22, 2014*, 2014. arXiv:1411.1925.

[76] A. Rubbia, *ArDM: A Ton-scale liquid Argon experiment for direct detection of dark matter in the universe*, *J. Phys. Conf. Ser.* **39** (2006) 129–132, [hep-ph/0510320].

[77] **LUX** Collaboration, D. S. Akerib et al., *First results from the LUX dark matter experiment at the Sanford Underground Research Facility*, *Phys. Rev. Lett.* **112** (2014) 091303, [arXiv:1310.8214].

[78] **XENON100** Collaboration, E. Aprile et al., *The XENON100 Dark Matter Experiment*, *Astropart. Phys.* **35** (2012) 573–590, [arXiv:1107.2155].

[79] **XENON100** Collaboration, E. Aprile et al., *Dark Matter Results from 225 Live Days of XENON100 Data*, *Phys. Rev. Lett.* **109** (2012) 181301, [arXiv:1207.5988].

[80] **XENON1T** Collaboration, E. Aprile, *The XENON1T Dark Matter Search Experiment*, *Springer Proc. Phys.* **148** (2013) 93–96, [arXiv:1206.6288].

[81] **XMASS** Collaboration, K. Abe et al., *Direct dark matter search by annual modulation in XMASS-I*, arXiv:1511.04807.

[82] C. E. Aalseth et al., *Search for an Annual Modulation in a P-type Point Contact Germanium Dark Matter Detector*, *Phys. Rev. Lett.* **107** (2011) 141301, [arXiv:1106.0650].

[83] **CoGeNT** Collaboration, C. E. Aalseth et al., *CoGeNT: A Search for Low-Mass Dark Matter using p-type Point Contact Germanium Detectors*, *Phys. Rev.* **D88** (2013) 012002, [arXiv:1208.5737].

[84] **CDMS** Collaboration, R. Agnese et al., *Silicon Detector Dark Matter Results from the Final Exposure of CDMS II*, *Phys. Rev. Lett.* **111** (2013), no. 25 251301, [arXiv:1304.4279].

[85] R. Bernabei et al., *WIMPs search by scintillators: Possible strategy for annual modulation search with large mass highly radiopure NaI(Tl)*, *Nucl. Phys. Proc. Suppl.* **70** (1999) 79–84, [astro-ph/9710290].

[86] R. Bernabei, P. Belli, F. Cappella, R. Cerulli, C. J. Dai, A. D'Angelo, H. L. He, A. Incicchitti, H. H. Kuang, X. H. Ma, F. Montecchia, F. Nozzoli, D. Prosperi, X. D. Sheng, R. G. Wang, and Z. P. Ye, *New results from DAMA/LIBRA*, *European Physical Journal C* **67** (May, 2010) 39–49, [arXiv:1002.1028].

[87] S. C. Kim et al., *New Limits on Interactions between Weakly Interacting Massive Particles and Nucleons Obtained with CsI(Tl) Crystal Detectors*, *Phys. Rev. Lett.* **108** (2012) 181301, [arXiv:1204.2646].

[88] J. Amare et al., *Status of the ANAIS Dark Matter Project at the Canfranc Underground Laboratory*, in *11th Patras Workshop on Axions, WIMPs and WISPs Zaragoza, Spain, June 22-26, 2015*, 2015. arXiv:1508.07213.

[89] **for the DM-Ice** Collaboration, W. C. Pettus, *DM-Ice: Current Status and Future Prospects*, 2015. arXiv:1510.00378.

[90] R. Trotta, F. Feroz, M. P. Hobson, L. Roszkowski, and R. Ruiz de Austri, *The Impact of priors and observables on parameter inferences in the Constrained MSSM*, *JHEP* **12** (2008) 024, [arXiv:0809.3792].

[91] M. Cahill-Rowley, R. Cotta, A. Drlica-Wagner, S. Funk, J. Hewett, A. Ismail, T. Rizzo, and M. Wood, *Complementarity and Searches for Dark Matter in the pMSSM*, in *Community Summer Study 2013: Snowmass on the Mississippi (CSS2013) Minneapolis, MN, USA, July 29-August 6, 2013*, 2013. arXiv:1305.6921.

[92] J. Billard, L. Strigari, and E. Figueroa-Feliciano, *Implication of neutrino backgrounds on the reach of next generation dark matter direct detection experiments*, *Phys. Rev.* **D89** (2014), no. 2 023524, [arXiv:1307.5458].

[93] P. Sikivie, *Experimental Tests of the Invisible Axion*, *Phys. Rev. Lett.* **51** (1983) 1415–1417. [Erratum: Phys. Rev. Lett.52,695(1984)].

[94] Y. Inoue, Y. Akimoto, R. Ohta, T. Mizumoto, A. Yamamoto, and M. Minowa, *Search for solar axions with mass around 1 ev using coherent conversion of axions into photons*, *Physics Letters B* **668** (2008), no. 2 93 – 97.

[95] K. Zioutas et al., *A Decommissioned LHC model magnet as an axion telescope*, *Nucl. Instrum. Meth.* **A425** (1999) 480–489, [astro-ph/9801176].

[96] **ALPS** Collaboration, K. Ehret, *The ALPS Light Shining Through a Wall Experiment - WISP Search in the Laboratory*, in *Proceedings, 45th Rencontres de Moriond on Electroweak Interactions and Unified Theories*, 2010. arXiv:1006.5741.

[97] **ALPS** Collaboration, K. Ehret et al., *Resonant laser power build-up in ALPS: A 'Light-shining-through-walls' experiment*, *Nucl. Instrum. Meth.* **A612** (2009) 83–96, [arXiv:0905.4159].

[98] R. Bähre et al., *Any light particle search II -Technical Design Report*, *JINST* **8** (2013) T09001, [arXiv:1302.5647].

[99] P. Fayet, *U-boson production in e+ e- annihilations, psi and Upsilon decays, and Light Dark Matter*, *Phys. Rev.* **D75** (2007) 115017, [hep-ph/0702176].

[100] M. Goodsell, J. Jaeckel, J. Redondo, and A. Ringwald, *Naturally Light Hidden Photons in LARGE Volume String Compactifications*, *JHEP* **11** (2009) 027, [arXiv:0909.0515].

[101] I. Yu. Kobzarev and L. B. Okun, *On the Photon mass*, *Usp. Fiz. Nauk* **95** (1968) 131–137. [Sov. Phys. Usp.11,338(1968)].

[102] L. Davis, Jr., A. S. Goldhaber, and M. M. Nieto, *Limit on the photon mass deduced from Pioneer-10 observations of Jupiter's m agnetic field*, *Phys. Rev. Lett.* **35** (1975) 1402–1405.

[103] A. S. Goldhaber and M. M. Nieto, *Terrestrial and extra-terrestrial limits on the photon mass*, *Rev. Mod. Phys.* **43** (1971) 277–296.

[104] H. Cavendish, *The electrical researches of the Honourable Henry Cavendish*. Cmbridge U. Press, 1879. edited by J. Clerk Maxwell.

[105] V. Popov, *On the experimental search for photon mixing*, *Turkish Journal of Physics* **23** (1999), no. 5 943–950.

[106] J. Jaeckel, J. Redondo, and A. Ringwald, *Signatures of a hidden cosmic microwave background*, *Phys. Rev. Lett.* **101** (2008) 131801, [arXiv:0804.4157].

[107] **CAST** Collaboration, S. Andriamonje et al., *An Improved limit on the axion-photon coupling from the CAST experiment*, *JCAP* **0704** (2007) 010, [hep-ex/0702006].

[108] **XENON10** Collaboration, J. Angle et al., *A search for light dark matter in XENON10 data*, *Phys. Rev. Lett.* **107** (2011) 051301, [arXiv:1104.3088]. [Erratum: Phys. Rev. Lett.110,249901(2013)].

[109] **XENON100** Collaboration, E. Aprile et al., *First Axion Results from the XENON100 Experiment*, *Phys. Rev.* **D90** (2014), no. 6 062009, [arXiv:1404.1455].

[110] H. An, M. Pospelov, and J. Pradler, *Observing dark photon with dark matter detectors*, in *10th International Symposium on Cosmology and Particle Astrophysics (CosPA 2013) Honolulu, Hawaii, USA, November 12-15, 2013*, 2014. arXiv:1401.8287.

[111] H. An, M. Pospelov, J. Pradler, and A. Ritz, *Direct Detection Constraints on Dark Photon Dark Matter*, *Phys. Lett.* **B747** (2015) 331–338, [arXiv:1412.8378].

[112] K. Van Bibber, N. R. Dagdeviren, S. E. Koonin, A. Kerman, and H. N. Nelson, *Proposed experiment to produce and detect light pseudoscalars*, *Phys. Rev. Lett.* **59** (1987) 759–762.

[113] C. Robilliard, R. Battesti, M. Fouche, J. Mauchain, A.-M. Sautivet, F. Amiranoff, and C. Rizzo, *No light shining through a wall*, *Phys. Rev. Lett.* **99** (2007) 190403, [arXiv:0707.1296].

[114] M. Frede, B. Schulz, R. Wilhelm, P. Kwee, F. Seifert, B. Willke, and D. Kracht, *Fundamental mode, single-frequency laser amplifier for gravitational wave detectors*, *Opt. Express* **15** (Jan, 2007) 459–465.

[115] Y. Takasu Master's thesis, Department of Physics, School of Science, The University of Tokyo, 1999.

[116] T. Namba Master's thesis, Department of Physics, School of Science, The University of Tokyo, 1997.

[117] http://aa.usno.navy.mil/software/novas/novas_info.php.

[118] H. An, M. Pospelov, and J. Pradler, *Dark Matter Detectors as Dark Photon Helioscopes*, *Phys. Rev. Lett.* **111** (2013) 041302, [arXiv:1304.3461].

[119] A. Golovnev, V. Mukhanov, and V. Vanchurin, *Vector Inflation*, *JCAP* **0806** (2008) 009, [arXiv:0802.2068].

[120] D. Cadamuro, S. Hannestad, G. Raffelt, and J. Redondo, *Cosmological bounds on sub-MeV mass axions*, *JCAP* **1102** (2011) 003, [arXiv:1011.3694].

[121] D. J. Fixsen, E. S. Cheng, J. M. Gales, J. C. Mather, R. A. Shafer, and E. L. Wright, *The Cosmic Microwave Background spectrum from the full COBE FIRAS data set*, *Astrophys. J.* **473** (1996) 576, [astro-ph/9605054].

[122] L. Danese and G. de Zotti, *Double Compton process and the spectrum of the microwave background*, *Astron. Astrophys.* **107** (Mar., 1982) 39–42.

[123] D. Horns, J. Jaeckel, A. Lindner, A. Lobanov, J. Redondo, and A. Ringwald, *Searching for WISPy Cold Dark Matter with a Dish Antenna*, *JCAP* **1304** (2013) 016, [arXiv:1212.2970].

[124] J. Jaeckel and J. Redondo, *An antenna for directional detection of WISPy dark matter*, *JCAP* **1311** (2013) 016, [arXiv:1307.7181].

[125] J. Jaeckel and S. Knirck, *Directional Resolution of Dish Antenna Experiments to Search for WISPy Dark Matter*, arXiv:1509.00371.

[126] P. Arias, A. Arza, B. Döbrich, J. Gamboa, and F. Méndez, *Extracting Hidden-Photon Dark Matter From an LC-Circuit*, *Eur. Phys. J.* **C75** (2015), no. 7 310, [arXiv:1411.4986].

[127] L. D. Duffy and P. Sikivie, *The Caustic Ring Model of the Milky Way Halo*, *Phys. Rev.* **D78** (2008) 063508, [arXiv:0805.4556].

[128] J. I. Read, G. Lake, O. Agertz, and V. P. Debattista, *Thin, thick and dark discs in LCDM*, *Mon. Not. Roy. Astron. Soc.* **389** (2008) 1041–1057, [arXiv:0803.2714].

[129] **Pierre Auger** Collaboration, J. Abraham et al., *Properties and performance of the prototype instrument for the Pierre Auger Observatory*, *Nucl. Instrum. Meth.* **A523** (2004) 50–95.